

SYNTHESIS OF HIGH TEMPERATURE STABLE TITANIA NANOPARTICLES FOR PHOTOCATALYTIC APPLICATIONS

A dissertation submitted for the degree of

Doctor of Engineering

Presented by

Dipl.-Ing. Fei Qi

Faculty of Mathematics/Computer Science and Mechanical Engineering

Clausthal University of Technology

Clausthal-Zellerfeld, 2013

Acknowledgements

I would like to express the deepest appreciation to Prof. Dr. Alfred Weber, for his continuous support, inspiration and scientific advices and to Prof. Dr. Joachim Deubener for discussions on characterization of TiO_2 photocatalysts and co-advising this Ph.D thesis. Special thanks to my coworker Dr.-Ing. Anna Moiseev for her assiduous work and helpful suggestions as well as valuable advices for the publications. Without their help and support, the work could not have been produced so many interesting results.

This work was a cooperation between the Institute of Particle Technology and the Institute of Non-Metallic Materials at TU Clausthal and it could not have been accomplished without the contributions of all my friends and colleagues.

In the Institute of Particle Technology, I would like to thank Dr.-Ing. Kurt Legenhausen for his extensive support. Special thanks go to Dipl.-Ing. Stephan Rennecke for many fruitful discussions and correction of all my publications. Many thanks to Katrin Ernst, Musaddik Dudic, Mannuel Gensch, Jun Hou, Dagma Koch and Lintao Zeng for the good teamwork and support. In addition, best thanks to Peggy Knospe and Martina Ketterer for characterization and visualization of innumerable nanoparticles as well as Henning Dunemann and Roland Schmidt for the fabrication of experimental set-ups in the workshop.

In the Institute of Non-Metallic Materials, I would like to thank Michael Zellmann for the XRD analysis and Thomas Peter as well as Reinhard Görke for the characterization of coatings.

Special thanks go to Maike Hermeling. Without her patient help and encouragement I could not have finished my Ph.D. study.

This work would not have been completed without the valuable contributions of all the diploma students, Martin Werkmeister, Hang Ruan, Jinglei Liu, as well as Hongwei Hao, who have worked as assistant with me.

Finally, I would like to express my deepest gratitude to my parents and family for all unconditional supports and patience.

Table of Contents

Abstract	1
1 Introduction	3
2 Theory	7
2.1 Heterogeneous photocatalysis.....	7
2.2 Photocatalysis on TiO ₂	9
2.3 TiO ₂ nanoparticles	12
2.3.1 Structural properties of TiO ₂	13
2.3.2 Synthesis of TiO ₂	14
2.3.3 Thermodynamic stability of TiO ₂	18
2.3.4 Synthesis of SiO ₂ coated TiO ₂	20
2.3.5 Photocatalytic activity of TiO ₂	22
3 Experimental section	25
3.1 Chemicals	25
3.2 Synthesis of TiO ₂ nanoparticles	25
3.3 Synthesis of TiO ₂ /SiO ₂ nanoparticles.....	28
3.4 Calcination of TiO ₂ /SiO ₂ samples.....	29
3.5 Particle Characterization	30
3.5.1 BET	30
3.5.2 X-Ray Diffraction.....	30
3.5.3 Transmission Electron Microscope	32
3.5.4 Scanning Electron Microscope.....	33
3.6 Photocatalytic activity tests	33
4 Results of pure TiO ₂ and binary TiO ₂ /SiO ₂ nanoparticles.....	35
4.1 Pure TiO ₂ nanoparticles	35

4.1.1	Effect of precursor feed rate on specific surface area	35
4.1.2	Effect of precursor feed rate on phase composition	36
4.1.3	Effect of precursor feed rate on particle morphology and size	38
4.1.4	Effect of precursor feed rate on photocatalytic performance	41
4.1.5	Discussion	45
4.2	Binary TiO ₂ /SiO ₂ nanoparticles	58
4.2.1	Effect of additive and calcination on specific surface area	59
4.2.2	Effect of additive and calcination on phase composition	60
4.2.3	Effect of additive and calcination on particle morphology and size	65
4.2.4	Effect of additive and calcination on photocatalytic performance	67
4.2.5	Effect of impurity ions on thermostability	70
4.2.6	Discussion	74
5	Performance of self-cleaning coatings made of TiO ₂ /SiO ₂ nanoparticles	79
5.1	Self-cleaning coating of extended surface with TiO ₂ photocatalyst	79
5.2	Baking of coatings	79
5.3	Photocatalytic test of coating	80
5.4	Results	81
5.4.1	Structure of coating	81
5.4.2	Phase composition of baked coatings	82
5.4.3	Photocatalytic activity of coating	84
6	Summary	91
7	Outlook	94
8	References	95
9	Publications and Presentations	106
10	Curriculum Vitae	108

Table of Figures

Fig. 1.1: The morphology of TiO ₂ particles before and after heat treatment	4
Fig. 2.1: Schematic illustration of the general mechanistic steps in heterogeneous photocatalysis.....	7
Fig. 2.2: Antenna function of rutile for the charge separation	8
Fig. 2.3: Mechanism of photocatalytic degradation of dichloroacetic acid	11
Fig. 2.4: Mechanism of photocatalytic degradation of 4-chlorophenol.....	11
Fig. 2.5: Crystal structure of anatase, rutile and brookite	13
Fig. 2.6: The basic steps for particle formation and growth by vapor-fed flame synthesis.....	15
Fig. 2.7: Schematic diagram showing the steps of anatase-to-rutile phase transformation.....	19
Fig. 2.8: Comparison of the methods for synthesis of SiO ₂ coated TiO ₂ particles via wet chemical route and gas phase route.....	21
Fig. 2.9: Coating mechanism in a hot wall reactor	23
Fig. 2.10: Electronic structure of semiconductor as a function of monomeric units ..	23
Fig. 3.1: Schematic diagram of the experimental setup for the synthesis of TiO ₂ nanoparticles	26
Fig. 3.2: Schematic diagram of the experimental setup for synthesis of TiO ₂ /SiO ₂ nanoparticles	28
Fig. 3.3: XRD patterns of anatase and rutile.....	31
Fig. 3.4: Diagram of platinum grid and a TEM sample holder with heating function for online observation	32
Fig. 4.1: The specific surface area and BET-equivalent diameter of flame synthesized TiO ₂ particles as a function of TiCl ₄ precursor feed rate	35
Fig. 4.2: X-ray diffraction patterns of the reference material TiO ₂ P25 and the flame made samples S1, S4 and S8.....	37
Fig. 4.3: The effect of the precursor feed rate on the anatase mass fraction and XRD-equivalent particle size.....	38
Fig. 4.4: Particle morphology and primary particle size distribution of TiO ₂ P25 and flame made samples.....	39
Fig. 4.5: The effect of the precursor feed rate on the TEM-equivalent particle size... ..	40

Fig. 4.6: Photocatalytic degradation of DCA with flame made samples of S1, S4, S6 and S8.....	42
Fig. 4.7: DCA oxidation rate at 30 minute as a function of the precursor feed rate....	43
Fig. 4.8: Photocatalytic degradation of 4-CP with flame made samples of S1, S4, S6 and S8.....	44
Fig. 4.9: 4-CP oxidation rate at 30 minute as a function of the precursor feed rate ...	44
Fig. 4.10: Crystal structure of TiO_2 particles	47
Fig. 4.11: TEM image of non-aggregated TiO_2 nanoparticles.....	47
Fig. 4.12: The mass fraction of rutile as a function of the TEM-equivalent diameter of TiO_2 particles	48
Fig. 4.13: Photocatalytic degradation of DCA with TiO_2 photocatalyst	50
Fig. 4.14: Reaction rate constants k_{DCA} and $k_{4\text{-CP}}$ as a function of anatase mass fraction of TiO_2 particles	51
Fig. 4.15: Reaction rate constants k_{DCA} and $k_{4\text{-CP}}$ as a function of average TEM-equivalent diameter of TiO_2 particles.....	52
Fig. 4.16: Reaction rate constant k_{DCA} and $k_{4\text{-CP}}$ as a function of relative frequency of particles between 10 nm and 15 nm	53
Fig. 4.17: Comparison of particle size distribution and area under 10nm to 15 nm of sample S8 and TiO_2 P25	54
Fig. 4.18: Normalized reaction rate constants k'_{DCA} and $k'_{4\text{-CP}}$ as a function of average TEM-equivalent diameter of TiO_2 particles	55
Fig. 4.19: The influence of particle size on the band gap energy of TiO_2 particles ...	56
Fig. 4.20: X-ray diffraction patterns of the non-stabilized sample S6 and the stabilized non-calcinated samples P1 and P5 before calcination	61
Fig. 4.21: X-ray diffraction patterns of the non-stabilized sample S6 calcinated at 900 °C and the stabilized sample P2 calcinated at 900 °C and 1000 °C...	62
Fig. 4.22: X-ray diffraction patterns of the sample P5 non-calcinated and calcinated at 900 °C, 1000 °C, 1050 °C, 1100 °C and 1150 °C.....	63
Fig. 4.23: The effect of Si/Ti ratio on the anatase content in the $\text{TiO}_2/\text{SiO}_2$ particles after calcination between 900 °C and 1200 °C	64
Fig. 4.24: Morphology of $\text{TiO}_2/\text{SiO}_2$ nanoparticles	65
Fig. 4.25: The effect of calcination on the particle morphology and the average TiO_2 core size	67
Fig. 4.26: Change of the SiO_2 layer after calcination at 1100°C and 1150 °C	67

Fig. 4.27: Photocatalytic degradations of DCA with calcinated sample P5	68
Fig. 4.28: Photocatalytic oxidation rate of DCA with calcinated samples as a function of Si/Ti ratio	69
Fig. 4.29: Influence of calcium ions on the phase composition of $\text{TiO}_2/\text{SiO}_2$ particles calcinated at 950 °C for 3 hours	71
Fig. 4.30: Influence of iron ion on the phase composition of $\text{TiO}_2/\text{SiO}_2$ particles calcinated at 950 °C for 3 hours	73
Fig. 4.31: Size distribution of SiO_2 layer thickness of sample P1, P3 and P5	75
Fig. 4.32: Photocatalytic degradation of DCA with non-calcinated samples P3, P4, P5 and P6.....	76
Fig. 4.33: Observation of the change of SiO_2 layer with online heating	78
Fig. 4.34: Observation of the change of $\text{TiO}_2/\text{SiO}_2$ structure with online heating	78
Fig. 5.1: Apparatus for photocatalytic test of coatings	80
Fig. 5.2: SEM-image of the morphology of $\text{TiO}_2/\text{SiO}_2$ coating before baking	81
Fig. 5.3: Roughness of the coating surface as a function of baking temperature	82
Fig. 5.4: XRD patterns of TiO_2 P25 scratched from coatings after baking at 150 °C, 550 °C and 650 °C and XRD patterns of $\text{TiO}_2/\text{SiO}_2$ scratched from coatings after baking at 150 °C, 550 °C and 950 °C.....	83
Fig. 5.5: The effect of the baking temperature on the phase composition of the TiO_2 P25 and $\text{TiO}_2/\text{SiO}_2$ particles	84
Fig. 5.6: The DCA degradation curves of TiO_2 P25 coating on Si-wafer baked at different temperatures.....	85
Fig. 5.7: The DCA degradation curves of $\text{TiO}_2/\text{SiO}_2$ coating on Si-wafer baked at different temperatures.....	86
Fig. 5.8: Reaction rate constant of TiO_2 P25 coating and $\text{TiO}_2/\text{SiO}_2$ coating as a function of baking temperature	87
Fig. 5.9: Water contact angle measurement on TiO_2 P25 film without UV irradiation and with UV irradiation.....	89
Fig. 5.10: The effect of heat treatment and UV irradiation on the contact angle on the $\text{TiO}_2/\text{SiO}_2$ film.....	90

Table of Tables

Tab. 3.1: Synthesis conditions of TiO_2 nanoparticles.....	27
Tab. 3.2: Synthesis condition of $\text{TiO}_2/\text{SiO}_2$ nanoparticles	29
Tab. 4.1: Comparison of the equivalent diameter of pure TiO_2 Particles determined from BET, XRD and TEM measurements.....	46
Tab. 4.2: Physical properties of non-stabilized sample S7	58
Tab. 4.3: Summary of the specific surface area of non-calcinated and calcinated $\text{TiO}_2/\text{SiO}_2$ particles.....	59

Abstract

Titanium dioxide is one of the prominent semiconductors in various kinds of industrial applications, such as photovoltaic and photocatalysis. TiO_2 has two main modifications of anatase and rutile. Rutile is generally recognized to be the most stable phase of TiO_2 , while anatase shows higher photocatalytic activity compared to rutile. The photocatalytic activity of TiO_2 is dependent on intrinsic and extrinsic parameters, such as the particle size and crystal habit. Due to high surface area particularly nanoparticles exhibit higher photocatalytic activity than coarse particles.

However, anatase nanoparticles are inherently unstable upon heating and transit irreversibly to rutile at temperatures above 400 °C hindering their applications in high temperature ceramic processes such as co-firing self-cleaning coatings. According to the industrial manufacture of ceramic roof tiles with self-cleaning coating in one step, the TiO_2 particles should exhibit high thermostability at 950 °C for 3 hours.

In this Ph.D. thesis TiO_2 nanoparticles were synthesized by feeding TiCl_4 as precursor into a $\text{CH}_4/\text{O}_2/\text{N}_2$ -premixed flame. In the flame synthesis the photocatalytic properties of TiO_2 particles were optimized by adjusting carrier gas flow rate as well as precursor feed rate. Then, starting from the optimal process parameters, the TiO_2 particles were additionally stabilized by introduction of a second precursor, SiCl_4 , in the flame with varying feed rate. After oxidation SiO_2 condensed on the surface of the already existing TiO_2 particles to build a core-shell structure. The physical properties of the samples were characterized with TEM, XRD and BET, respectively. During calcination, the evolution of the SiO_2 layer was observed online with TEM. To investigate the thermostability, the samples were calcinated at different temperatures between 900°C and 1200 °C for 3 hours and the photocatalytic activity of the samples was determined by the degradation of dichloroacetic acid (DCA) and 4-chlorophenol (4-CP). Furthermore, the thermostability of coatings made of stabilized TiO_2 particles was investigated and related to phase composition and photocatalytic activity.

It was found that the physical and photocatalytic properties of the flame synthesized TiO_2 nanoparticles are strongly dependent on the precursor feed rate as key process

parameter. The specific surface area of TiO_2 particles varied from $160 \text{ m}^2/\text{g}$ to $70 \text{ m}^2/\text{g}$ as the precursor feed rate changed from 0.021 mmol/min to 0.504 mmol/min and simultaneously the BET equivalent particle size increased from 9 nm to 21 nm . All flame synthesized TiO_2 samples mainly consisted of anatase (between $90 \text{ wt.}\%$ and $100 \text{ wt.}\%$), while the rutile mass fraction increased with the fraction of primary particles exceeding the critical size of about 14 nm . The most active TiO_2 sample showed much higher photocatalytic activity compared to the reference material TiO_2 P25 for the DCA degradation.

By enveloping the anatase TiO_2 nanoparticles in SiO_2 it was observed that not only the particle size but also the crystal structure were stabilized up to temperatures of 1050°C . Furthermore, the stabilized TiO_2 particles exhibited surprisingly high photocatalytic activity. However, to enable the photocatalytic activity of the core-shell nanoparticles the SiO_2 coating had to be calcinated at high temperatures to establish the permeability for reactive species. Also coatings on Si-Wafer made of stabilized TiO_2 particles showed high thermostability up to 1050°C indicating that neither the coating process nor the substrate had any influence on the thermostability. These self-cleaning coatings showed also higher photocatalytic activity for DCA decomposition after baking, in contrast to the coatings with the reference material TiO_2 P25.

The stabilization of nanoparticles by SiO_2 coating against coalescence and phase transformation was shown in this work on the example of TiO_2 nanoparticles. However, this concept of high temperature stabilization may be refined for pure contact passivation and extended to other material systems such as metal nanoparticle catalysts.

1 Introduction

Titanium dioxide has attracted much attention due to its special properties and is one of the prominent semiconductors in various kinds of industrial applications, such as photovoltaic [1] and photocatalysis [2-4]. In industry more than two million tons of TiO_2 are produced annually [5]. Because of its high refractive index and chemical stability TiO_2 is usually used in the pigment, plastics and paper industries. In addition, TiO_2 particles, especially at the nano-scale, have various applications in treatment of waste gas and waste water as well as in solar cells and self-cleaning coatings [3, 6], due to their catalytic properties.

For several decades TiO_2 particles were produced in flame reactors instead of the liquid phase by means of the chloride-process [7, 8]. TiO_2 powders made in flame reactors exhibit higher purities compared to the products from liquid phase and no further treatments such as filtration, drying and calcination are required. Furthermore, the properties of TiO_2 particles are well controlled in the flame process by adjusting the process parameters of the experiment [9, 10]. Therefore, the flame synthesis is preferably suitable for the preparation of TiO_2 particles, in particular at the nano-scale.

TiO_2 has two main modifications, anatase and rutile. Rutile is generally recognized to be the most stable phase of TiO_2 . Anatase shows a higher photocatalytic activity compared to rutile [11, 12]. The photocatalytic activity of TiO_2 is dependent on the intrinsic parameters such as particle size, phase composition and extrinsic parameters of the experiments such as the concentration of TiO_2 or pH value of the solution [13-16]. Smaller particles, particularly nanoparticles exhibit higher photocatalytic activity than coarse particles, because small particles offer larger specific surface area for the photocatalytically chemical reactions. However, if the particles are too small, the photocatalytic activity is poor because of the so-called "quantum size effect" [4, 17, 18].

Nevertheless, due to their high surface energy, anatase nanoparticles are inherently unstable upon heating as reflected by a reduced melting point and enhanced coalescence [19, 20]. Furthermore, anatase transits irreversibly to rutile at temperatures above 400 °C [16]. This hinders the applications of TiO_2 particles in ceramic processes for such as co-firing self-cleaning coatings, which are processed

at high temperatures. According to the industrial manufacture of roof tiles with self-cleaning coating in one step, which was the starting point for the research presented here, the TiO_2 particles must exhibit high thermostability at 950 °C for 3 hours. Fig. 1.1 shows the morphology of the commercial product TiO_2 P25 of Evonik before (left) and after calcination at 950°C for 3 hours (right). The non-calcinated TiO_2 P25 particles are very small, about 20 nm (left). This powder is also very active, because it consists of about 80 wt.% anatase. After heat treatment the TiO_2 particles sintered and coalesced very strongly (right). Due to the phase transformation and the grain growth the TiO_2 particles lost their photocatalytic activity after heat treatment almost completely. The influence of heat treatment of TiO_2 P25 on the particle properties and the photocatalytic activity was reported in detail by Nádia [21]. They found that the onset temperature of phase transformation of TiO_2 P25 was about 500 °C and after calcination at 600 °C all anatase transited to rutile.

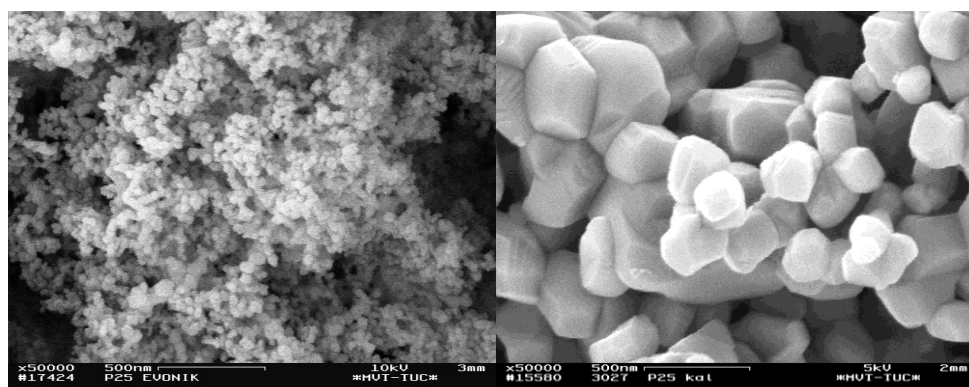


Fig. 1.1: The morphology of TiO_2 particles before (left) and after heat treatment at 950°C for 3 hours (right)

Zhang et al. [19, 20, 22] have reported that a critical particle size is the dominant parameter for the phase transformation, because the surface free energy of anatase is lower than that of rutile. According to their studies, anatase is more stable than rutile when the particle diameter is smaller than 14 nm. The result is in agreement with the studies of Hu et al. [23] and Kobata et al. [24] reporting that critical particle size for the phase transformation is around 15 nm. In addition, Kobata et al. have simulated the phase transformation from anatase to rutile in a tubular reactor. If the activation energy for the phase transformation is above 400 kJ/mol, the rutile mass fraction increases with increasing temperature. They have also examined the

sintering process by checking the primary particle size with increased calcination temperature. Increasing calcination temperature leads to the loss of desirable properties of anatase and limits the applications of anatase with respect to the photocatalytic activity at high temperature processes.

Therefore, to extend the application of anatase to high temperatures by preventing phase transformation and grain growth, it is necessary to stabilize the anatase particles. The thermostability of TiO_2 can be improved by using metallic and non-metallic additives [17, 25] as well as dopants [26] in liquid phase or in gas phase. Shannon et al. [27] have reported that the phase transformation of single anatase particles occurs at about 900 °C. Therefore, Tobaldi et al. [25] mixed the commercial product TiO_2 P25 with silica powder at various concentrations in water. It was desired that the TiO_2 particles are separated by the SiO_2 particles to enhance their thermostability. They found out that the mixed TiO_2 and SiO_2 formed new Ti-O-Si bonds after calcination exhibiting higher thermostability up to 900 °C. Okada et al. [28] investigated the effect of silica additive on the anatase to rutile phase transformation as well as the thermostability. The experiments showed that the anatase particles were stable up to 1000 °C after the addition of 5 mol% of SiO_2 for 1 hour, because the added SiO_2 was expelled from the interior to the TiO_2 surface forming an amorphous SiO_2 layer. Teleki [29] has introduced an online coating method of TiO_2 particles with SiO_2 by flame synthesis. He concluded that the TiO_2 particles showed no photocatalytic activity, when the TiO_2 particles are coated with more than 10 wt.% SiO_2 . It indicates that in this case the TiO_2 particles are completely encapsulated with a SiO_2 shell. According to the theory of Shannon et al. [27], the core-shell $\text{TiO}_2/\text{SiO}_2$ particles must show high thermostability.

In the present work, TiO_2 particles are synthesized by oxidation of a TiCl_4 precursor in an O_2/CH_4 premixed flame. Flame synthesis is favored for the production of nanosized TiO_2 exhibiting high photocatalytic activity, because in the flame amorphous anatase is firstly formed while crystal anatase and rutile are formed later [30, 31]. To prevent the phase transformation from anatase to rutile, SiCl_4 as second precursor is introduced directly into the flame. It was expected that SiO_2 formed amorphous protection layers on the TiO_2 particles for a core-shell structure according to the studies of Hung et al. [32]. They have found that at low flame temperatures up to about 1200 °C and/or with high Si to Ti ratios the TiO_2 particles are encapsulated

with SiO_2 in a counterflow diffusion flame reactor. Akurati et al. [33], Ehrman et al. [34] and Kim et al. [35] have studied and simulated the possible formation of SiO_2 on different kinds of particles. Teleki et al. [36] have also synthesized silica coated titania in one step in a flame reactor and checked the quality of SiO_2 -coating by examining the isoelectric point of the particles. By these processes silica layer is amorphous and prevents the direct contact and grain growth of anatase particles and inhibits the phase transformation. These results are consistent with the study of Hofer et al. [37]. The present study focuses on the optimization of the process parameters to synthesize TiO_2 particles with high photocatalytic activity. Based on the optimized parameters the TiO_2 particles are stabilized with SiO_2 additive using various concentrations. The physical properties of samples such as the primary particle size, particle morphology, phase composition, specific surface area are characterized with TEM, XRD and BET. The development of SiO_2 layer was observed online with TEM during calcination. To investigate the thermostability, the stabilized samples were calcinated at different temperatures between 900°C and 1200°C for 3 hours and the photocatalytic activity of the samples was determined by the degradation of the model compounds of dichloroacetic acid (DCA) and 4-chlorophenol (4-CP), respectively.

In the following, the experiments to synthesize and characterize pure and silica coated titania nanoparticles as well as the setup to determine their photocatalytic activity are outlined. Then, the results for pure TiO_2 nanoparticles are presented and discussed. Finally, as the main objective of this work, the results for silica coated titania nanoparticles with respect to thermostability and photocatalytic activity will be shown and discussed. In addition to the examination of the photocatalytic activity in suspensions, the results of first photocatalytic activity tests of extended surfaces with a self-cleaning coating of the synthesized $\text{TiO}_2/\text{SiO}_2$ nanoparticles will also be presented.

2 Theory

2.1 Heterogeneous photocatalysis

Photocatalysis is based on semiconductors, which use light energy in the form of photons to activate chemical reactions. The basic mechanism of photocatalysis is shown in Fig. 2.1 and described in equation 2.1 to 2.3. When a semiconductor particle absorbs a photon with energy equal to or higher than the band gap energy of the semiconductor, an electron can be promoted from the valence band to the conduction band (equation 2.1). This results in the generation of electron e^- / hole h^+ pairs, which can migrate to the semiconductor particle surface and oxidize or reduce (pathway c, d and equation 2.1, 2.2) the surface adsorbed species before recombination can take place (pathway a and b). The recombination of the separated electron and hole can occur at the semiconductor surface (pathway a) or in the semiconductor volume (pathway b), which should be retarded for an efficient charge transfer. The electron transfer is more efficient if the species are preadsorbed on the semiconductor surface [38].

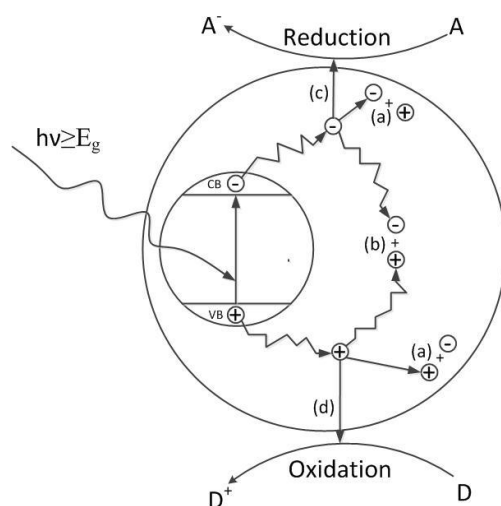


Fig. 2.1: Schematic illustration of the general mechanistic steps in heterogeneous photocatalysis (a) Recombination of electron and defect electron pairs at the semiconductor surface; (b) Recombination of electron and defect electron pairs in the volume of the semiconductor; (c) Reduction of an electron acceptor A at the semiconductor surface; (d) Oxidation of an electron donor D at the semiconductor surface [39]



As illustrated in Fig. 2.1, the precondition is that the photon energy must be equal to or higher than the band gap energy of the semiconductor, so that the activation of the semiconductor photocatalyst for the reaction (equation 2.1) can be achieved. In addition, the band gap energy of the semiconductor and the thermodynamic positions of the valence and conduction band have a great influence on the transfer of electron pairs from the semiconductor to the adsorbed species. For an efficient transfer of the electron pairs, the relevant potential level of the electron acceptor must be thermodynamically stable under the conduction band level of the semiconductor and the potential level of the electron donor must be above the valence band level [40]. There is evidence that TiO_2 powders consisting of both, anatase and rutile phase, respectively, show higher photocatalytic activity compared to TiO_2 powder consisting of one phase alone, because rutile helps to separate the generated electron and hole pairs in the anatase crystal (Fig. 2.2).

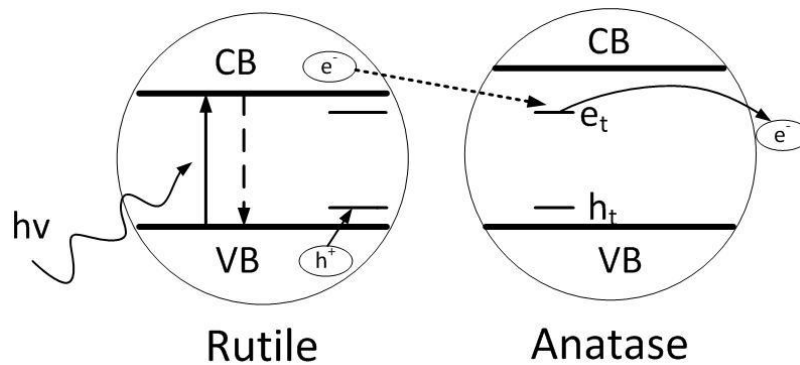


Fig. 2.2: Antenna function of rutile for the charge separation [41]

2.2 Photocatalysis on TiO₂

TiO₂ is an n-type semiconductor with a large band gap energy of 3.0 eV for rutile and 3.2 eV for anatase. Absorption of photons with energy higher than 3.2 eV by TiO₂ particles leads to a promotion of an electron from the valence band to the conduction band and simultaneously results in a positive charged hole in the valence band, which is described in equation 2.4 [4].



Where e_{CB}^- is the electron promoted to the conduction band and h_{VB}^+ is the hole in the valence band.

The generation of charge carriers is very fast and at the order of femtoseconds [4, 39]. However, most of the excited charge carriers recombine within a short time at the surface or in the volume of the TiO₂ particle resulting in the releasing of heat (equation 2.5) [42].



The remaining charge carriers, react with water or hydroxide ions adsorbed on the TiO₂ surface to form surface-bound hydroxyl radicals in case of holes h_{VB}^+ (equation 2.6 and 2.7) [42]:



The promoted electrons e_{CB}^- in the conduction band reduce oxygen adsorbed on the surface (equation 2.8) to form peroxy radicals (equation 2.9), peroxy ions (equation 2.10) and hydrogen peroxide (equation 2.11 and 2.12) and the hydrogen peroxide forms further hydroxyl radicals (equation 2.13 to 2.15) [43]:





The formed OH-radicals are the primary oxidizing species in the photocatalytic processes. The OH-radicals and the photogenerated holes are strong oxidizing agents, which are able to decompose inorganic and organic substrates (R) in a chain of reactions (equation 2.16 and 2.17). The intermediate formed organic radicals R^{\cdot} add quickly to the dissolved oxygen and form reactive peroxide radicals, which react further to hydroperoxide radicals, hydrogen peroxide and other peroxides, aldehydes and carboxylic acids [4, 42].



The degradation of organic compounds on TiO_2 photocatalyst is very complex. Fig. 2.3 and Fig. 2.4 show the possible routes for the photocatalytic degradation of dichloroacetic acid and 4-chlorophenol. As shown in these figures, the routes of organic destruction on the TiO_2 photocatalyst and formation of intermediates during the photocatalytic degradation depend strongly on the type of the organic compound, light intensity, additive of oxidant and reaction conditions. The common of the reactions is that the final products of the photocatalytic reaction by adding oxygen or other oxidants of organic compounds are CO_2 , H_2O and mineral acids. However, the degradation of 4-chlorophenol is more tedious and consequently takes longer time than that of dichloroacetic acid, because the molecules of 4-chlorophenol is much larger and more complex than dichloroacetic acid molecules. Therefore, at least one step described above in Fig. 2.4 is the limiting step for the degradation of 4-chlorophenol.

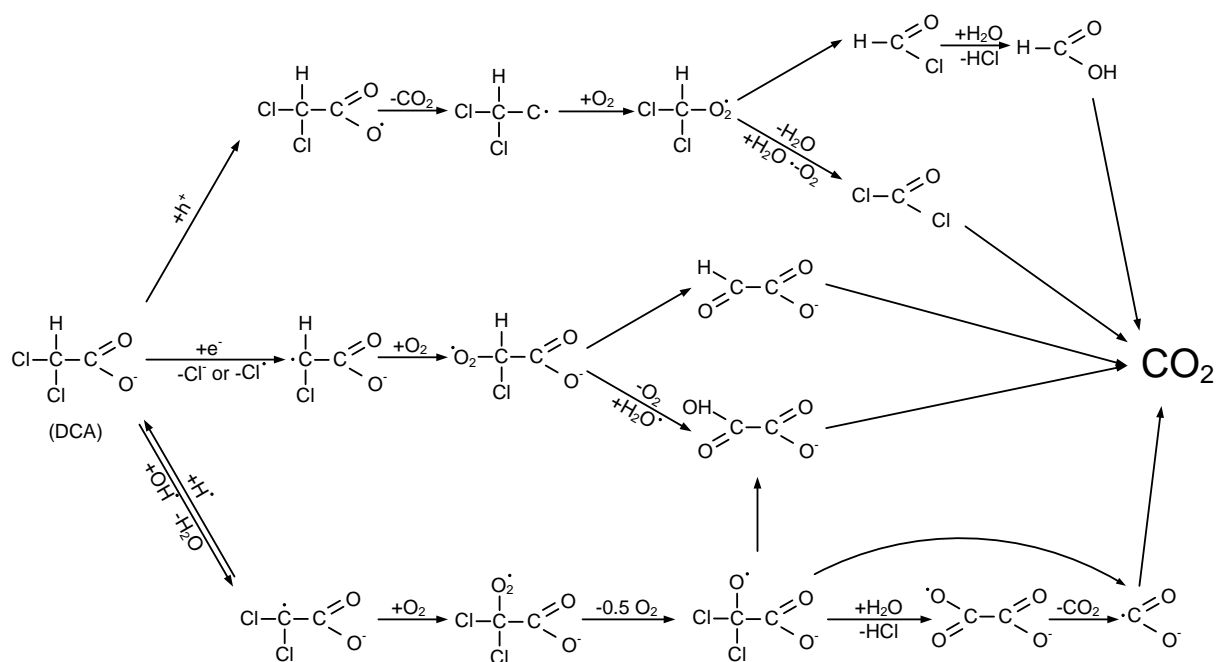


Fig. 2.3: Mechanism of photocatalytic degradation of dichloroacetic acid [44]

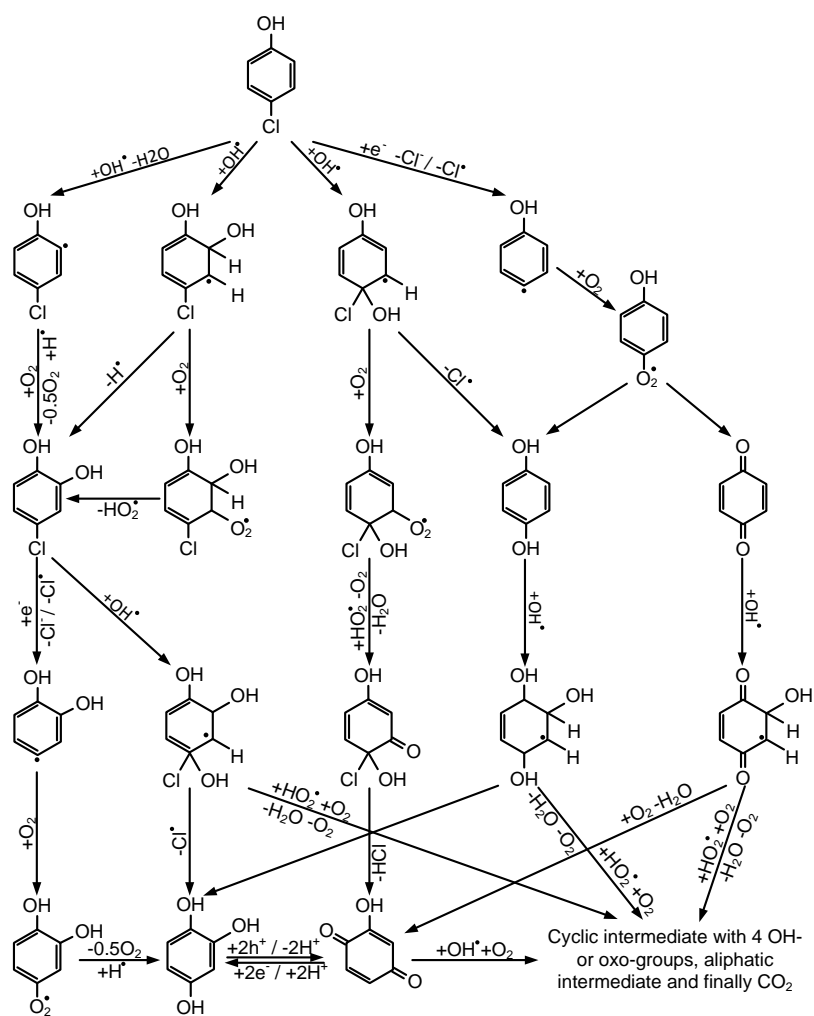


Fig. 2.4: Mechanism of photocatalytic degradation of 4-chlorophenol [44]

In general, the kinetics of the photocatalysis can be described with a Langmuir-Hinshelwood (LH) model, when the following assumptions are made [45, 46]:

- 1) At equilibrium the number of adsorption sites on the particle surface is constant
- 2) One adsorption site can absorb only one molecule and the catalyst surface can be covered to the maximum by one layer
- 3) The adsorbed molecules do not affect each other
- 4) Adsorption is reversible
- 5) The energy of adsorption is always the same and does not depend on surface coverage degree

In this case the classical Langmuir adsorption model can be simplified as shown in the following equation [45]:

$$r = -\frac{dC}{dt} = \frac{k_r \cdot K_{LH} \cdot C}{1 + K_{LH} \cdot C} \quad (2.18)$$

For low initial reactant concentration, equation 2.18 can also be simplified to an apparent first-order equation [45]:

$$\ln\left(\frac{C_0}{C}\right) = k_r \cdot K_{LH} \cdot t = k_{app} \cdot t \quad (2.19)$$

Where C is the concentration of the reactant (mg/l/min); t the reaction time; k_r the constant of reaction rate (mg/l/min); K_{LH} the adsorption constant of the reactant (l/mg); C_0 the initial concentration of the reactant and k_{app} the apparent first-order rate constant.

2.3 TiO₂ nanoparticles

TiO₂ belongs to the family of semiconductors, which is characterized by an unoccupied conduction band just like insulators. In comparison to insulators the band gap energy of semiconductors is so small, that electrons can be excited from the valence band to the next higher unoccupied conduction band with relative low energy. Based on this effect TiO₂ is usually used as photocatalyst.

TiO₂ is a white powder used as a pigment in paint because of its high refractive index since the 19th century. After the discovery of Fujishima and Honda [47] in 1972 that water molecules can be splitted on TiO₂ electrodes under UV light, TiO₂ particles, in particular at the nano-scale, have become more interesting for application in areas such as photovoltaic, self-cleaning coating and antibacterial surface.

2.3.1 Structural properties of TiO₂

TiO₂ is known to be polymorphic and has three modifications named anatase, rutile and brookite, which are different in their crystal structure, as shown in Fig. 2.5. A similarity in the crystal lattice of all modifications is that each titan ion is surrounded by an octahedron of six oxygen ions and each oxygen ion belongs to three octahedrons, so that the stoichiometric ratio between titan and oxygen ions is maintained by 1:2.

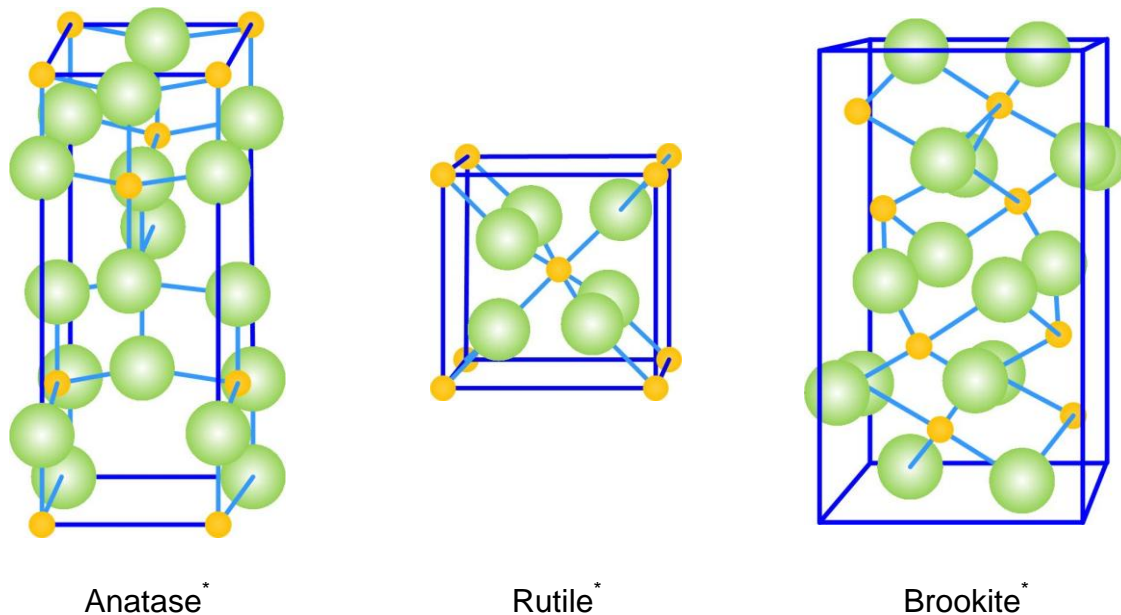


Fig. 2.5: Crystal structure of anatase, rutile and brookite (* green ball is oxygen ion and orange one is titan ion) [48]

The difference between the three crystal structures is the distortion of each octahedron and the assembly pattern of the octahedron chains [38, 49]. Rutile shows

a tetragonal crystal structure and the TiO_6 octahedron in rutile is slightly distorted. Anatase also has a tetragonal crystal structure but the octahedron in anatase is significantly distorted. Brookite shows an orthorhombic structure formed by a distorted octahedron with a titan ion at the center and oxygen ions at each of the six vertices. Moreover, the octahedron in rutile is connected by edge-sharing of two oxygen pairs, in brookite by edge-sharing of three oxygen pairs and in anatase by edge-sharing of four oxygen pairs. The increase of sharing edges causes increased repulsion between ions in the crystal structure because of a decrease of the distance between the ions. All the described differences result in different mass densities and electronic band structures between the three modifications of TiO_2 .

2.3.2 Synthesis of TiO_2

In generally, TiO_2 can be synthesized by wet chemical approaches or aerosol processes. In comparison with the aerosol process, the synthesis of TiO_2 via wet chemical processes has advantages of allowing control over the stoichiometry, production of homogeneous materials, formation of complex shapes and preparation of composite materials [50]. The wet chemical processes are mostly used for the industrial manufacturing of pigmentary TiO_2 particles with large particle size in micrometer range, which is usually referred to the sol-gel processing [49-51]. However, the TiO_2 particles from wet chemical processes are usually amorphous or with low crystallinity resulting in low photocatalytic activity [51]. Moreover, these processes are mainly batch processes requiring tedious post-steps, such as separation, washing, drying and calcination and producing high volumes of waste water as well as a byproduct.

Aerosol processes offer advantages over the wet chemical processes for the fabrication of nanoparticles with high production rate and purity at low cost, such as carbon black, fumed silica and alumina [7, 34]. Very recently, aerosol processes have been developed for manufacturing of TiO_2 nanoparticles using flame reactors, for example, the well-known product TiO_2 P25 from Evonik, which is synthesized with the chloride process by the oxidation of TiCl_4 . Flame synthesis is a scalable, continuous and well-established method and produces about 90 % (by value and

volume) of aerosol-made productions [52]. Depending on the mixing type of fuel and oxidation gas, the flame reactors can be divided into diffusion flame reactors and premixed flame reactors. In the diffusion flame, the fuel gas and oxidant gas do not contact until they leave the burner, whereas in premixed flame they are already mixed before they are delivered into the burner. Furthermore, depending on the precursor state fed to the flame the flame synthesis can be classified in vapor-fed flame synthesis and liquid-fed flame synthesis [7]. Flame synthesis offers advantages that for the particle production the particle properties like particle size, particle morphology, phase composition and crystallinity can be easily controlled and particles with complex structure (e.g. core-shell structure) can be easily achieved.

Ulrich is one of the first researchers studying the basic mechanisms of formation and growth of submicron silica particles by flame synthesis [53, 54]. Fig. 2.6 shows the basic steps for particle formation and growth by gas-to-particle conversion in a flame.

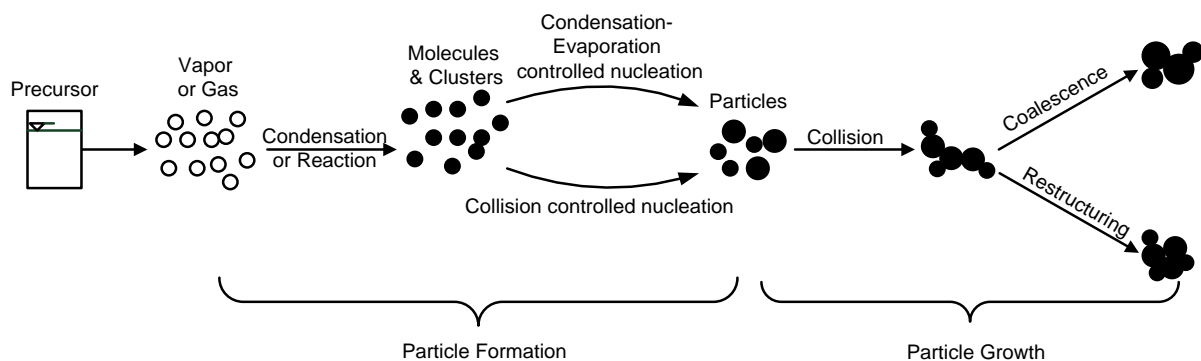


Fig. 2.6: The basic steps for particle formation and growth by vapor-fed flame synthesis (adapted from Camenzind [55], Chang et al. [56] and Nakaso et al. [57])

The vapor-fed flame synthesis is one of the gas-to-particle conversions offering the advantages to build particles from individual molecules all the way up to the desired size. For the particle formation high energy is required to initiate and sustain the chemical reaction, for example, flame synthesis uses the energy of a high temperature flame to generate product molecules and clusters, which can form particles either by condensation-evaporation controlled nucleation or collision controlled nucleation. The nucleation process in flames can be described with the classical theory of homogenous nucleation for material system where the critical

particle size is much larger than the size of a monomer. For the synthesis of TiO_2 nanoparticles by titanium tetrachloride oxidation the critical particle size of TiO_2 is much less than the size of a monomer [58]. Depending on the process temperature and precursor feed rate, the newly nucleated particles grow further by collisions with product molecules and/or with particles (coagulation) [59]. In the case of the vapor-fed flame synthesis coagulation plays a more important role than the surface condensation [53]. Coagulation refers to the growth process by particle collision and/or coalescence. As the generated particles leave the high temperature zone and cool down to low enough temperature, they show soft agglomerate structure consisting of small primary particles. Otherwise, particles grow further by coalescence and/or restructuring depending on the residence time and flame temperature. In this case, the particle size and morphology ultimately is determined by the ratio of collision time τ_c and sintering time τ_s [60]. Collision preferentially occurs at low flame temperatures and/or short residence times of particles in the flame resulting in fractal agglomerates ($\tau_c < \tau_s$). In contrast, sintering is favored at high flame temperatures and/or long residence times causing large primary particles with spherical structure ($\tau_c > \tau_s$).

In the initial stages of particle formation of TiO_2 particles synthesized in a flame reactor by oxidation of TiCl_4 , the mean free path of gas molecules is much higher than the critical particle size of TiO_2 particles. Therefore, according to the collision/sintering theory, the average primary particle size of TiO_2 , d_p , can be calculated as a function of residence time for the free molecular regime by the assumption that the spherical particles grow by coagulation because of the high concentration in the initial stages [61, 62]:

$$d_p = 1.88 \cdot \left(\frac{6 \cdot k_B \cdot T}{\rho_p} \right)^{0.2} \cdot (V \cdot t)^{0.4} \quad (2.20)$$

where k_B is the Boltzman's constant, T the flame temperature, ρ_p the density of TiO_2 , V is the total aerosol volume per unit of gas and t is the residence time of TiO_2 particle in the flame.

By the vapor-fed flame synthesis the density of TiO_2 particles can be considered as constant, because they are not porous. As the flow rate of fuel gas is kept constant and its oxidation is complete, the flame temperature also can be taken as constant

for a given total gas flow rate. For the premixed flame the flame length as well as the residence time of TiO_2 particles in the flame is also constant, since the total gas flow is kept constant. Hence, the average primary size of TiO_2 particles made in a premixed vapor-fed flame is only dependent on the total aerosol volume per unit volume of total gas. It means that increasing the precursor feed rate leads to an increase of the particle size caused by the increased total aerosol volume per unit gas volume [13].

$$d_p \propto (V)^{0.4} \quad (2.21)$$

For the dynamic description of particle growth one simple method named monodisperse model can be applied on basis of the assumption that the particle size distribution remains monodisperse throughout the particle generation process involving concurrent gas phase chemistry and particle transport [63]. Therefore, the time change of TiO_2 particle concentration can be described with the equation below [64]:

$$\frac{dN}{dt} = I - \frac{1}{2} \cdot \beta \cdot N^2 \quad (2.22)$$

Where N is the TiO_2 particle number concentration, I is the nucleation rate of TiO_2 particles, β is the monodisperse collision frequency for coagulation spanning from free molecular to continuum regime. Moreover, β is a function of the average particle size [64]:

$$\beta = 8 \cdot \pi \cdot D \cdot d_p \cdot \left(\frac{d_p}{d_p + \sqrt{2} \cdot g} + \frac{4 \cdot \sqrt{2} \cdot D}{c \cdot d_p} \right) \quad (2.23)$$

Where D is the diffusion coefficient, c is the velocity of particle and the parameter g is given by [64]:

$$g = \frac{1}{3 \cdot d_p \cdot l_a} \cdot \left[(d_p + l_a)^3 - (d_p^2 + l_a^2)^{3/2} \right] - d_p \quad (2.24)$$

With l_a is the mean free path for the TiO_2 particles.

The first term on the right side in equation (2.22) represents the particle formation rate by gas phase oxidation over a wide range of conditions, whereas the second term on the right side stands for the loss of particles by coagulation. The equation (2.25) describes the particle formation rate by gas phase reaction. Ulrich has

reported that the coagulation is much more important than surface reaction in the particle growth process [53]. When the surface reaction is neglected, the equation (2.25) can be simplified as shown in equation (2.26):

$$I = k_g \cdot C \cdot N_{av} = (k - k_s \cdot A) \cdot C \cdot N_{av} \quad (2.25)$$

$$I = k_g \cdot C \cdot N_{av} = k \cdot C \cdot N_{av} \quad (2.26)$$

With k_g being the gas phase reaction rate constant, C the TiCl_4 precursor concentration, N_{av} the Avogadro number, k the overall oxidation rate constant of TiCl_4 , k_s the surface reaction rate constant and A the total surface area concentration of TiO_2 particle.

2.3.3 Thermodynamic stability of TiO_2

Generally, rutile is recognized to be the most stable phase of TiO_2 at most temperatures and pressures [48]. Anatase transits irreversibly to rutile at temperatures above 400 °C, which results in a loss of the desired photocatalytic properties for the applications of TiO_2 particles at high temperature processes. Zhang and Banfield [65] have reported that the thermodynamic phase stability is dependent on the particle size. For equally sized particles, anatase is the most stable phase for particles smaller than 11 nm and rutile is the most stable for particles larger than 35 nm. They have also reported that a critical particle size dominates the phase transformation from anatase to rutile. For anatase particles in the few nanometer range the surface energy is lower than that of comparable rutile particles causing lower total free energy (contributed by solid and surface energy) of anatase. Anatase shows a higher solid energy than rutile, but a lower surface energy, which compensates for small particles. According to the fact that every system aspires to the lowest energy state, anatase transforms to rutile when it grows to a critical size where the higher surface energy is not sufficient to compensate the lower solid energy of rutile [66].

According to the studies of Zhang and Banfield [19, 20, 65], the critical particle size for the phase transformation is 14 nm, which is in agreement with the studies of Hu et

al. [23] and Kobata et al. [24] reporting that the critical particle size is around 15 nm. Kobata et al. have simulated the phase transformation from anatase to rutile in a tubular reactor. If the activation energy for the phase transformation is above 400 kJ/mol, the rutile mass fraction increases with increasing temperature and/or the time of heat treatment. Shannon and Pask [67] have reported that the rate of phase transformation exhibits a S-curved shape along with the heat treatment time. In the first stage of the phase transformation the nucleation rate of rutile is linear and this stage is named accelerating step. In the second stage of the phase transformation on the S-curve, the phase transformation rate decreases with the time, which is named decelerating step. They have also pointed out that the phase transformation is initiated by the nucleation of rutile on the surface of anatase, followed by the growth of rutile towards the particle interior [24], as shown in Fig. 2.7.

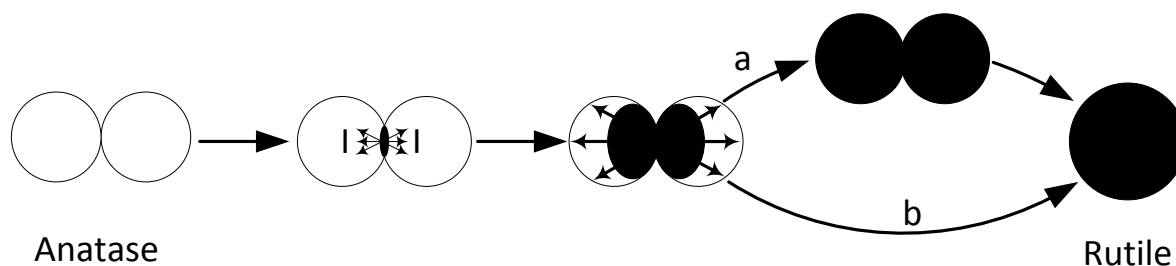


Fig. 2.7: Schematic diagram showing the steps of anatase-to-rutile phase transformation (I is the nucleation rate of rutile, a represents the phase transformation over short time and b over long time) (adapted from Zhang et al. [68])

In order to extend the application of photoactive TiO_2 particles at high temperatures, the anatase particles can be stabilized with metallic and non-metallic additives. Periyat et al. [69] showed that the TiO_2 particles are stable at 1000 °C with 15 mol% silica addition. The same results were obtained by He et al. [70]. They have pointed out that the thermostability of TiO_2 increases with increased silica amount. Okada et al. [28] have studied the effect of silica additive on the stabilization of anatase particles performance in liquid phase. They have found that the SiO_2 formed smooth layer on the anatase particle surface and with 5 wt. % SiO_2 additive the anatase particles showed stability up to 1000 °C, which is consistent with the conclusion from Hofer et al. [37] and He et al. [70]. It should be noted that the structure of the

stabilized particles affects strongly on the thermostability of TiO_2 particles. Like the studies mentioned above, the TiO_2 particles show high thermostability up to 1000 °C, because after heat treatment SiO_2 formed a layer on the TiO_2 surface for a core-shell structure preventing the phase transformation and particle growth.

2.3.4 Synthesis of SiO_2 coated TiO_2

In order to extend the application of photoactive TiO_2 particles at high temperatures, the anatase particles can be stabilized by wet chemical route [17, 25] or gas phase route [36, 71]. Because the wet chemical route is very complex and expensive, the simple gas phase method has attracted more interest. As shown in Fig. 2.8 the synthesis of SiO_2 coated TiO_2 via the wet chemical route is compared with the synthesis via the gas phase route. In industry the coating process of the flame made pigmentary TiO_2 particles via wet chemical processes contains several steps. The flame made TiO_2 particles are firstly dispersed and grinded in a liquid to assure that all particles will be coated. Finally the coated particles have to be filtered from the liquid and dried. In contrast the coating of TiO_2 particles can be achieved in one step by flame synthesis. In this case, the TiO_2 particles are firstly synthesized in the flame and simultaneous coated with SiO_2 by introduction of Si-precursor into the reaction zone, as shown in Fig. 2.8.

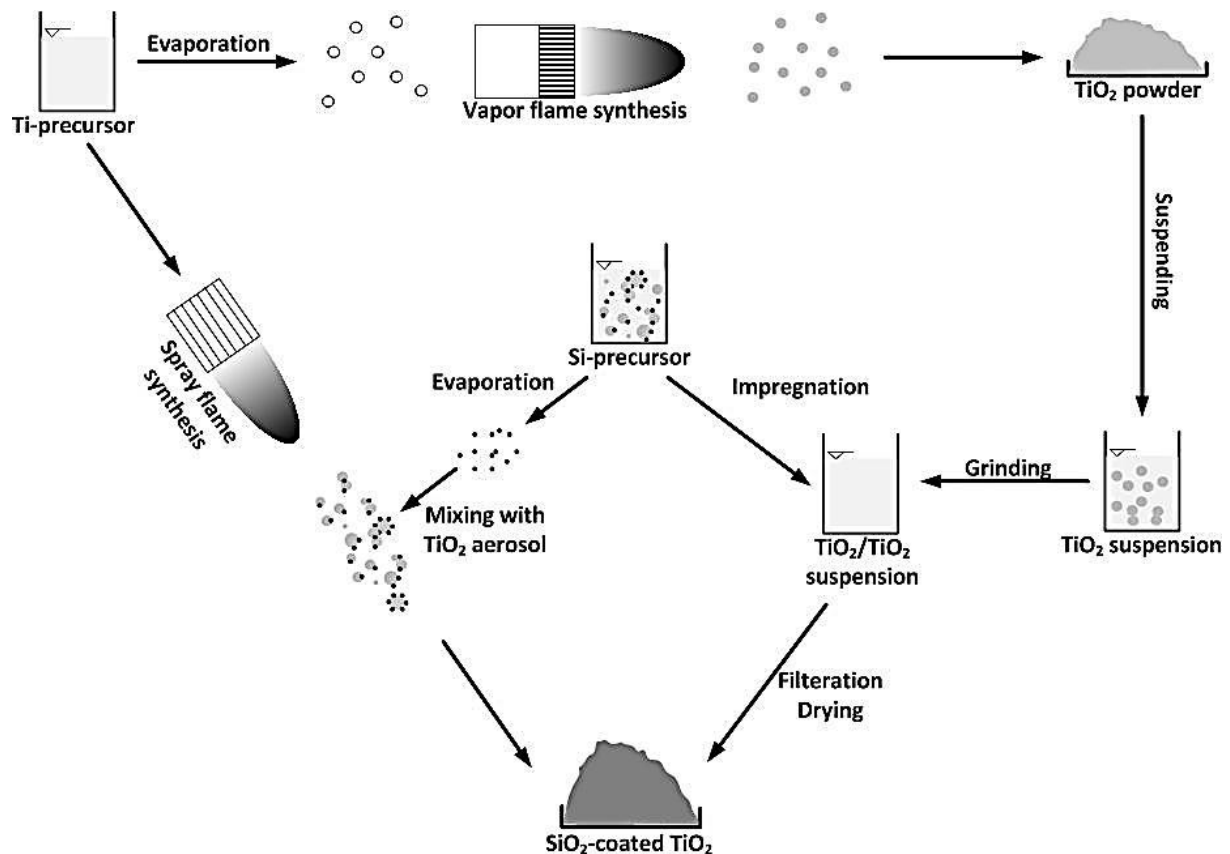


Fig. 2.8: Comparison of the methods for synthesis of SiO_2 coated TiO_2 particles via wet chemical route and gas phase route adapted from [29]

Hung et al. [32] have synthesized $\text{TiO}_2/\text{SiO}_2$ particles in a rectangular counterflow diffusion H_2/O_2 flame. They concluded that increasing the residence time and /or increasing the reaction temperature is favored to form smooth SiO_2 coatings at high SiO_2 loading and at low SiO_2 loading TiO_2 particles could be coated with discrete SiO_2 particles. Powell et al. [71] synthesized SiO_2 coated TiO_2 particles in a hot wall reactor, in which the possible coating mechanism is illustrated in Fig. 2.9. They have studied the influence of reaction temperature and SiO_2 loading on the coating structure and concluded that high temperature (1500 °C) is favored to form uniform films on TiO_2 surface and at low temperature of 1300 °C the TiO_2 surface became rough because of the deposition of silica particles. The group of Kodas [72-73] have introduced a model and also experiments for online coating of TiO_2 particles with SiO_2 in a hot wall reactor. They found that at low temperature of 1300 °C rough SiO_2 coatings were obtained, because the temperature was not enough which caused low sintering rates. Increasing the SiO_2 loading resulted in thicker SiO_2 coatings, but they

were also rough. Smooth SiO_2 coatings on TiO_2 surface were achieved at high temperature of $1500\text{ }^\circ\text{C}$ because of increased sintering rates. However, at this temperature the SiO_2 coatings did not increase as the SiO_2 content increased which was consumed by gas to particle conversion to form SiO_2 particles. Teleki et al. [29, 36] have also successfully synthesized SiO_2 coated TiO_2 particles in one step by flame spray pyrolysis and checked the coating quality by analyzing the isoelectric point of powders. They found that the isoelectric point of the $\text{TiO}_2/\text{SiO}_2$ particles is shifted to the value of SiO_2 , when the SiO_2 amount increased. It indicates that the thickness of SiO_2 coating increased with increased SiO_2 content. Therefore, the morphology of $\text{TiO}_2/\text{SiO}_2$ particle as well as the structure of SiO_2 on TiO_2 surface is strongly dependent on the reactor type, temperature for reactions, precursor feed rate, particle mixing, residence time, cooling rate of particles and so on, which are finally attributed to the particle collision and sintering rate.

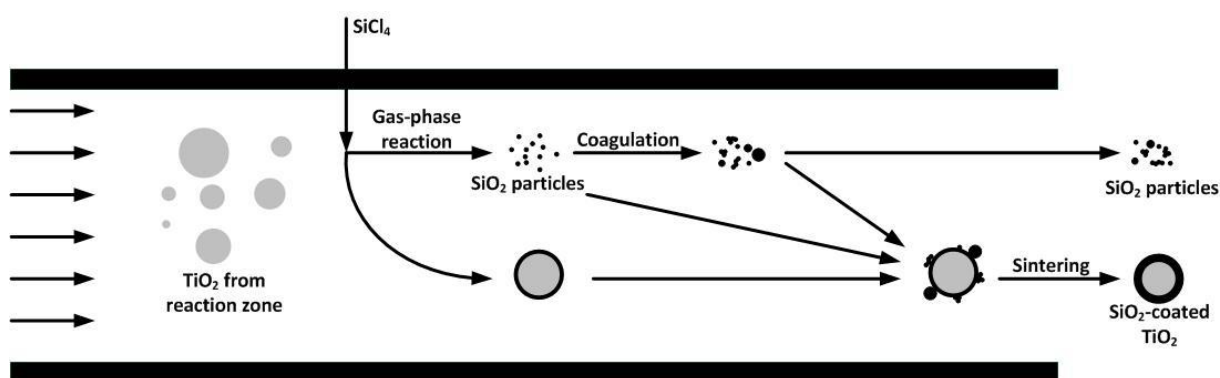


Fig. 2.9: Coating mechanism in a hot wall reactor [73]

2.3.5 Photocatalytic activity of TiO_2

The influences on the photocatalytic activity of TiO_2 can be subdivided into intrinsic parameters of the photocatalyst properties and extrinsic parameters of the experimental conditions. Because there are many variables affecting the photocatalytic activity of TiO_2 such as particle size, phase composition, crystal structure, pH of solution and preparation method of particles [16, 74-76], in the present work only the influence of particle size, particle morphology and phase composition on the photocatalytic activity is discussed.

The particle size is a crucial parameter affecting the photocatalytic activity of TiO_2 . Reducing the particle size, results in more specific surface area for the photocatalytic reaction offering more adsorption sites on the photocatalyst surface for reactant molecules. According to the study of Hagfeldt et al. [77], the transit time of the charge carriers from the particle interior to the surface decreases with decreasing particle size, which results in a reduction of the volume recombination rate of the charge carriers. However, for nanoparticles with decreasing particles size an increase of the surface recombination rate of the charge carriers is also observed. The charge carriers are generated near the particle surface and can diffuse quickly to the particle surface and recombine with each other because of the existence of many defects (traps) and the lack of a driving force for charge separation. Therefore, there should be an optimum particle size for the maximum photocatalytic activity.

In addition, extremely small nanoparticles are within the transition region between molecules and solids. When the particle size of the semiconductor commensurate with the de-Broglie-wavelength of the charge carriers, they behave like a giant atom and their energy levels are quantized. This effect is called quantum size effect, which enlarges the band gap of semiconductors [4, 39] (Fig. 2.10). Therefore, the particles showing the quantum size effect are not desired for the photocatalytic application of TiO_2 photocatalysts.

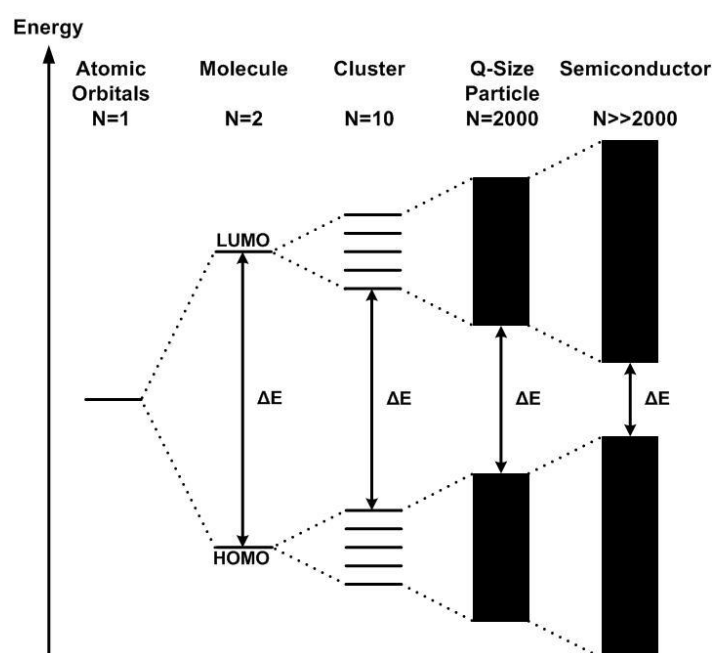


Fig. 2.10: Electronic structure of semiconductor as a function of monomeric units [4, 39]

TiO₂ exists in nature with different modifications of anatase, rutile and brookite, which have different contributions to the photocatalytic performance. Theoretically brookite because of nearly the same band gap as anatase shows the same or a slightly lower photocatalytic activity as anatase. However, for photocatalytic applications only anatase and rutile are considered.

Amorphous TiO₂ shows a negligible photocatalytic activity [78]. It is assumed that the defects in amorphous TiO₂ increase the recombination rate of charge carriers causing the reduction of the photocatalytic activity [79].

Tanaka et al. have reported that pure anatase exhibit an excellent photocatalytic activity, while pure rutile shows a very poor photocatalytic activity [80]. The difference of the photocatalytic ability between anatase and rutile is due to their different conduction and valence band edges. In anatase the generated electrons and holes have sufficient over-potentials to electron acceptor or donors, respectively. But in the case of rutile, only holes have a sufficient over-potential to electron donors because the conduction band of rutile is about 0.3 eV more positive than that of anatase, which results in a higher recombination rate of charge carriers [39, 81]. In addition, the adsorption of O₂ on rutile is lower than that on anatase because of its crystal structure. This also leads to an increased recombination rate of charge carriers [45, 82].

3 Experimental section

3.1 Chemicals

As precursor for the flame synthesis of TiO_2 and $\text{TiO}_2/\text{SiO}_2$ nanoparticles titanium tetrachloride (TiCl_4) and silicon tetrachloride (SiCl_4) from Sigma Aldrich with a purity > 99.9% were used. The flame and carrier gases methane, oxygen, nitrogen and argon were purchased from Linde and the purity class of these gases is 4.5.

As a model substance dichloroacetic acid (DCA, Riedel-de Haen with a purity > 99%) and 4-chlorophenol (4-CP, Sigma-Aldrich with a purity of 99%) were used to determine the photocatalytic activity of TiO_2 nanoparticles. To evaluate the photocatalytic activity of the particles prepared by flame synthesis and the effect of the SiO_2 additive on the stabilized anatase particles the commercial product titanium dioxide Aeroxide® P25 (Evonik), having an average primary particle size of 21 nm and an anatase content of 80 wt.%, was used as reference material.

3.2 Synthesis of TiO_2 nanoparticles

The experimental setup for the synthesis of TiO_2 nanoparticles in a laminar premixed flame is shown in Fig. 3.1, which was described in detail in the reference [83].

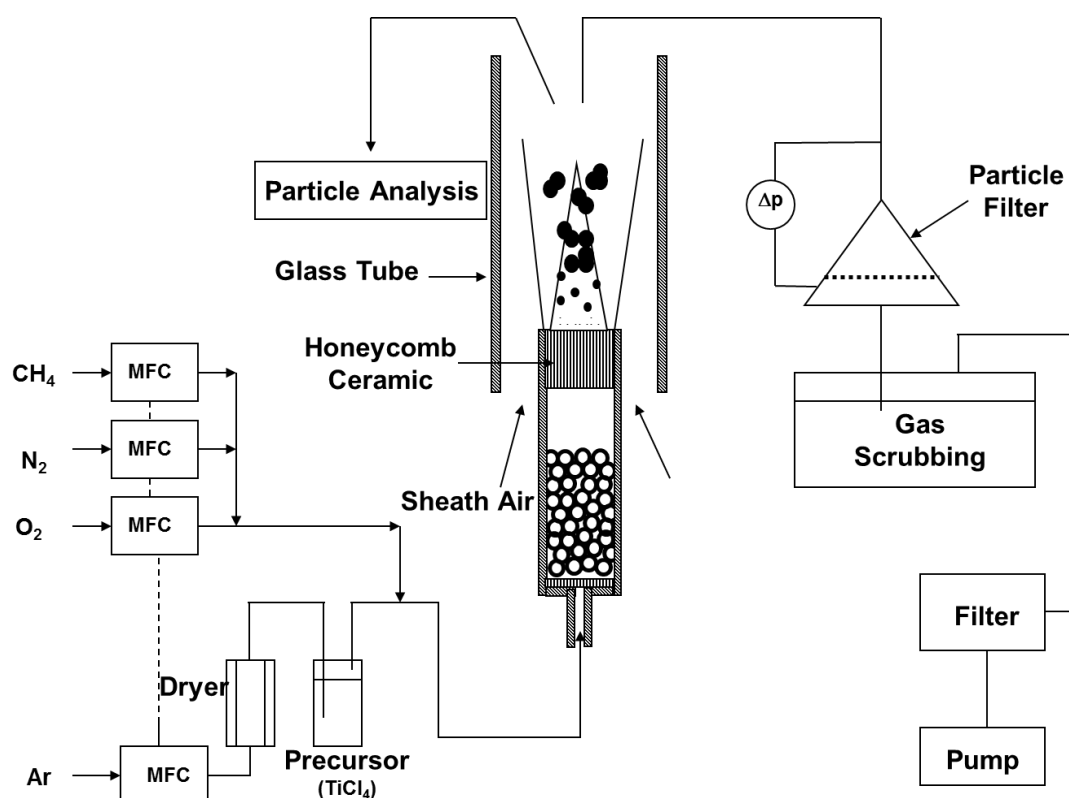


Fig. 3.1: Schematic diagram of the experimental setup for the synthesis of TiO_2 nanoparticles [83]

The apparatus mainly consists of a TiCl_4 evaporator, burner, particle collector and exhaust gas clean-up unit. The burner is made of a quartz glass tube (inner diameter 18 mm, length of 100 mm) filled with 4 mm quartz glass spheres and a honeycomb ceramic of channel width 1.55 mm (Type 200 CSI, Rauschert, Germany). Fuel gas (methane) and oxidant (oxygen) were premixed with nitrogen raising the flame above the burner. Titanium tetrachloride vapour was generated by passing dry argon gas through a bubbler containing the liquid precursor at room temperature. Subsequently, the vapour was mixed with the other process gas constituents at room temperature. The gas mixture was then introduced into the burner. The flow rates of all synthesis components were controlled by mass flow controllers. The visible flame height was about 10 mm and the maximum temperature of the flame measured with a thin 1mm K-type NiCr-Ni thermocouple in absence of the titanium tetrachloride vapour was about 1000 °C. The produced TiO_2 particles were collected on a glass fiber filter placed in a stainless steel filter holder connected to a vacuum pump. The filter was positioned about 50 cm above the glass tube on the flame. The chloride containing

byproducts were removed from the exhaust gas by passing through a sodium hydroxide solution. The produced TiO_2 particles were collected on a glass fiber filter placed in a stainless steel filter holder connected to a vacuum pump. The filter was positioned about 50 cm above the glass tube on the flame. The chloride containing byproducts were removed from the exhaust gas by passing through a sodium hydroxide solution.

Tab. 3.1: Synthesis conditions of TiO_2 nanoparticles

Sample	CH_4	O_2 [l/h]	Ar/TiCl_4 [l/h]	TiCl_4 [mmol/min]
S1	25	110	2.5	0.021
S2	25	110	3	0.025
S3	25	110	5	0.042
S4	25	110	8.5	0.071
S5	25	110	12	0.101
S6	25	110	26	0.218
S7	25	110	40	0.336
S8	25	110	60	0.504

Tab. 3.1 lists the experimental conditions used for the particle syntheses of samples S1 to S8. All experiments were performed at fixed flow rates of methane and oxygen: 25 l/h and 110 l/h, respectively. For the flame synthesis oxygen was introduced into the flame above the stoichiometric amount to ensure a complete combustion of methane. The Ar/TiCl_4 flow rate was varied between 2.5 and 60 l/h, which corresponds to a TiCl_4 feed rate in the range between 0.021 and 0.504 mmol/min, whereas total gas mixture flow rate was kept constant (380 l/h) by appropriate adjustment of the nitrogen flow rate. As the total gas mixture flow rate was kept constant, constant residence time and flame temperature for all syntheses were achieved.

3.3 Synthesis of $\text{TiO}_2/\text{SiO}_2$ nanoparticles

The experimental setup for the synthesis of highly thermally stable TiO_2 nanoparticles with SiO_2 additive in a premixed flame is shown in Fig. 3.2, which is similar to Fig. 3.1 and described in detail in the reference [84].

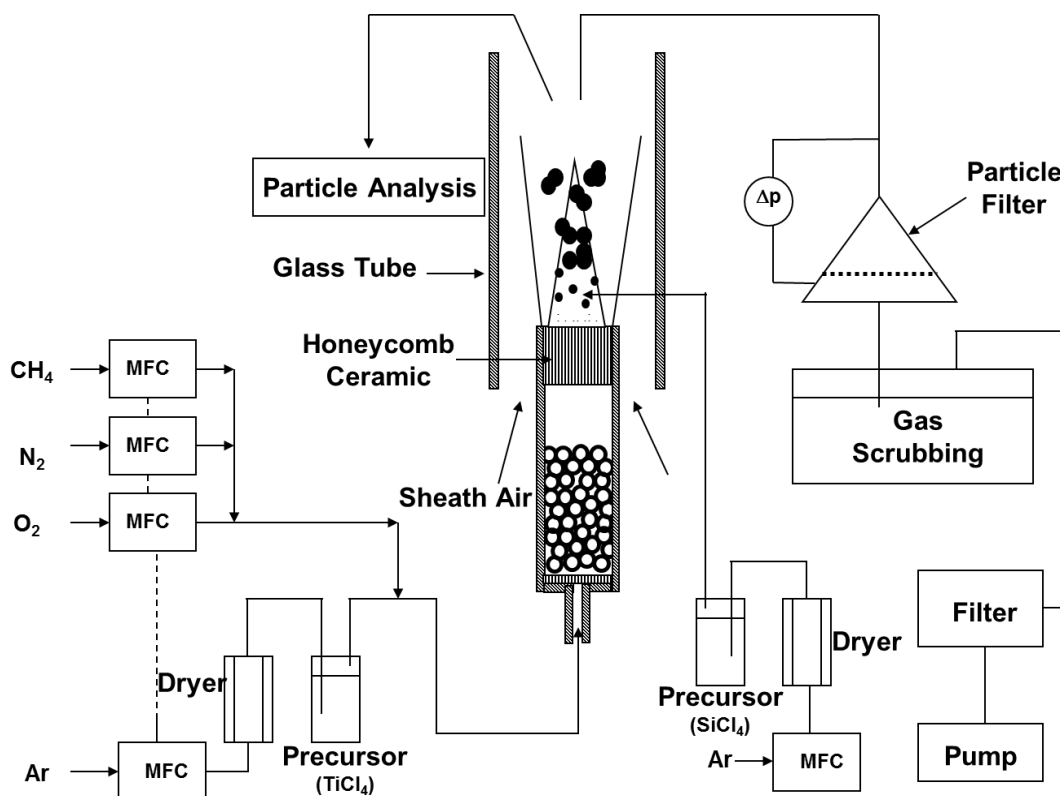


Fig. 3.2: Schematic diagram of the experimental setup for synthesis of $\text{TiO}_2/\text{SiO}_2$ nanoparticles [84]

To stabilize the TiO_2 particles, the second precursor SiCl_4 was delivered directly into the flame, where TiO_2 particles had been already formed. Thus, the SiO_2 can condense on the surface of TiO_2 particles.

The feed rate of TiCl_4 precursor introduced into the flame was kept constant at 0.218 mmol/min. The amount of SiCl_4 was varied in this study between 0.023 and 2.057 mmol/min by changing the carrier gas flow rate of Argon for the SiCl_4 precursor from 0.1 l/h to 9 l/h. The corresponding ratio between TiO_2 and SiO_2 is between 0.11 and 9.65 mmol/mmol, which is listed in Tab. 3.2.

Tab. 3.2: Synthesis condition of TiO₂/SiO₂ nanoparticles

Sample	Ar/TiCl ₄ [l/h]	Ar/SiCl ₄ [l/h]	SiCl ₄ [mmol/min]	Si/Ti [mmol/mmol]
P1	26	0.1	0.023	0.11
P2	26	0.2	0.046	0.22
P3	26	0.3	0.069	0.32
P4	26	0.4	0.091	0.43
P5	26	0.6	0.137	0.64
P6	26	0.8	0.183	0.86
P7	26	1.6	0.366	1.71
P8	26	2	0.457	2.15
P9	26	3	0.686	3.22
P10	26	6	1.371	6.44
P11	26	9	2.057	9.65

The generated TiO₂/SiO₂ particles were also collected on a glass fibre filter placed in a stainless steel filter holder connected to a vacuum pump and the filter holder was fixed about 50 cm above the flame. The exhaust stream from particle collection unit was then passed through a sodium hydroxide solution.

3.4 Calcination of TiO₂/SiO₂ samples

To determine the thermostability of TiO₂/SiO₂ particles, the samples synthesized in the flame reactor were calcinated at 900 °C, 1000 °C, 1050 °C, 1100 °C, 1150 °C and 1200 °C, respectively. According to the industrial manufacture of ceramic roof tiles with a self-cleaning surface in one step, the calcination of the TiO₂/SiO₂ particles was carried out in a muffle furnace with a heating rate of 5 °C/min. The calcination began from room temperature and was kept at the desired temperature for 3 hours.

For comparison with the synthesized particles the reference material TiO₂ P25 was also calcinated up to 900 °C to observe the change of phase composition and particle morphology as well as particle size.

3.5 Particle Characterization

3.5.1 BET

The specific surface area (SSA) of the synthesized powders was determined at the Institute of Particle Technology from a five-point nitrogen adsorption isotherm obtained from Brunauer-Emmett-Teller (BET) measurements using a Gemini 2360 (Micromeritics, USA). Prior to analysis the powders were degassed at 120 °C for two hours. Additionally, the equivalent diameter d_{BET} was calculated using the BET results.

$$d_{BET} = \frac{6000}{\rho_{TiO_2} \cdot SSA} \quad (3.1)$$

Where ρ_{TiO_2} is the density of TiO₂ powder.

3.5.2 X-Ray Diffraction

The phase composition of synthesized powders was analyzed by X-Ray Diffraction (XRD) using a Siemens D5000 Kristalloflex instrument at the Institute of Non-Metallic Materials with scanning range from 15 to 70° 2 θ at a step size of 0.04°. The major characteristic peaks of anatase and rutile are located at 2 θ = 25.3 °C and 2 θ = 27.5 °C, respectively, as shown in Fig. 3.3.

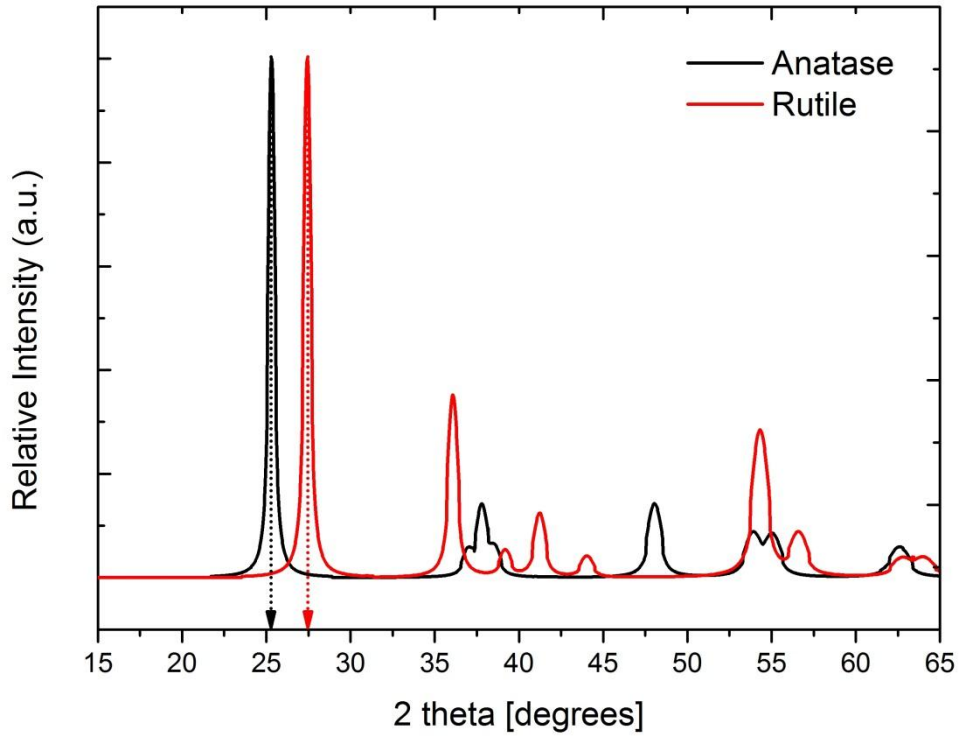


Fig. 3.3: XRD patterns of anatase and rutile

The relative weight fractions of anatase and rutile phase were determined using Rietveld full-profile refinement with Topas R Software per following equations [85]:

$$x_A = \frac{1}{1 + (1.26 \cdot \frac{I_R}{I_A})} \quad (3.2)$$

$$x_R = \frac{1}{1 + (0.8 \cdot \frac{I_A}{I_R})} \quad (3.3)$$

where x_A , x_R are the relative weight fraction of anatase and rutile, I_A and I_R are the relative intensity of reflection of anatase and rutile, respectively.

Furthermore, the crystal size d_{XRD} was determined by the Scherrer's equation [86]:

$$d_{XRD} = \frac{K \cdot \lambda}{\beta \cdot \cos \theta} \quad (3.4)$$

where λ is the wavelength of the X-ray radiation ($\lambda = 154.056$ pm), K the Scherrer constant ($K = 0.91$), θ the characteristic X-ray diffraction peak ($\theta = 12.7^\circ$) and β is

the full-width-at-half-maximum of the (101) plane after correcting with instrumental broadening using the Warren function.

3.5.3 Transmission Electron Microscope

The morphology of powders was observed with a transmission electron microscope (TEM, JEM 2100, JEOL) operated at 120 kV at the Insitute of Particle Technology. The particles were deposited on a carbon coated copper grid. For the determination of the average particle size d_{TEM} , as well as the primary particle size distribution, around 1000 particles were carefully measured from different region on the TEM grid. For exact observation of the TiO_2 sintering process and examination of the change of SiO_2 shell, the flame synthesized powders were analyzed in TEM upon online heating. For this case platinum grids with three slits were used to avoid the interruption from the grid, (Fig 3.4, left). The particles were firstly deposited on the platinum grids and then the grids were fixed on a heating stage connected to the sample holder (Fig. 3.4, right). Since the sample holder is placed in TEM, the particle can be heated via temperature controller. With this method man can observe the sintering process of the same particles and the change of particle structure upon heating for a long time.

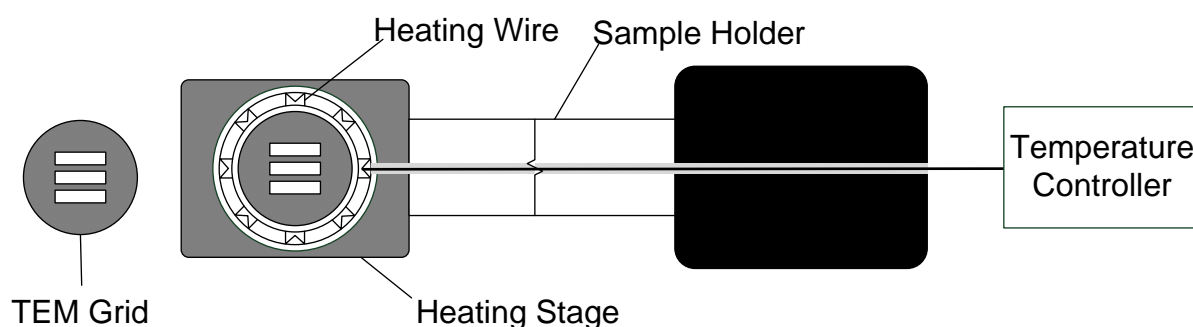


Fig. 3.4: Diagram of platinum grid and a TEM sample holder with heating function for online observation

3.5.4 Scanning Electron Microscope

The morphology of self-cleaning coatings was investigated at the Insititute of Non-Metallic Materials with a scanning electron microscope (SEM, Cam Scan C54). The coatings were completely dehydrated and then fixed on the sample holder. Subsequently, the samples were sputtered with a thin layer of gold or carbon to avoid the static electricity effect for increasing the image quality. The operation of SEM was carried out by 10 kV and also three dimensional images of the sample were provided. Due to the high resolution of SEM the structure of the cracks and pores are clearly visible.

3.6 Photocatalytic activity tests

The photocatalytic activity of synthesized TiO_2 materials as well as of commercial TiO_2 P25 was evaluated at the Insititute of Non-Metallic Materials by the mineralization of two model organic pollutants in a slurry-type photoreactor: DCA and 4-CP with initial concentrations of 5 and 1.7 mmol, respectively. The corresponding initial total organic carbon (TOC) concentration of DCA and 4-CP solutions was approximately 120 mg/l. The experiments were conducted at pH = 3.0 (adjusted with HNO_3) and at photocatalyst loading of 0.3 g/L. The effect of experimental conditions on the photocatalytic decomposition of DCA and 4-CP as well as the description of major reaction pathways were reported in detail elsewhere [14, 87-89].

A cylindrical immersion photochemical reactor with a capacity of 1 L was used as a reaction vessel. The reaction solution was kept at 20 °C in a thermostat and continuously purged with oxygen. Dark adsorption step was performed for 30 min prior to illumination. A 500 W iron doped Hg medium pressure lamp (Heraeus, Germany) was employed as UV-A light source. The major part of short-wave-length UV- and IR-radiation was eliminated by a borosilicate cooling jacket (water as cooling fluid) surrounding the lamp. In the present study the progress in photocatalytic degradation reaction was monitored by measuring the decrease in TOC in the range down to $\text{TOC} \approx 2$ ppm measured with Analytic-Jena IDC-micro N/C TOC-Analyzer calibrated for concentrations in the range from 1 to 1000 ppm.

The process for the determination of the photocatalytic activity of $\text{TiO}_2/\text{SiO}_2$ samples is similar to that of the TiO_2 samples. The difference is that the photocatalytic activity of $\text{TiO}_2/\text{SiO}_2$ particles was only evaluated for the model substance DCA. The photocatalytic tests were also performed in aqueous phase by monitoring the changes of total organic carbon values of DCA. The initial concentration of the DCA solution was 5 mmol and the TiO_2 loading used was 0.5 g/L. The tests were performed in a 0.40 L capacity batch glass vessel supplied with magnetic stirrer. A UV-A light with an intensity of 6.5 mW/cm^2 was positioned over the glass vessel. Following photocatalytic oxidation, TOC of treated solution was measured by Analytic-Jena IDC-micro N/C TOC-Analyzer.

4 Results of pure TiO₂ and binary TiO₂/SiO₂ nanoparticles

In the following section on the results, the physical and photocatalytic properties of pure TiO₂ nanoparticles as a function of particle size, which is adjusted by the TiCl₄ precursor feed rate, will be discussed first. Then, staying with the active TiO₂ nanoparticles, the effect of the SiO₂ additive on the thermostability and photocatalytic activity of binary TiO₂/SiO₂ nanoparticles will be investigated. Finally, the photocatalytic activity of thin self-cleaning films made of the active and stable TiO₂/SiO₂ nanoparticles for the decomposition of DCA will be explored in the next chapter.

4.1 Pure TiO₂ nanoparticles

4.1.1 Effect of precursor feed rate on specific surface area

Fig. 4.1 shows the specific surface area and the BET-equivalent diameter of the TiO₂ nanoparticles synthesized with various precursor feed rates of TiCl₄ (cf. Tab. 3.1).

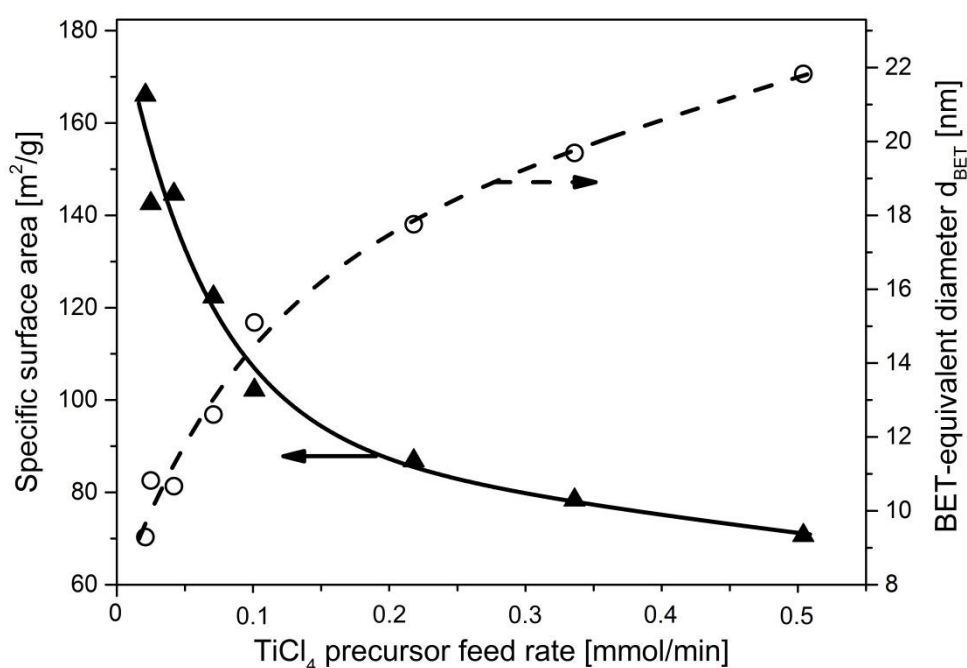


Fig. 4.1: The specific surface area and BET-equivalent diameter of flame synthesized TiO₂ particles as a function of TiCl₄ precursor feed rate

The specific surface area of flame synthesized TiO₂ nanoparticles exponentially decreases and the BET equivalent diameter exponentially increases with increasing precursor feed rate, as shown in Fig. 4.1. Unlike the synthesis of TiO₂ particles in a diffusion flame reactor [13, 33], the flow rate of oxidant in a premixed flame reactor has no influence on the particle size as well as the specific surface area [13, 90, 91]. In this study an oxygen rich flame was used and the total gas amount (380 l/h) and the fuel gas amount (25 l/h) were kept constant. Therefore, the flame height and the residence time of the particles in the flame were also constant. Despite the fact that the oxidation of TiCl₄ precursor is exothermic, the enhancement of the flame temperature by introduction of TiCl₄ precursor into the flame is negligible, because the combustion enthalpy is very low ($\Delta H_{c(TiCl_4)} = -140$ kJ/mol). On the other hand, increasing the TiCl₄ precursor feed rate leads to an increase of the number of TiO₂ particles per unit gas volume, which results in an increasing collision rate between TiO₂ particles and hence in larger particles. Therefore, when increasing the precursor feed rate of TiCl₄ from 0.021 to 0.504 mmol/min, the average diameter of TiO₂ particles from BET analysis is increased from about 9 to 21 nm (Fig. 4.1, dashed line) by assuming the particles to be spherical. The specific surface area of TiO₂ particles decreases exponentially from ca. 166 m²/g at 0.021 mmol/min to ca. 70 m²/g at 0.504 mmol/min (Fig. 4.1, solid line). This trend is consistent with the reported results of Jang et al. [16]. It should be noted here that the specific surface area of synthesized samples in the premixed flame is much higher than the reference material TiO₂ P25 from Evonik showing a specific surface area of about 50 m²/g.

4.1.2 Effect of precursor feed rate on phase composition

Fig. 4.2 illustrates the X-ray diffraction patterns of the reference material TiO₂ P25 and the flame made samples S1, S4 and S8 (cf. Tab. 3.1). The X-ray diffraction patterns show two main peaks at 25.3° and 27.5°, which correspond to anatase and rutile, respectively. According to the manufacturer data of the reference material, TiO₂ P25 consists of about 80 wt.% anatase and 20 wt.% rutile, as shown in Fig. 4.2.

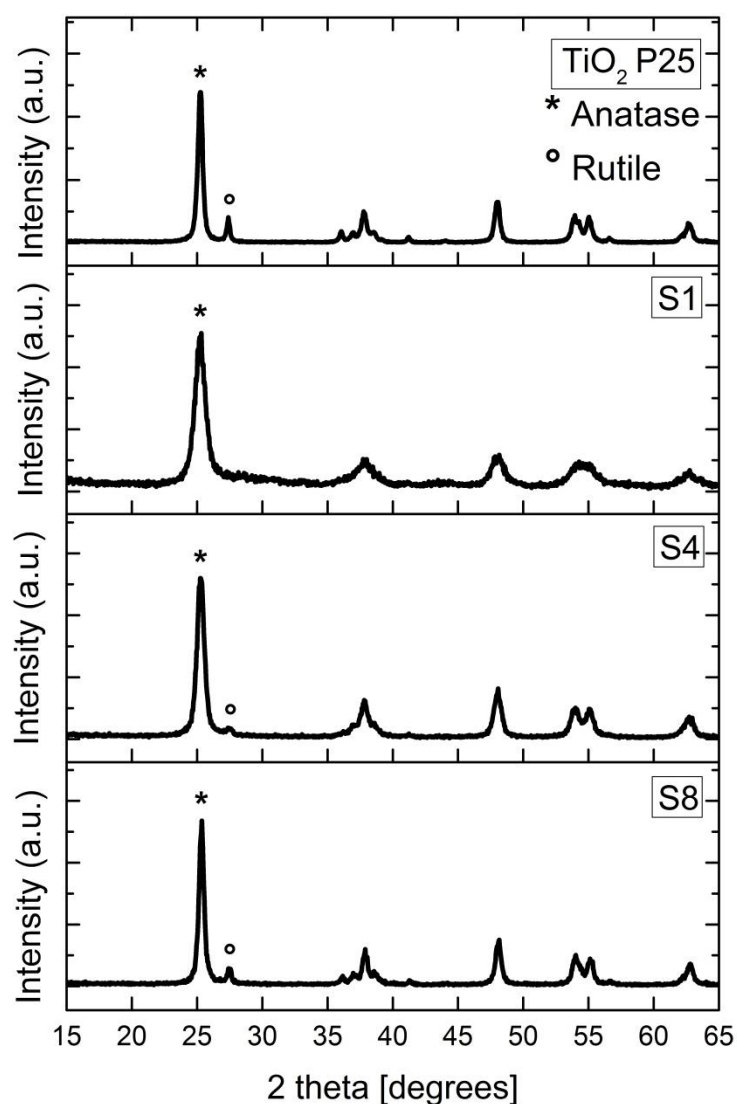


Fig. 4.2: X-ray diffraction patterns of the reference material TiO₂ P25 and the flame made samples S1 (TiCl₄: 0.021 mmol/min), S4 (TiCl₄: 0.071 mmol/min) and S8 (TiCl₄: 0.504 mmol/min)

The variation of TiCl₄ precursor feed rate strongly affects the anatase and rutile mass fraction of the flame made TiO₂ samples. It was found that anatase is the predominant phase in flame made samples. For sample S1 with low precursor feed rate there is no rutile peak observable indicating that this sample is composed of anatase only. Increasing the precursor feed rate increases the intensity of the rutile peak in the XRD patterns from S1 to S8.

Fig. 4.3 shows the effect of the precursor feed rate on the anatase mass fraction in flame made samples and the calculated XRD-equivalent diameter of TiO₂ particles.

As the precursor feed rate increases from 0.021 mmol/min to 0.504 mmol/min, the mass fraction of anatase decreases from 100 wt.% to ca. 90 wt.%, while the XRD-equivalent diameter of TiO₂ particles determined with Scherrer's equation increases from ca. 7 nm to ca. 17 nm. Compared to the reference material TiO₂ P25, the flame made TiO₂ samples consist of less than 10 wt.% rutile, because the process parameters of the experiments are favourable for the synthesis of small anatase particles, for example, the maximal flame temperature is only about 1000 °C. This result is in agreement with the experimental and simulated results of Kobata et al. [24]. The low flame temperature for the oxidation of TiCl₄ precursor leads to a low coagulation and sintering rate of particles, which results in small particle size and a slow phase transformation from anatase to rutile.

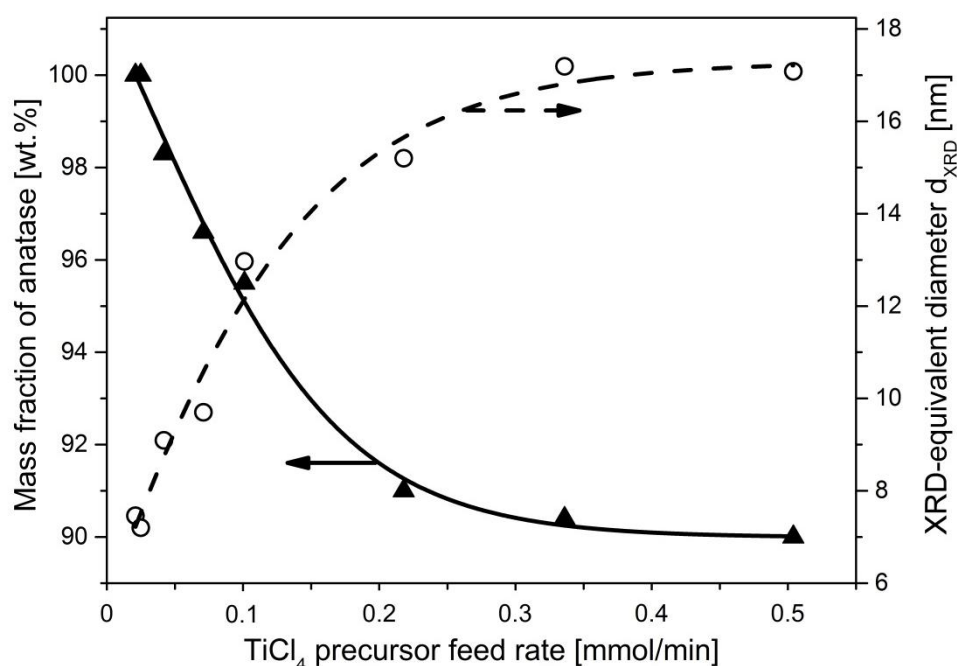


Fig. 4.3: The effect of the precursor feed rate on the anatase mass fraction and XRD-equivalent particle size

4.1.3 Effect of precursor feed rate on particle morphology and size

Studies [16, 56, 75, 76] have shown that the particle morphology and the particle size are crucial parameters for the TiO₂ photocatalytic properties. Fig. 4.4 shows the

particle morphology and the primary particle size distribution of the reference material TiO₂ P25 and the flame made samples. For the determination of the primary particle size distribution about 1000 particles were carefully counted and measured from many TEM images of a sample, which were taken at different regions on the TEM grids.

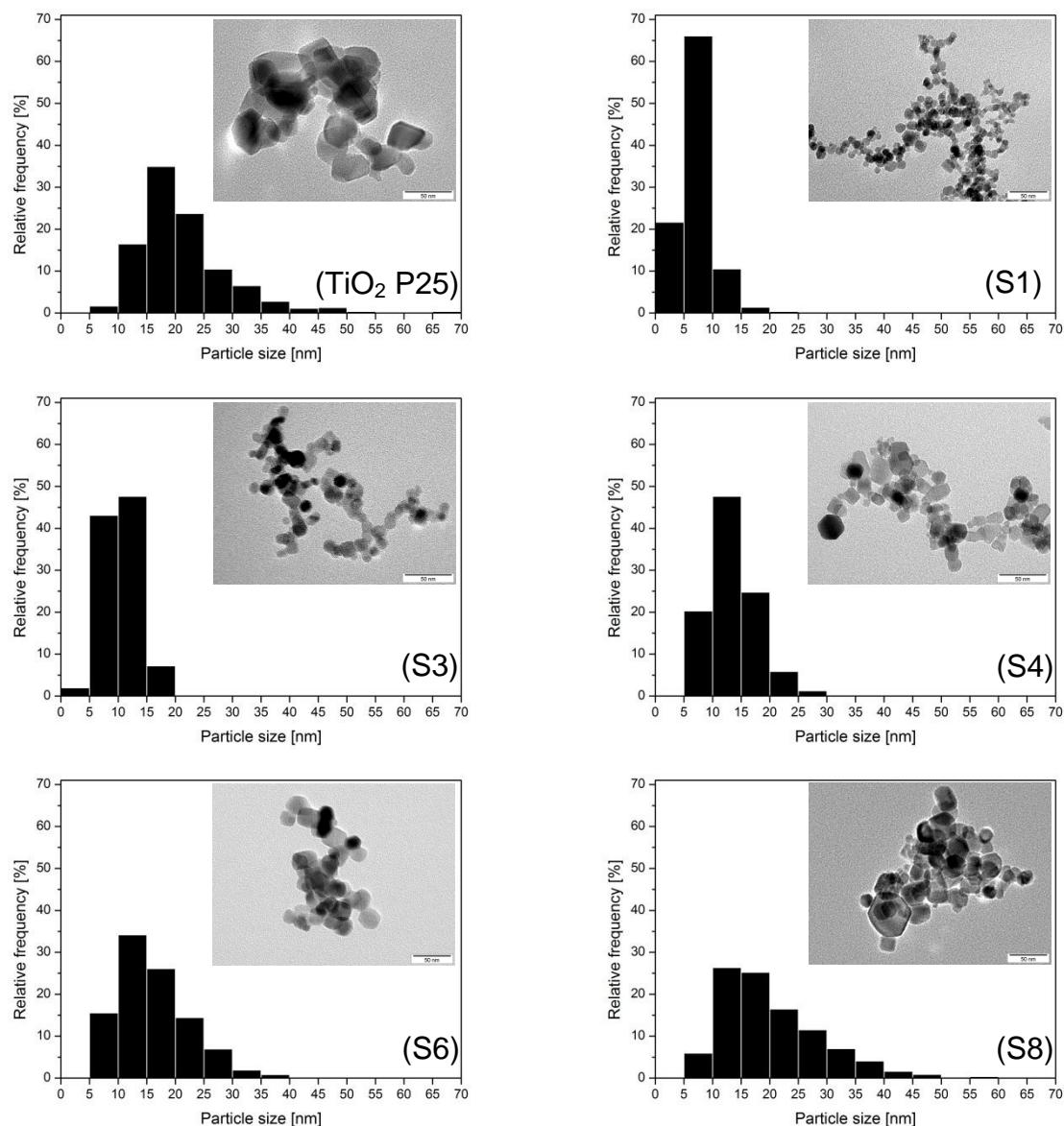


Fig. 4.4: Particle morphology and primary particle size distribution of TiO₂ P25 and flame made samples with precursor feed rate of 0.021 mmol/min (S1), 0.042 mmol/min (S3), 0.071 mmol/min (S4), 0.218 mmol/min (S6) and 0.504 mmol/min (S8), respectively

The particles of the reference material TiO₂ P25 are polyhedral, which are more active than spherical particles with the same size [74-76]. The average particle size determined from TEM images is about 21 nm with a particle size range between 5 and 70 nm. The particle size distribution is broad and most of the particles are located between 10 and 40 nm (Fig 4.4, TiO₂ P25). The Figure 4.4 (S1 to S8) shows the effect of TiCl₄ precursor feed rate on the particle morphology and particle size distribution. The flame made samples are also polyhedral and show a chain-like structure like the morphology of TiO₂ P25 and the precursor feed rate has no significant effect on the particle morphology, as displayed in the inserted TEM images. The samples S1 to S3, which are synthesized at low precursor feed rate, consist of particles smaller than 20 nm and the particle size distributions are very narrow. However, as the precursor feed rate increases, the particle size distribution becomes broader and shifts to bigger sizes. As shown in Fig. 4.5, increasing the precursor feed rate from 0.021 mmol/min to 0.504 mmol/min, the calculated average particle size increases from 7.27 nm to 20.56 nm.

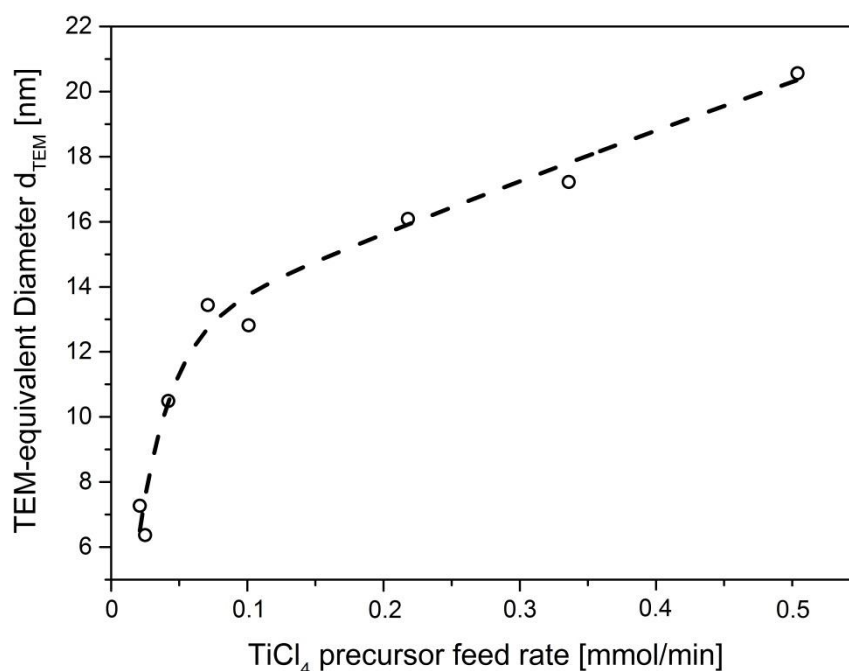


Fig. 4.5: The effect of the precursor feed rate on the TEM-equivalent particle size

The sample S8 with feed rate of 0.504 mmol/min shows a similar particle size distribution and the same average particle size as the reference material TiO₂ P25. It

should be noted that the predominant particle fraction in samples S1 to S8 is switched also to bigger size with increased precursor feed rate. For the sample S1 the predominant particle fraction is about 65 % located between 5 nm to 10 nm. Sample S4 shows the maximal particle fraction of about 50 % in the range between 10 nm to 15 nm and in the sample S8 there are two maximal peaks of particle fraction between 10 nm to 20 nm. It is known that the photocatalytic activity of TiO₂ is size dependent. Therefore, in the discussion the photocatalytic activity of TiO₂ particles in every fraction will be discussed.

4.1.4 Effect of precursor feed rate on photocatalytic performance

The photocatalytic performance of the flame made TiO₂ samples and the reference material TiO₂ P25 was tested for the decomposition of DCA and 4-CP in the liquid phase under the irradiation with UV-A light and illustrated in Fig. 4.6. The reference material TiO₂ P25 is known to be very active as confirmed by the measured degradation of DCA of about 89% in 75 minutes. Sample S1 shows inferior photocatalytic activity to the reference material TiO₂ P25 as in 75 minutes about 85 % DCA was decomposed. The most active sample is S4 (corresponding to increased precursor feed rate compared to S1) that degraded about 85% DCA in 30 minutes. With further increased the precursor feed rate (from sample S4 over S6 to S8), the photocatalytic activity of flame made TiO₂ samples decreases but still stays above the photocatalytic activity of TiO₂ P25.

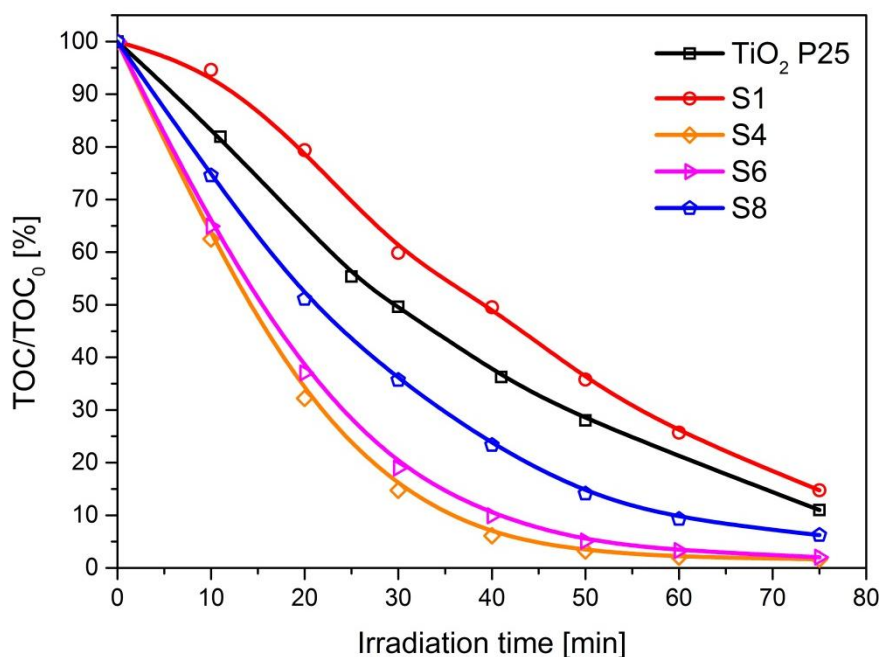


Fig. 4.6: Photocatalytic degradation of DCA with flame made samples of S1 (TiCl₄: 0.021 mmol/min), S4 (TiCl₄: 0.071 mmol/min), S6 (TiCl₄: 0.218 mmol/min) and S8 (TiCl₄: 0.504 mmol/min)

Fig. 4.7 shows the oxidation rate of DCA at 30 minute with flame made TiO₂ as a function of the TiCl₄ feed rate. Increasing the precursor feed rate, the DCA oxidation rate increases until an optimum and then decreases with further increased precursor feed rate. Despite the samples S1 and S2 consist of anatase phase only, they show a DCA oxidation rate at 30 minute of 1.66 and 2.0 mg/(l·min), respectively, which are inferior to the other flame made samples. Although the reference material TiO₂ P25 consists of around 80% anatase, its DCA oxidation rate at 30 minute is 2.17 mg/(l·min), which is higher than that of sample S1 and S2. The most active flame made sample shows a DCA oxidation rate of 3.4 mg/(l·min), which is more than one and a half times as active as the reference material TiO₂ P25.

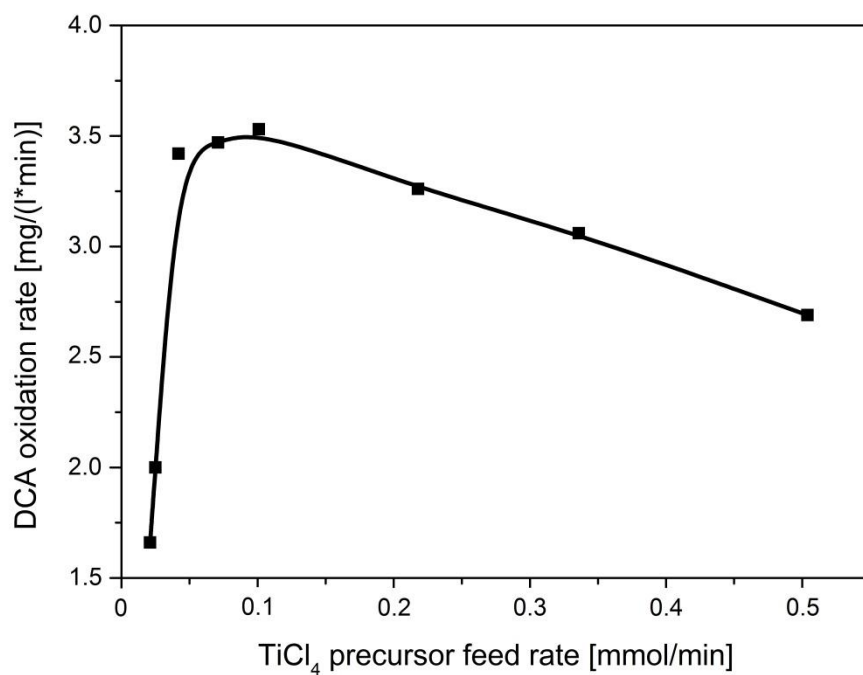


Fig. 4.7: DCA oxidation rate at 30 minute as a function of the precursor feed rate

As shown in Fig. 4.8 and Fig. 4.9, the photocatalytic degradation of 4-CP with the flame made samples compared to reference material shows the same tendency as for DCA.

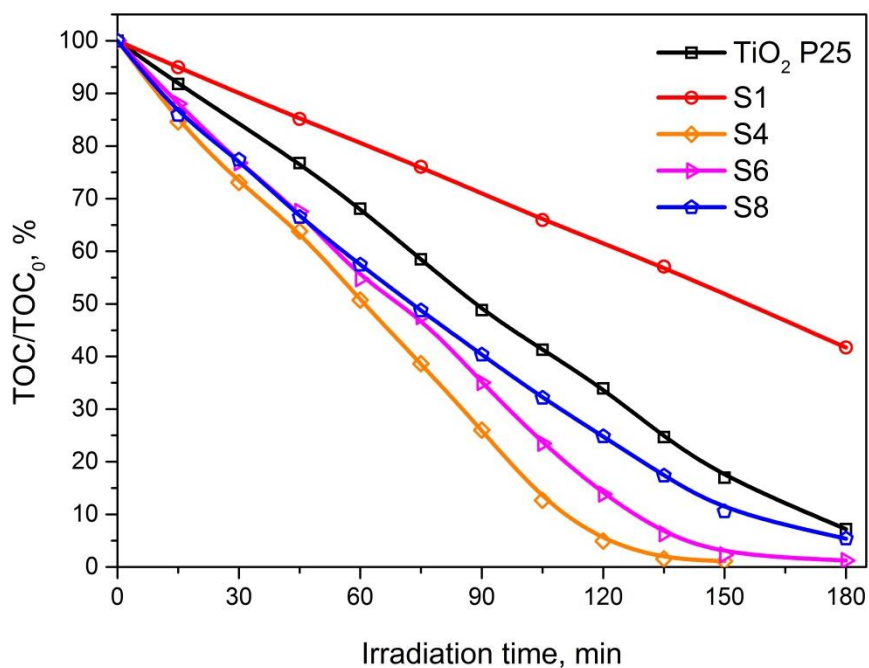


Fig. 4.8: Photocatalytic degradation of 4-CP with flame made samples of S1 (TiCl_4 : 0.021 mmol/min), S4 (TiCl_4 : 0.071 mmol/min), S6 (TiCl_4 : 0.218 mmol/min) and S8 (TiCl_4 : 0.504 mmol/min)

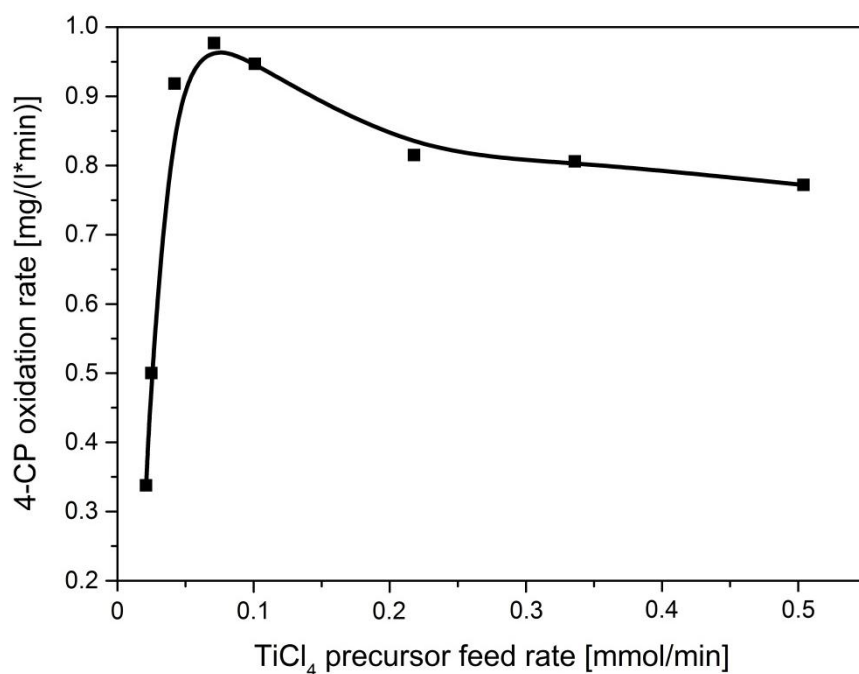


Fig. 4.9: 4-CP oxidation rate at 30 minute as a function of the precursor feed rate

Here should be noted that the oxidation rates of 4-CP at 30 minute with TiO₂ P25 and flame made samples are generally lower than that of DCA. The reason is that the molecule of 4-CP is much larger, more complex and hardly adsorbed on the titania surface compared to DCA molecules [92-95]. For the reference material TiO₂ P25, about 90% 4-CP was decomposed within 180 minute. The flame made sample S1 showed inferior ability for the degradation of 4-CP to the other flame made samples and the reference material. The most active sample is also S4, as shown in Fig. 4.9. The 4-CP oxidation rate with sample S4 shows the highest value of 0.98 mg/(l·min), which is also higher than the 4-CP oxidation rate of 0.69 mg/(l·min) with the reference material.

The photocatalytic activity of pure TiO₂ was evaluated not only for the degradation of DCA and 4-CP in the liquid phase, but also for the decomposition of aliphatic acrylonitrile and aromatic toluene in the gas phase, which is introduced in detail in the reference [96]. For this test the most active sample S4 (TiCl₄: 0.071 mmol/min) was chosen for the degradation of the hazardous air pollutants and compared to the reference material TiO₂ P25 [96]. Because of its small particle size, large surface area and superior structure properties, the sample S4 showed higher ability for photocatalytic degradation of air pollutants than the reference material TiO₂ P25, which is consistent with the results for the degradation of aqueous pollutants.

4.1.5 Discussion

In the present study, the flame synthesized TiO₂ samples were analyzed using three methods for the determination of the equivalent particle size affected by precursor feed rate. The equivalent diameters of TiO₂ particles determined with different methods are listed in Tab. 4.1 for comparison.

Tab. 4.1: Comparison of the equivalent diameter of pure TiO₂ Particles determined from BET, XRD and TEM measurements

Sample	TiCl ₄ [mmol/min]	d _{BET} [nm]	d _{XRD} [nm]	d _{TEM} [nm]	d _{BET} ³ /d _{XRD} ³
S1	0.021	9.30	7.46	7.27	1.94
S2	0.025	10.82	7.20	6.37	3.93
S3	0.042	10.67	9.09	10.49	1.62
S4	0.071	12.61	9.70	13.44	2.20
S5	0.101	15.10	12.97	12.82	1.58
S6	0.218	17.76	15.20	16.09	1.60
S7	0.336	19.68	17.19	17.22	1.50
S8	0.504	21.83	17.08	20.56	2.09

As shown in the Tab. 4.1, the BET-equivalent diameters of samples S1 to S8 are larger than the equivalent diameter determined with TEM. However, the TEM-equivalent diameter of particles is generally recognized to be the accurate value of spherical or sphere-like particles. The difference of the TiO₂ particle diameter obtained by these two methods is that BET analysis corresponds to the area size distribution while the TEM-equivalent diameter corresponds to the number size distribution. On the other hand, the difference is due to the BET-equivalent diameter being calculated with the assumption of spherical particles. In this study, the flame synthesized TiO₂ particles are polyhedral and sphere-like, but not really spherical (Fig. 4.4). Moreover, the pure TiO₂ particles show the morphology of soft agglomerates, which result in a little larger equivalent diameter compared to monodisperse particles with the same specific surface area. In contrast, the XRD-equivalent diameter and TEM-equivalent diameter show a good agreement, which indicates that the TiO₂ particles are single crystals, as shown in Fig. 4.10.

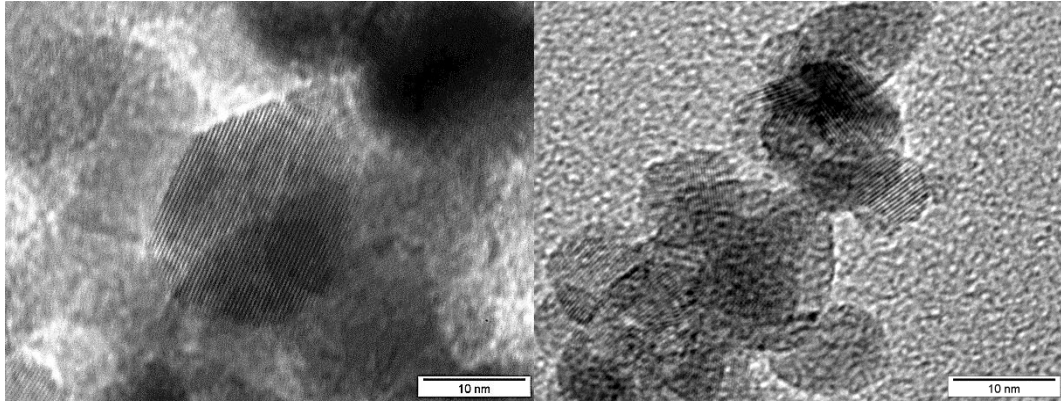


Fig. 4.10: Crystal structure of TiO₂ particles

In addition, the BET equivalent diameter and XRD equivalent diameter can be used for determination of the number of grains per particle N , as a measure for the degree of aggregation with the formula below [90, 97, 98]:

$$N = \frac{d_{BET}^3}{d_{XRD}^3} \quad (4.1)$$

As shown in Tab. 4.1, the degree of aggregation is usually between 1.50 and 2.20 indicating that few of the TiO₂ particles are bonded to each other by sintering necks as aggregate. That can be confirmed by TEM image, as shown in Fig. 4.11. The flame synthesized TiO₂ particles are adhered to each other because of van der Waals force and these loose TiO₂ agglomerates can be well dispersed in water [90].

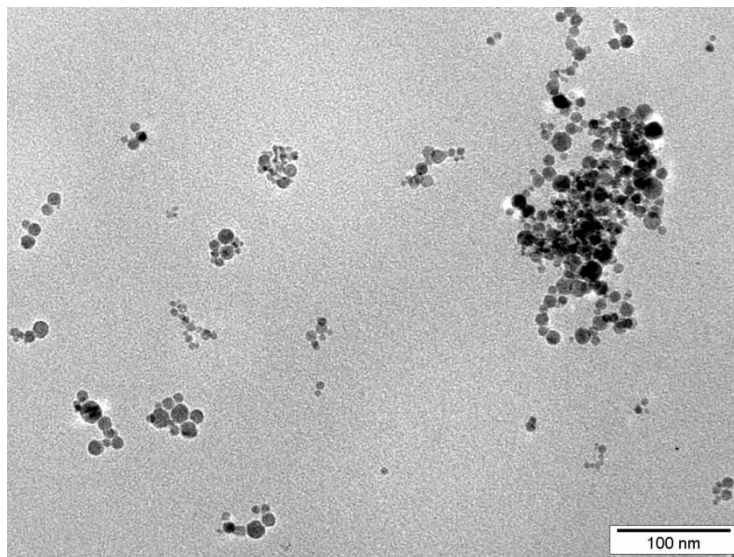


Fig. 4.11: TEM image of non-aggregated TiO₂ nanoparticles made in flame reactor

The particle size is an important parameter for the TiO₂ properties, which is related to the phase composition as well as to the photocatalytic activity of TiO₂ particles. The studies of Zhang et al. [19, 20, 22] showed that a critical particle size is the dominant parameter for the phase transformation, because the surface free energy of anatase is lower than that of rutile. When the particle diameter is smaller than 14 nm, anatase is more stable than rutile. Fig. 4.12 shows the mass fraction of rutile as a function of the TEM-equivalent diameter of TiO₂ particles.

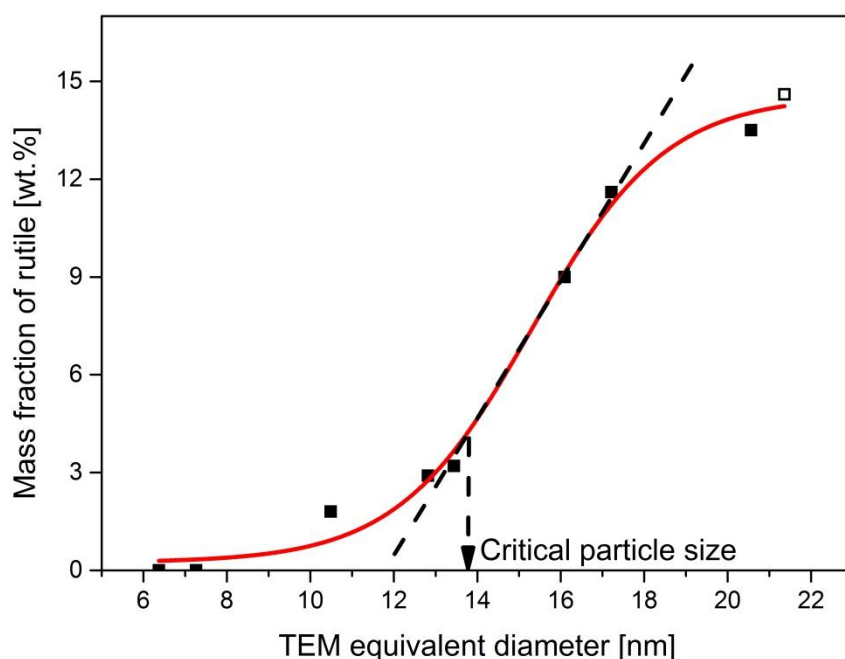


Fig. 4.12: The mass fraction of rutile as a function of the TEM-equivalent diameter of TiO₂ particles (Solid points are the rutile mass fraction of flame made samples and hollow point is for commercial reference material TiO₂ P25)

As shown in this figure, the mass fraction of rutile increases from zero to about 4 wt.% as the average particle size increases from around 7 nm to 14 nm. The particle size of about 14 nm is the critical size of the phase composition, which is in agreement with the studies of Zhang et al.. When the particles are larger than 14 nm, the rutile mass fraction increases significantly. The tendency is also suitable for the reference material TiO₂ P25 (hollow point in Fig. 4.12). However, the flame synthesized pure TiO₂ powders mainly consist of anatase phase. It is contributed to the low flame

temperature and short residence time of particles in the flame. The high anatase mass fraction benefits the high photocatalytic activity of TiO₂ particles.

Generally photocatalytic reactions are very complex and there are numerous parameters that affect the photocatalytic activity of TiO₂, particularly the particle size and phase composition. Many studies have been carried out to investigate the effect of physical and chemical properties of TiO₂ on its photocatalytic activity [13, 16, 75, 76, 99, 100]. Most of them reported that the anatase showed higher photocatalytic activity than rutile. Some reported that the anatase phase containing a small amount of rutile phase exhibited higher photocatalytic activity than that of pure anatase [92]. Until now there is no reliable correlation of photocatalytic activity as a function of particle physical properties. Jang et al. have investigated the influence of particle size and phase composition of TiO₂ on its photocatalytic activity [16]. However, they have found no quantitative correlation between particle properties and photocatalytic activity. In the present study TiO₂ particles with various precursor feed rates are synthesized in order to obtain different phase compositions and primary particle sizes in the premixed flame. By fixing all other parameters the influence of particle size and phase composition on photocatalytic degradation of DCA and 4-CP was investigated using the reaction rate constant.

According to Fig. 4.6, the DCA degradation curves for TiO₂ P25 and flame made samples could be fitted well by an exponential decay curve suggesting first order reaction kinetic, which could be described with the Langmuir-Hinshelwood model. As already mentioned, the model could also be simplified for a low concentration of pollutant as shown below:

$$\ln\left(\frac{TOC}{TOC_0}\right) = -k_{DCA} \cdot t \quad (4.2)$$

Where TOC is the concentration of DCA at time t. TOC₀ is the initial concentration of DCA and k_{DCA} is the reaction rate constant.

The reaction rate constants k_{DCA} of the reference material and flame samples were obtained by plotting the natural logarithm of TOC concentration as a function of irradiation time, as shown in Fig. 4.13. For the photocatalytic test with 4-CP, the decompositions also could be described with the first order reaction kinetic. The reaction rate constant is the most accurate measure of photocatalytic activity of TiO₂

particles, which is not related to the irradiation time compared to the time oxidation rate.

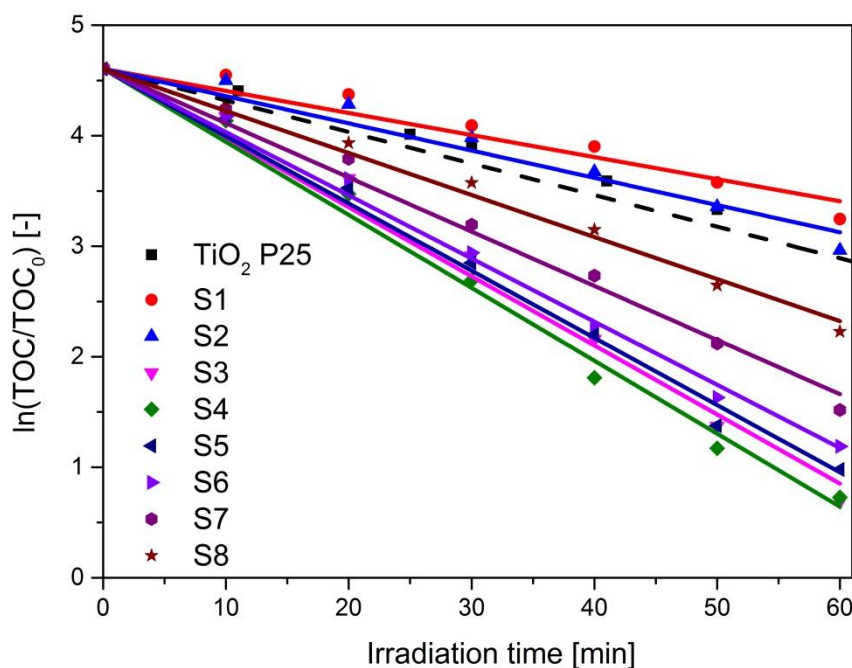


Fig. 4.13: Photocatalytic degradation of DCA with TiO₂ photocatalyst

Fig. 4.14 shows the reaction rate constants k_{DCA} and $k_{4\text{-CP}}$ as a function of anatase mass fraction of TiO₂ particles. The reaction rate constants k_{DCA} and $k_{4\text{-CP}}$ corresponding to the photocatalytic performance of TiO₂ steadily increases with increased anatase mass fraction until a maximum value and subsequently decreases rapidly with further increased anatase mass fraction. This tendency is not only suitable for the flame synthesized samples, but also for the reference material TiO₂ P25 (hollow points in Fig. 4.14). The increase of the reaction rate constant is obviously due to the positive contribution of the increased anatase mass fraction. Decrease of the reaction rate constant with further increased anatase mass fraction seems to be in agreement with the report of Balázs et al. [74]. However, the phase composition of TiO₂ powders depends on the particle size. Therefore, Fig. 4.15 shows the reaction rate constant as a function of the average particle size.

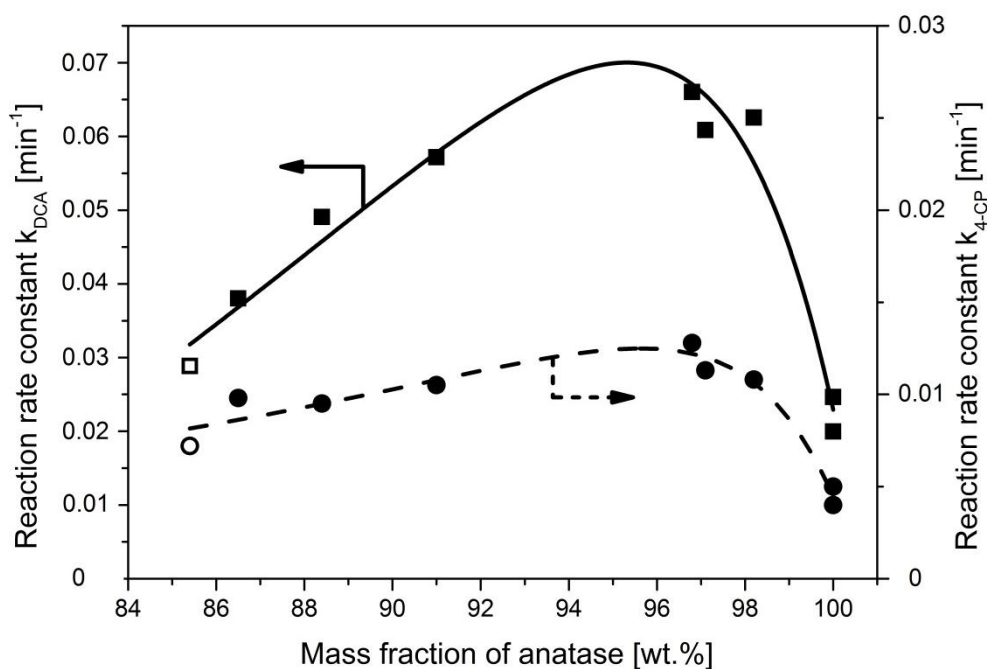


Fig. 4.14: Reaction rate constants k_{DCA} and k_{4-CP} as a function of anatase mass fraction of TiO₂ particles (Solid line is for the reaction rate constants of DCA degradation and dashed line is for the 4-CP degradation; Solid points are the reaction rate constants of flame made samples and hollow points are for TiO₂ P25)

Fig. 4.15 depicts the reaction rate constants of k_{DCA} and k_{4-CP} of the photocatalytic decompositions as a function of the TEM-equivalent diameter of TiO₂ particles. The observation of the influence of average particle size on the photocatalytic activity is based on the same loading of photocatalyst, i.e. the same catalyst mass. Since the UV adsorption of the studied TiO₂ particles is proportional to the particle mass (as shown below), constant loading results in the same UV adsorption [101, 102]. Alike the trend of reaction rate constant with anatase mass fraction, the reaction rate constants of k_{DCA} and k_{4-CP} increases with increased average TEM-equivalent particle size until a maximum at about 14 nm and then decreases with further increased average particle size, which is consistent with the results showed in Fig. 4.14.

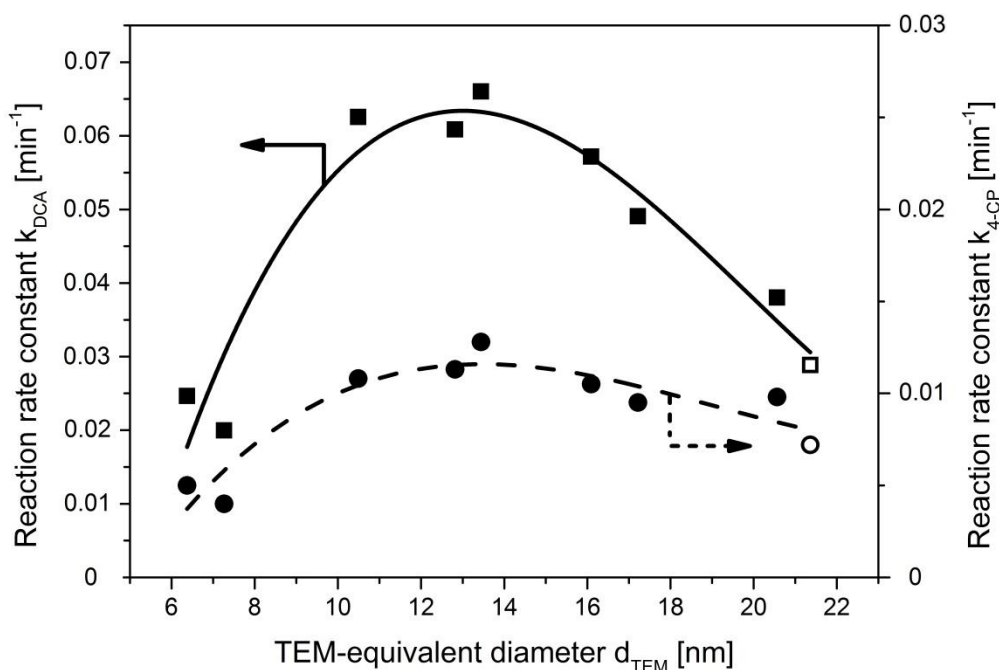


Fig. 4.15: Reaction rate constants k_{DCA} and $k_{4\text{-CP}}$ as a function of average TEM-equivalent diameter of TiO₂ particles (Solid line is for the reaction rate constants of DCA degradation and dashed line is for the 4-CP degradation; Solid points are the reaction rate constants of flame made samples and hollow points are for TiO₂ P25)

The results imply that different particle sizes have different contributions to the photocatalytic ability of TiO₂ particles. When the TiO₂ particles are about 14 nm, they show the highest contribution to the photocatalytic performance, whereas TiO₂ particles are smaller or larger than 14 nm, they show lower contribution to the photocatalytic activity. After analyzing the particle size distribution in Fig 4.4, it is ascertained that the fraction of nanoparticles in the range between 10 and 15 nm can be conjugated with the photocatalytic activity (Fig. 4.16). The photocatalytic activity of TiO₂ particle is proportional to the number of the particles in the range between 10 nm and 15 nm. The tendency is not only suitable for the photocatalytic degradation of DCA, but also for the photocatalytic degradation of 4-CP. Moreover, for the reference material TiO₂ P25 this tendency is also suitable. It means that the particles between 10 nm and 15 nm are dominant particle size for the photocatalytic activity of TiO₂ particles, independent of particle synthesis method.

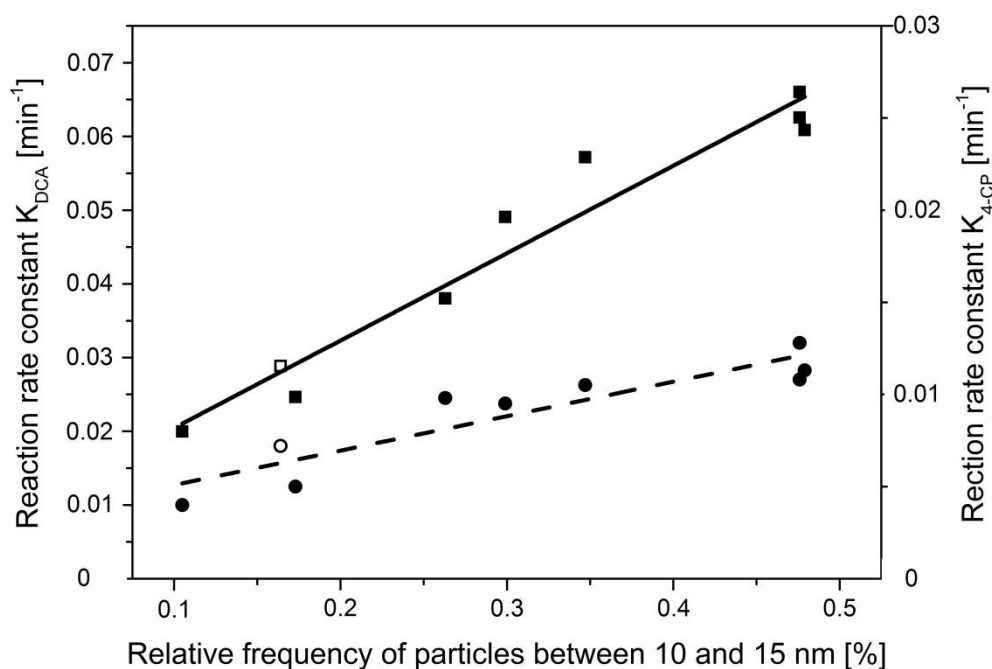


Fig. 4.16: Reaction rate constant k_{DCA} and k_{4-CP} as a function of relative frequency of particles between 10 nm and 15 nm (Solid points are the reaction rate constants of flame made samples and hollow points are for commercial reference material TiO₂ P25)

In fact, by flame synthesis the growth of particles is not uniform reflecting a certain polydispersity of TiO₂ particles (Fig. 4.4). Therefore, it is possible that the particle size distributions are different, although TiO₂ powders have the same average particle size. For example, the flame made sample S8 shows approximately the same average particle size of 20.56 nm in contrast to the reference material TiO₂ P25 of 21.36 nm. However, the particle size distributions of these two powders are different, as shown in Fig. 4. 17.

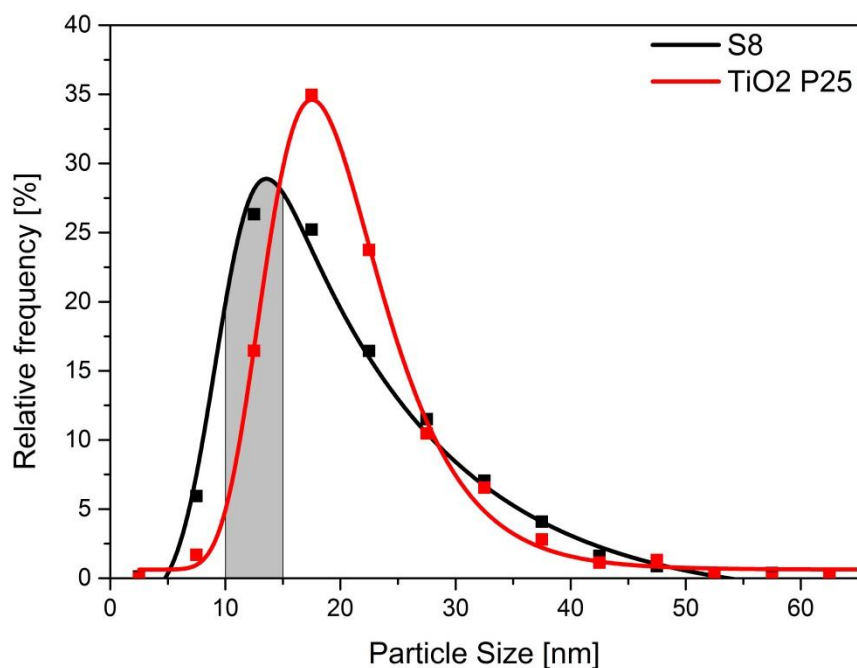


Fig. 4.17: Comparison of particle size distribution and area under 10nm to 15 nm of sample S8 and TiO₂ P25

The particle size distribution of sample S8 and TiO₂ P25 were obtained by plotting the bar diagram of Fig. 4.4. The particle size distribution of sample S8 is broader as TiO₂ P25 and the main fraction of particles are in the range between 10 nm and 20 nm. For TiO₂ P25, its particle size distribution is relative symmetric and main particles are in the range of 15-25 nm. Although sample S8 and TiO₂ P25 show approximately the same average particle size, sample S8 is more active than the reference material TiO₂ P25. It is found that for the particles between 10 and 15 nm of sample S8 and TiO₂ P25, sample S8 has larger areas under the curves noting larger number of particles than TiO₂ P25 (shown in Fig. 4.17), which results in higher photocatalytic activity. This result can explain the decrease of the photocatalytic activity with increased anatase mass fraction (Fig. 4.14) and TEM-equivalent particle size (Fig. 4.15).

However, the reaction rate constants of k_{DCA} and $k_{4\text{-CP}}$ are considered under the same mass concentration of TiO₂ photocatalyst. For the same mass concentration of photocatalyst, the TiO₂ powders show different specific surface area, as shown in Fig. 4.1. To emphasize real size effect beyond the specific surface area influence, the

reaction rate constants of k_{DCA} and $k_{4\text{-CP}}$ are normalized with total surface area of the particles, as depicted in Fig. 4.18.

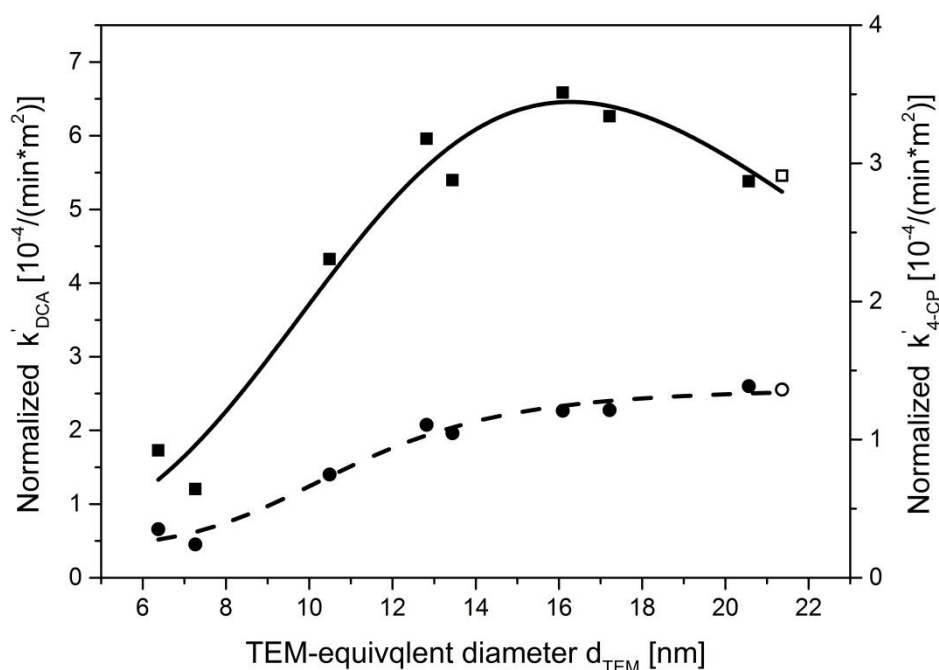


Fig. 4.18: Normalized reaction rate constants k'_{DCA} and $k'_{4\text{-CP}}$ as a function of average TEM-equivalent diameter of TiO₂ particles (Solid line is for the normalized reaction rate constants of DCA degradation and dashed line is for the 4-CP degradation; Solid points are the normalized reaction rate constants of flame made samples and hollow points are for commercial reference material TiO₂ P25)

For the interpretation of the results shown in Fig. 4.18, the whole chain of the reaction steps leading to the photocatalytic activity has to be considered, i.e. absorption of UV photons, generation of electron-hole pairs, migration to the particle surface and recombination. According to the studies of Müller et al. [101] and Born et al. [102], the adsorption of UV light of TiO₂ with the same mass is constant, as long as the band gap energy does not change (Fig. 4.19).

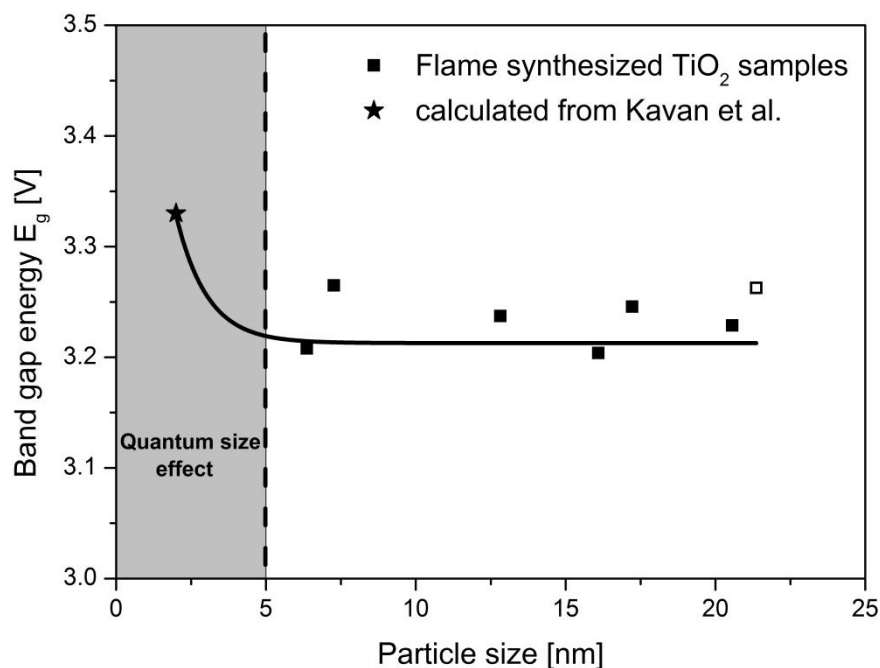


Fig. 4.19: The influence of particle size on the band gap energy of TiO₂ particles [103]
(Hollow point is the band gap energy of reference material TiO₂ P25)

As shown in Fig. 4.19, the band gap energy of flame synthesized TiO₂ is constant. When the TiO₂ particle size further decreases under about 5 nm, the band gap energy increases rapidly according to the studies of Kavan et al. [103]. From Fig. 4.19 it can be concluded that the formation of an electron-hole pair always needs the same minimal photon energy, independent of particle size. It means that for a given particle mass and a given irradiation intensity (and spectrum), the number of generated electron-hole pairs should be the same regardless of particle size. However, the migration of excited species to the particle surface and subsequent recombination may be influenced by the particle size. In fact, the results in Fig. 4.18 indicate that the size effect is present for both considered reactions, but with different characteristics. While in the case of DCA decomposition an optimum particle size appears at 16 nm, for the 4-CP degradation activity increases first with particle size and reaches a constant level at about 20 nm. However, for larger particles it is still possible that the activity decreases again. In the case of DCA decomposition the optimum particle size of 16 nm is different from the value of 14 nm determined in Fig. 4.15. The diameter of 16 nm is the optimal particle size for the generation, migration

and lifetime of reactive species produced by the UV irradiation, whereas the diameter of 14 nm is the optimal particle size for the overall photocatalytic activity when taking into account the inverse dependence of the available surface on particle size.

4.2 Binary TiO₂/SiO₂ nanoparticles

For the application of TiO₂ particles as self-cleaning coating on substrates produced by co-firing, the TiO₂ particles must be stable at high temperatures. Therefore, in this study the TiO₂ particles are coated with SiO₂ to improve their thermostability. Teleki et al. [29] have synthesized TiO₂ particles coated with SiO₂ in one step by flame spray pyrolysis for the application in sun cream. In that application, the TiO₂ particles used to absorb UV light must be hermetically coated with SiO₂ layers to avoid reaction with the skin by direct contact with the TiO₂ particles. In contrast, the stabilized TiO₂ particles in this work must exhibit high photocatalytic activity for degradation of organic pollutants in the application for self-cleaning coatings. Thus, the stabilized TiO₂ particles must have free surface after synthesis or heat treatment.

In this study SiO₂ was used as stabilizer for the TiO₂ particles, which were synthesized based on the condition for sample S6. The properties of sample S6 are summarized in Tab. 4.2. A core-shell structure of TiO₂/SiO₂ particles was desired to enhance the thermostability of anatase particles. According to the research of Shannon et al. [27], the onset of phase transformation of single anatase crystals occurred at about 900°C. By addition of SiO₂, the TiO₂ nanoparticles should be separated and the contact between anatase crystals should be avoided.

In this chapter, the stabilized samples were calcinated for 3 hours at 900 °C, 1000 °C, 1050 °C 1100 °C, 1150 °C and 1200 °C, respectively, in order to examine the thermostability and then the photocatalytic activity. Then, the effect of SiO₂ additive and calcination temperature on the physical and catalytic properties of TiO₂/SiO₂ is discussed. In addition, the effect of impurity ions of sodium, calcium and iron on the thermostability of TiO₂/SiO₂ particles is also discussed.

Tab. 4.2: Physical properties of non-stabilized sample S6

Sample	Ar/TiCl ₄	SSA	Anatase content	d _{TEM}
S6	26 l/h	86.57 m ² /g	91 wt.%	16.1 nm

4.2.1 Effect of additive and calcination on specific surface area

Tab. 4.3 shows the effect of SiO₂ additive and calcination on the specific surface area of flame synthesized samples, which are based on the synthesis condition of sample S6 with a specific surface area of ca. 87 m²/g. The non-calcinated samples show a specific surface area between 80 m²/g and 93 m²/g (Tab. 4.3), similar to sample S6. For the stabilization of TiO₂ particles, the precursor SiCl₄ was directly introduced into the flame, when the formation of TiO₂ particles was already completed. Thus, SiO₂ condensed on the surface of the TiO₂ particles and formed amorphous layers. Increasing the Si/Ti ratio causes a decrease of average density of TiO₂/SiO₂ particles. Additionally, the amorphous SiO₂ layer on the TiO₂ particles leads to an increase of the average particle size. Due to the two opposing parameters, the specific surface area is approximately constant for the non-calcinated samples. The slight increase of the specific surface area is due to the uniform distribution of the SiO₂ layers on the TiO₂ particles, in particular for a high Si/Ti ratio.

Tab. 4.3: Summary of the specific surface area of non-calcinated and calcinated TiO₂/SiO₂ particles

Sample	Si/Ti [mmol/mmol]	Specific surface area [m ² /g]			
		Non-calcinated	900 °C	1000 °C	1100 °C
P1	0.11	80.36	63.98	51.18	16.98
P2	0.22	79.98	74.31	72.51	33.37
P3	0.32	79.95	72.58	70.31	47.08
P5	0.64	87.80	72.63	66.44	40.06
P6	0.86	79.90	65.85	63.96	57.78
P7	1.71	82.34	67.9	64.56	51.09
P8	2.15	86.65	67.1	66.5	50.98
P10	6.44	93.52	55.63	56.62	44.25

For the calcinated samples, the specific surface area changes in the range between 55 m²/g and 75 m²/g, 51 m²/g and 70 m²/g as well as 17 m²/g and 57 m²/g for calcination temperatures of 900 °C, 1000 °C and 1100 °C, respectively. The specific surface areas of calcinated samples are generally smaller than the non-calcinated ones and decrease steadily with increased calcination temperatures, due to particle growth and restructuring of the agglomerates by the heat treatment. For each calcination temperature of 900 °C, 1000 °C and 1100 °C, the specific surface areas increase with increased Si/Ti ratio until a maximum and then decrease with further increased Si/Ti ratio. The increase is due to the protection of TiO₂ particles by the amorphous SiO₂ layer that suppresses particle growth, while the decrease is because of the restructuring of agglomerates. For the samples with low Si/Ti ratio (P1) calcinated at 1100 °C, its specific surface area decreased dramatically to about 17 m²/g indicating that the SiO₂ layer could not withstand the heat treatment. However, the flame made samples, in particular the samples P2 to P10, show still high specific surface area after calcination up to 1000 °C compared to the non-calcinated ones.

4.2.2 Effect of additive and calcination on phase composition

Fig. 4.20 shows the x-ray diffraction patterns of the stabilized samples P1 and P5 compared to the non-stabilized background sample S6 before heat treatment. The x-ray diffraction patterns of samples P1 and P5 are similar to that of sample S6. The anatase mass fraction of the samples P1 and P5 are 88 wt.% and 90 wt.%, respectively, which are similar to the anatase mass fraction of the sample S6 of 91 wt.%. The similar anatase mass fraction indicates that the SiO₂ additive has no influence on the phase composition of the flame made TiO₂ samples. The reason is that the SiCl₄ precursor was directly introduced into the reaction zone and the formation of TiO₂ particles was already completed before the SiO₂ condensation. Therefore, the phase composition of anatase depends only on the synthesis condition of TiO₂ particles. In addition, the samples P1 and P5 show approximately the same anatase fraction, although the sample P5 was synthesized with about six times the SiO₂ content as the sample P1. It shows that increasing the amount of SiO₂ additive has no influence on the phase composition of the flame made samples.

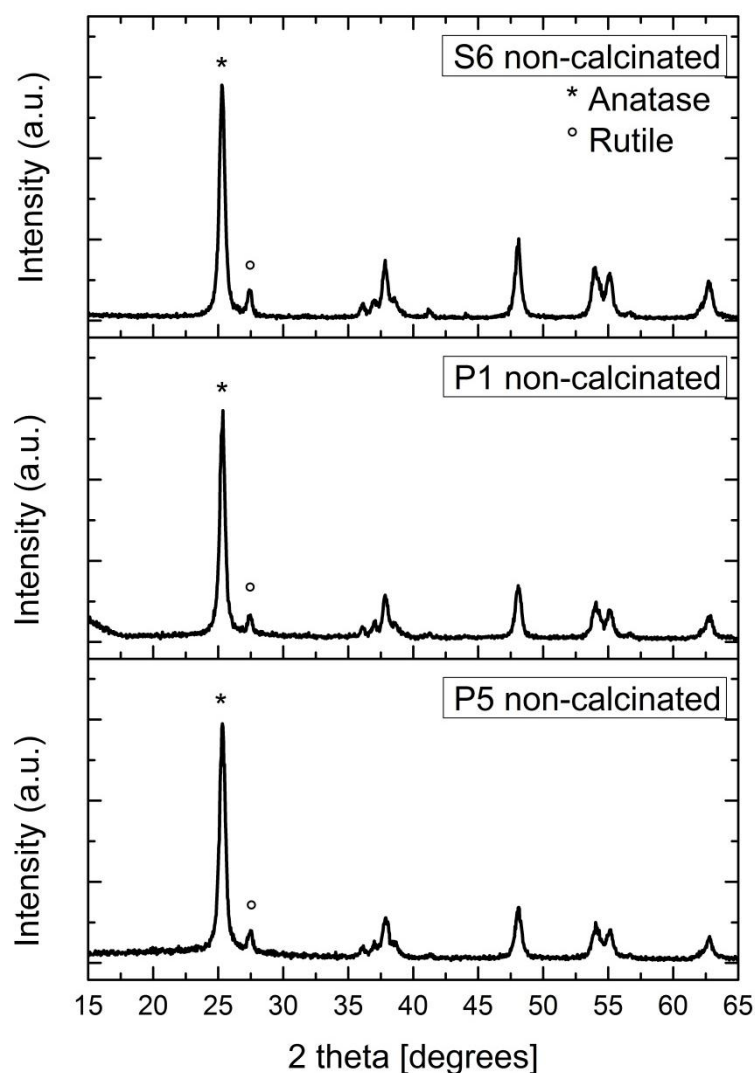


Fig. 4.20: X-ray diffraction patterns of the non-stabilized sample S6 and the stabilized non-calcinated samples P1 (Si/Ti ratio: 0.11) and P5 (Si/Ti ratio: 0.64) before calcination

It is well known that the transformation of anatase to rutile of non-stabilized TiO_2 particles begins at much lower temperature than 900 °C [21, 104]. To check this fact, the background sample S6 was calcinated at 900 °C for 3 hours and compared to the stabilized samples P2 after calcination at 900 °C and 1000 °C, respectively. As shown in Fig. 4.20, the non-calcinated sample S6 consists of ca. 91 wt.% anatase before calcination. After the heat treatment the anatase peaks of sample S6 disappear completely and the still present rutile peaks indicate that almost all anatase has transited to rutile at 900 °C (Fig. 4.21). Compared to the sample S6, the

stabilized sample P2 always shows high anatase peaks even after calcination at 1000 °C. This means that the presence of SiO₂ additive can effectively prohibit phase transformation from anatase to rutile at high temperatures.

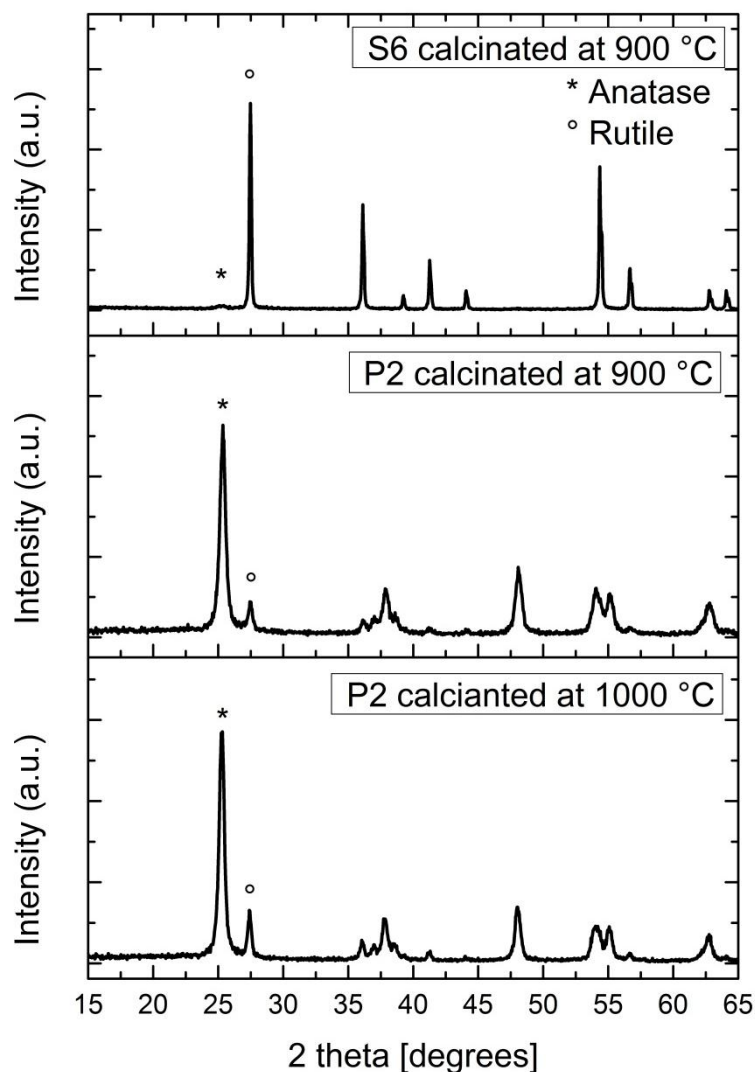


Fig. 4.21: X-ray diffraction patterns of the non-stabilized sample S6 (TiCl₄: 0.218 mmol/min) calcinated at 900 °C and the stabilized sample P2 (Si/Ti ratio: 0.22) calcinated at 900 °C and 1000 °C

Fig. 4.22 shows the effect of calcination temperature on the phase composition of sample P5. The non-calcinated sample P5 consists of about 90 wt.% anatase with a Si/Ti ratio of 0.64. After calcination at 900 °C to 1050 °C, the XRD patterns shows no significant differences in the broadness and height of anatase as well as rutile peaks,

which means that the anatase mass fraction and the size of anatase crystals are kept approximately constant. After calcination at up to 1050 °C the anatase mass fraction of sample P5 remains ca. 85 wt.% confirming the retarding effect of SiO_2 additive on the phase transformation. However, the XRD patterns of sample P5 calcinated at over 1100 °C show the phase transformation occurred above this temperature, because the rutile peaks have become much higher compared to the non-calcinated one and the anatase peaks have nearly disappeared after calcination at 1150 °C with an anatase mass fraction of ca. 10 wt.%. The results show that the presence of SiO_2 can effectively improve the thermostability of TiO_2 up to 1050 °C.

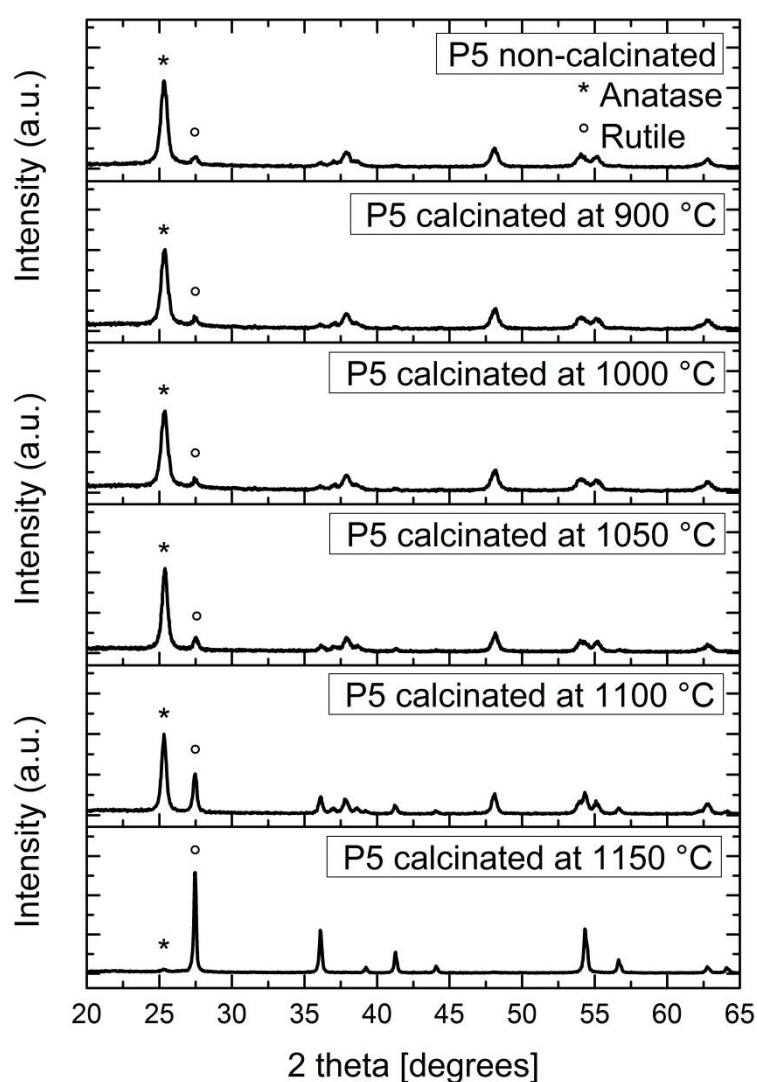


Fig. 4.22: X-ray diffraction patterns of the sample P5 (Si/Ti ratio: 0.64) non-calcinated and calcinated at 900 °C, 1000 °C, 1050 °C, 1100 °C and 1150 °C

Fig. 4.23 shows the anatase mass fraction of calcinated samples as a function of Si/Ti ratio. For each calcination temperature a maximal anatase mass fraction is observed, when the anatase particles were protected with a sufficient amount of SiO₂. In other words, in order to prohibit the phase transformation of TiO₂ particles at high temperatures a minimal amount of SiO₂ additive must be achieved. However, the maximal anatase mass fraction decreases with increasing calcination temperature. The reason is an inhomogeneous SiO₂ distribution on TiO₂ particles that leads to insufficient protection of a part of the anatase particles by heat treatment. The flame synthesized samples calcinated at 900 °C and 1000 °C show the same maximal anatase content, of about 87 wt.%. Until a calcination temperature of 1050 °C the samples exhibited a maximal anatase content of around 83 wt.%. This means that the SiO₂ additive has enhanced the thermostability of anatase particle to 1050 °C. When the calcination temperatures are higher than 1050 °C, the SiO₂ layers could not survive because of viscous flow occurring. Therefore, independently of the Si/Ti ratio the anatase mass fraction decreases to about 55 wt.% and 25 wt.% for the samples calcinated at 1150 °C and 1200 °C, respectively.

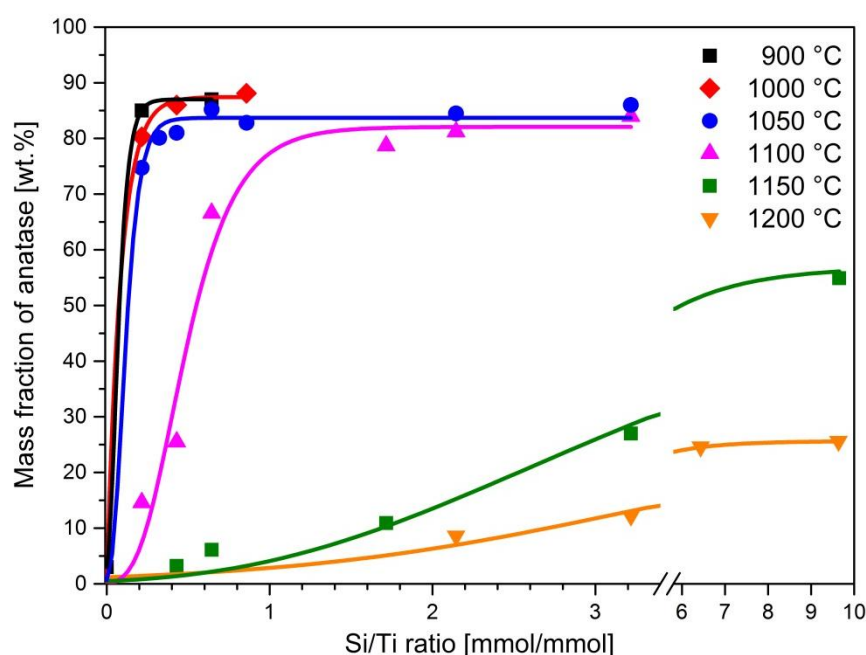


Fig. 4.23: The effect of Si/Ti ratio on the anatase content in the TiO₂/SiO₂ particles after calcination between 900 °C and 1200 °C

4.2.3 Effect of additive and calcination on particle morphology and size

According to the study of Shannon et al. [27], the location of SiO₂ in the necks between TiO₂ particles would be more favorable for the stabilization of anatase particles, because there would be still free surface for the photocatalytic reactions. However, these particles exhibited photocatalytic activity up to 900 °C only, which is not enough for the application as a co-firing self-cleaning coating. Therefore, a core-shell structure of TiO₂/SiO₂ particles is desired to enhance the thermostability of anatase particles and the surface of TiO₂ particles should be released after heat treatment. Fig. 4.24 illustrates the typical morphology of the TiO₂ nanoparticles with SiO₂ additive, which were synthesized in the premixed flame.

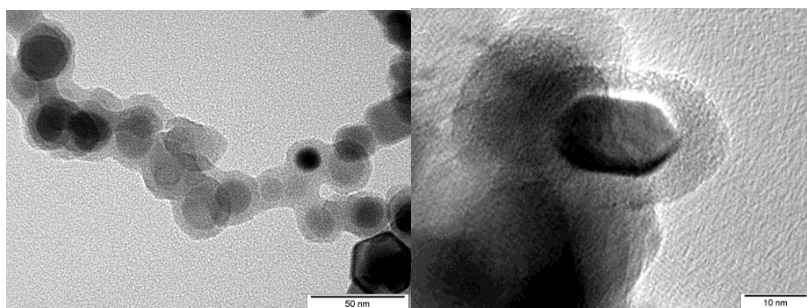


Fig. 4.24: Morphology of TiO₂/SiO₂ nanoparticles

The dark cores are TiO₂ particles because of high density and crystallinity, while the bright shells are SiO₂ layers condensed on the TiO₂ surface. From the TEM images, it can be seen that the TiO₂ particles are covered with a relative homogenous amorphous SiO₂ layer and are well separated from each other. Nevertheless, the SiO₂ additive hardly changed the chain-like structure of agglomerates and the faced structure of TiO₂ particle. This is attributed to the delayed introduction of the SiO₂ additive directly into the reaction zone after the formation of TiO₂ particles. The average particle size of TiO₂ cores was calculated from TEM images and is about 16.4 nm, which is similar to the average size of the background sample S6 of 16.06 nm. This proved again that the SiO₂ additive had no influence of the particle properties of TiO₂ particles. However, somehow the SiO₂ layer had to come inbetween two adhering TiO₂ particles to separate them. It should be noted here that the TiO₂ particles coated with a high SiO₂ content are more or less changed to

spherical morphology, as shown in Fig. 4.24. In addition, increasing the Si/Ti ratio from 0.11 to 9.65 mmol/mmol, increased the average thickness of SiO₂ layers from about 1.9 nm to over 10 nm.

Many approaches [12, 105-108] were developed to enhance the stability of TiO₂ without additive. The authors showed that the TiO₂ synthesized in the liquid phase was stable up to about 800 °C. Li et al. have synthesized crystal TiO₂ from layered titanates, which was stable up to 900 °C. Nevertheless, these TiO₂ particles are not suitable for the applications in ceramic processes because of the relative low thermostability. Therefore, many studies [37, 69, 70] were carried out to extend the thermostability of TiO₂ with SiO₂ additive. They showed increased thermostability of sol-gel synthesized mixed TiO₂/SiO₂ up to 1200 °C, but only for a short time of about 30 minutes. In order to check their thermostability, the flame made samples were calcinated at 900 °C, 1000°C, 1050 °C 1100 °C, 1150°C and 1200 °C for 3 hours, respectively. In our case it is expected that the TiO₂ particles coated with an amorphous SiO₂ layer should show high thermostability for a long time of 3 hours.

Fig. 4.25 shows the effect of calcination on the particle morphology and TiO₂ core size. After heat treatments no significant change of the particle morphology is observed, in contrast to the non-calcinated sample also shown in this figure. The average TiO₂ core size determined from TEM images is kept approximately constant by about 17 nm up to 1050 °C. When the calcination temperature is above 1050 °C, the SiO₂ layers on the TiO₂ particles were destroyed (Fig. 4.26) and simultaneously the anatase particles transited to bigger rutile particles. Therefore, the average size of TiO₂ core increases dramatically to over 50 nm after calcination exceeded 1100 °C. The results are in agreement with the observation of the phase composition and proved again that the thermostability of TiO₂ was enhanced up to 1050 °C.

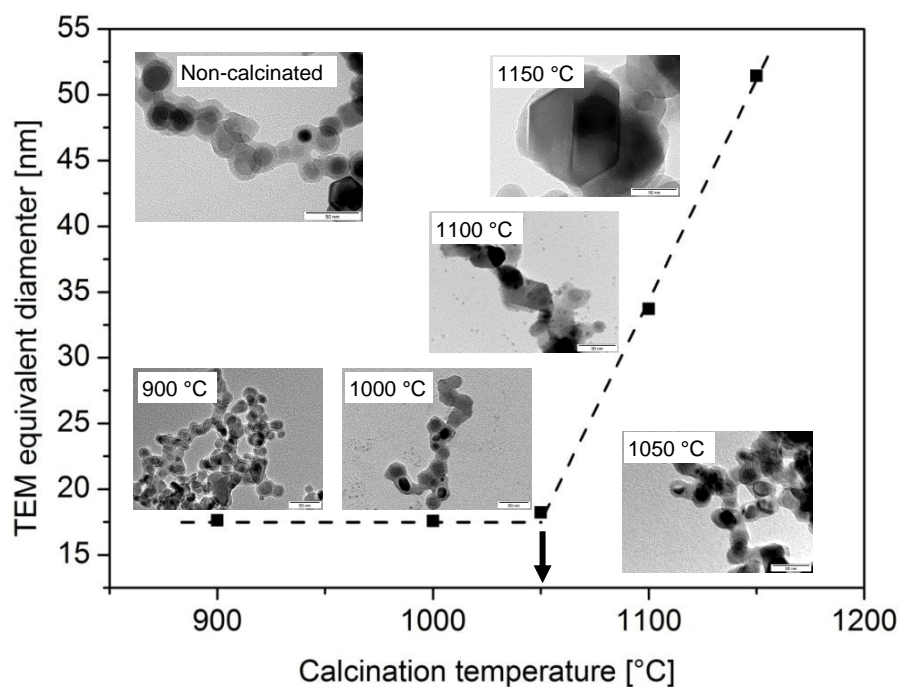


Fig. 4.25: The effect of calcination on the particle morphology and the average TiO₂ core size

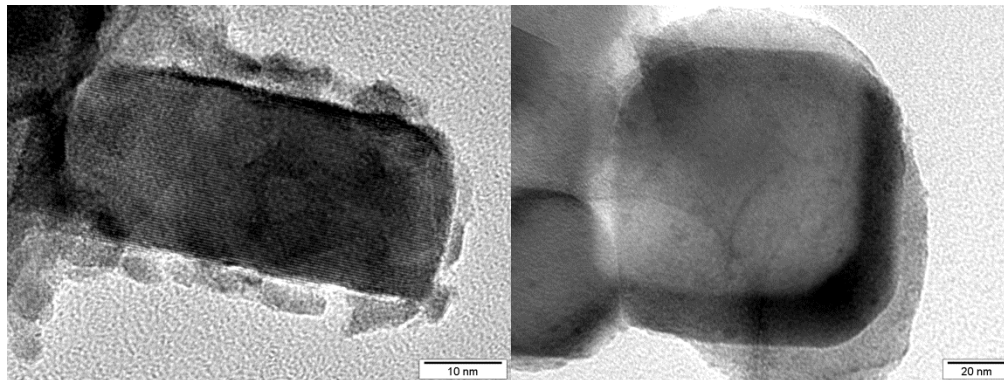


Fig. 4.26: Change of the SiO₂ layer after calcination at 1100 °C (left) and 1150 °C (right)

4.2.4 Effect of additive and calcination on photocatalytic performance

The photocatalytic performance of calcinated TiO₂/SiO₂ particles was tested for the decomposition of DCA under UV-A light in the liquid phase at ambient temperature. Fig. 4.27 illustrates the photocatalytic degradation of DCA for the sample P5 with a Ti/Si ratio of 0.64 before and after calcination at different temperatures.

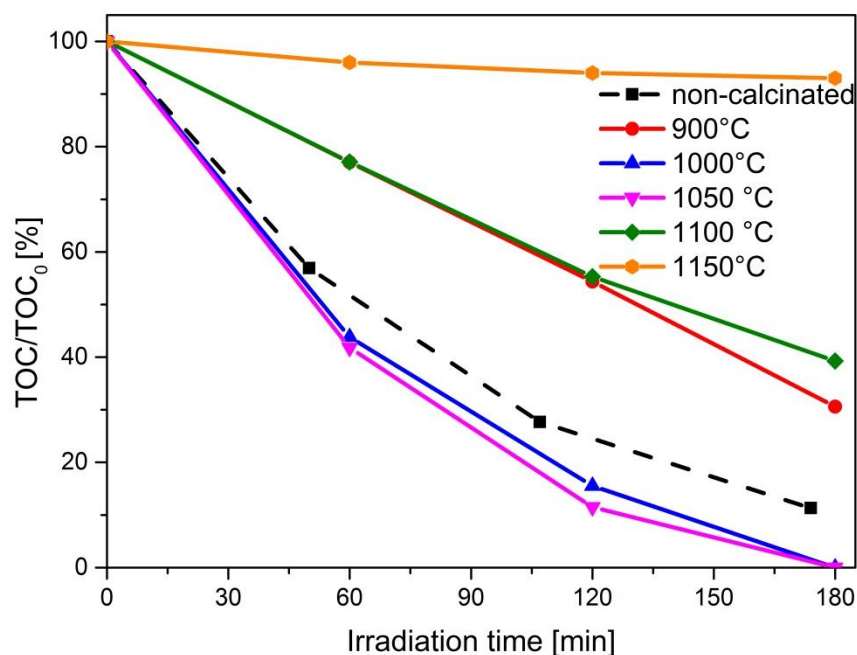


Fig. 4.27: Photocatalytic degradations of DCA with calcinated sample P5 (Si/Ti ratio: 0.64)

For the non-calcinated sample P5, about 90 % DCA is decomposed in 180 minutes (dashed line). Its photocatalytic activity is much lower with higher photocatalyst loading of 0.5 g/l than that of the background sample S6 degrading about 90 % DCA in 40 minutes with photocatalyst loading of 0.3 g/l. The non-calcinated particles showed certain photocatalytic activity for the DCA degradation because of the inhomogeneous distribution of SiO₂ on the TiO₂ particles, i.e. certain uncovered titania surface. Lindner et al. [93] and Bahnemann et al. [94] have pointed out that the photocatalytic decomposition of DCA could take place, only when the DCA molecules are in close contact with TiO₂ surface. In addition, SiO₂ is photocatalytically inactive indicating that some TiO₂ particles are not coated with SiO₂ and have free surface for the photocatalytic reaction. When the TiO₂ particles are hermetic or completely covered with a SiO₂ layer, they should not have any activity when exposed to UV light, because the TiO₂ particles have no direct contact with the DCA molecules. However, the part of non-coated TiO₂ particles in the form of anatase could not survive after calcination at or above 900°C, according to the studies [21, 104]. Despite the loss of part of the anatase, the sample P5 shows obvious activity for the degradation of DCA after calcination. The highest DCA

decomposition with P5 appears after the calcination at 1000 °C and 1050 °C. The sample shows similar photocatalytic ability after calcination at 900 °C and 1100 °C, respectively. The sample P5 is almost inactive after calcination at 1150 °C. From 900 °C to 1050 °C the photocatalytic activity increased with increased calcination temperature. It is assumed that more surface of anatase particle was released with increasing calcination temperature, because until 1050 °C the sample S6 shows almost the same anatase fraction of 85 wt.%. When the calcination temperature increases further to more than 1050 °C, the SiO₂ protection layers were destroyed after heat treatment and the photocatalytic activity decreases dramatically due to the decreased anatase mass fraction (Fig. 4.23).

Fig. 4.28 shows the DCA oxidation rate at 120 minute with flame made samples (P1-P9) calcinated at various temperatures as a function of Si/Ti ratio.

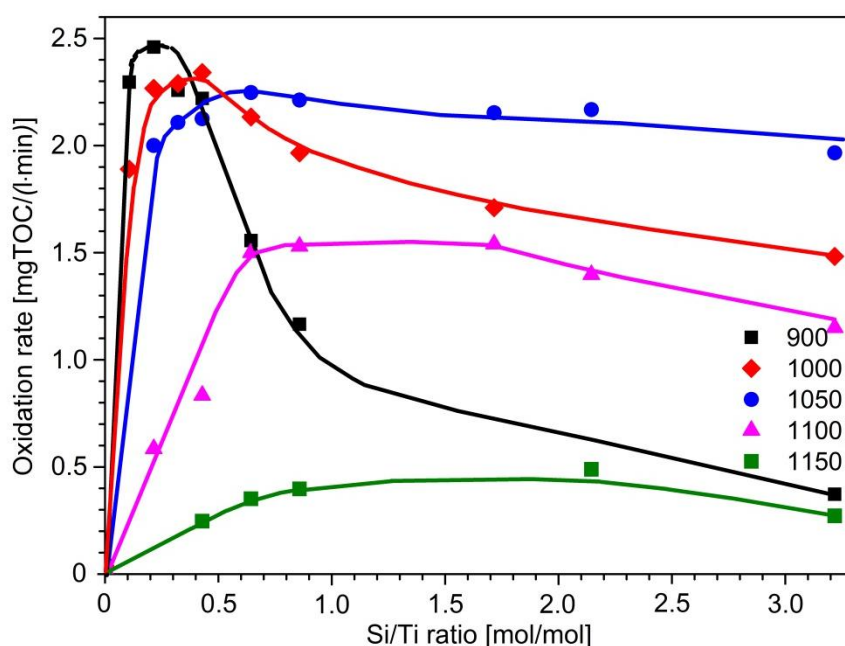


Fig. 4.28: Photocatalytic oxidation rate of DCA with calcinated samples as a function of Si/Ti ratio

From this diagram it can be seen that the presence of SiO₂ obviously improved the thermostability of TiO₂ particles and the SiO₂ coated TiO₂ particles exhibited high photocatalytic activity after calcination. For each calcination temperature, the DCA oxidation rate increases with increasing Si/Ti ratio until a maximal value and then

decreases with further increasing Si/Ti ratio. The increase of DCA oxidation rate is because of the increase of anatase mass fraction of the samples after calcination attributed to the increased SiO₂ protection. The later decrease of DCA oxidation rate is due to an excessive amount of SiO₂ on the TiO₂ particles. The amorphous SiO₂ layer on TiO₂ particle reduced the PCA for non-calcinated samples and also for the calcinated samples with excessive SiO₂ content [25]. The most active sample is calcinated at 900 °C with low silica content and the maximal PCA of every calcination temperature decreases with increased calcination temperature due to the decrease of anatase content, as shown in Fig. 4.23.

4.2.5 Effect of impurity ions on thermostability

In the present study the stabilized TiO₂ particles are desired to coat roof tiles in order to obtain a self-cleaning surface. According to the study of Hornfeck [109], some ions such as Zr⁴⁺ and Al³⁺ can affect the viscosity of SiO₂ by the synthesis of quartz glass. Because there may be many impurity elements on the surface of roof tiles made of such as Kaolin, the influence of impurity ions of sodium, calcium and iron on the thermostability of the TiO₂/SiO₂ particles (sample P4, Si/Ti ratio: 0.43) was investigated. For the investigations the sample P4 was mixed with different concentrations of impurity ions. The concentrations of impurity ions of sodium, calcium and iron varied from 0.0005 mol/mol to 1 mol/mol, compared to the number of titanium atoms. After mixing, the powders were calcinated at 950 °C for 3 hours and the phase composition was determined with XRD as analogous to evaluation of the thermostability of TiO₂/SiO₂ particles from the XRD analysis.

For sodium ions, the TiO₂/SiO₂ particles were completely destroyed and coalesced with the quartz cup used in the calcination procedure. Therefore, the phase composition of the sample P4 was not measureable.

Fig. 4.29 shows the influence of calcium ions on the phase composition of TiO₂/SiO₂ particles. For the addition of calcium ions calciumacetathydrat was used as raw material and added into the TiO₂/SiO₂ powder prior to calcination at 950 °C for 3 hours.

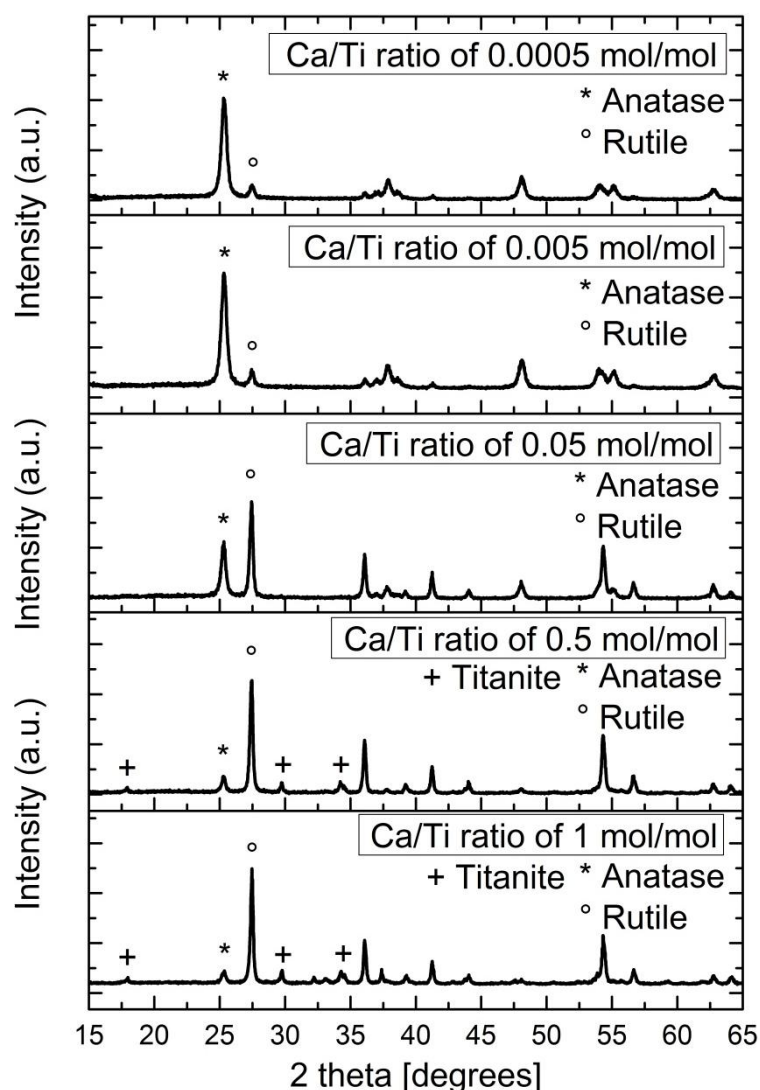


Fig. 4.29: Influence of calcium ions on the phase composition of $\text{TiO}_2/\text{SiO}_2$ particles calcinated at 950°C for 3 hours

At low concentrations of the Ca/Ti ratio up to 0.005 mol/mol, no change in the phase composition is observed in the XRD patterns. The rutile mass fraction is kept constant at around 13 wt.%. Nevertheless, a further increase of calcium ion concentration to 0.05 mol/mol leads to a significant increase of rutile mass fraction to 63%. No additional peaks appeared in the XRD patterns meaning that no other phase was formed by addition of calcium ions at low concentration up to 0.05 mol/mol. However, when the Ca/Ti ratio further increases to over 0.5 mol/mol, some additional peaks are observed in the XRD patterns. The additional peaks appear at 17.9° , 29.7° and 34.2° , which correspond to the mineral titanite with the chemical

formula of CaTiSiO_5 . The rutile mass fraction increases to 71 wt.% with a Ca/Ti ratio of 0.5 mol/mol, whereas the anatase mass fraction is only 7.1 wt.%. Moreover, a small amount of perovskite (CaTiO_3), portlandit ($\text{Ca}(\text{OH})_2$) and Limestone (CaO) are found by analyzing of the XRD patterns, when the Ca/Ti ratio is above 0.5 mol/mol. The results indicate obviously that the calcium additive leads to a reduction of the thermostability of $\text{TiO}_2/\text{SiO}_2$ particles. The formation of titanite is a sign that due to the reaction of $\text{TiO}_2/\text{SiO}_2$ particles with calcit formed during the decomposition of calciumacetathydrat, the SiO_2 layer is corroded by the calcium ions. After erosion of the SiO_2 layer, the calcit reacts further with the TiO_2 core, so that the phase transformation is started at 950 °C.

To investigate the influence of iron ions on the thermostability of $\text{TiO}_2/\text{SiO}_2$ particles, the sample P4 was mixed with iron(III) citrate and then calcinated at 950 °C for 3 hours. Fig. 3.30 shows the influence of iron ions on the phase composition of $\text{TiO}_2/\text{SiO}_2$ particles.

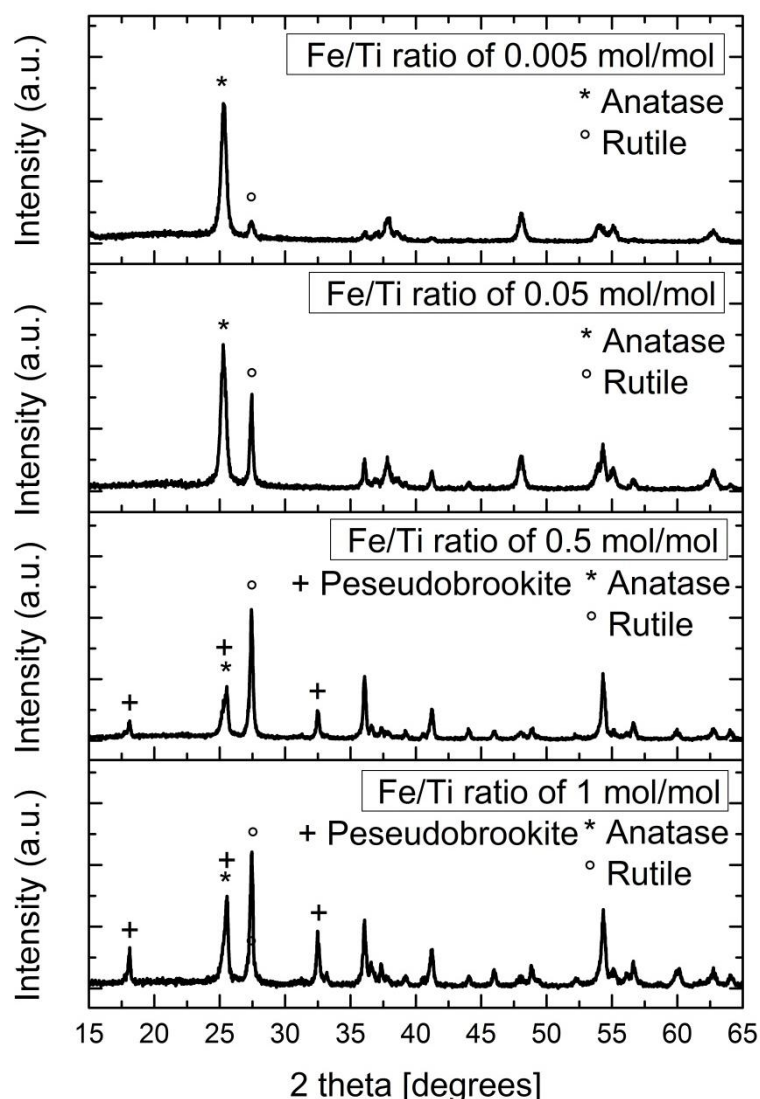


Fig. 4.30: Influence of iron ion on the phase composition of $\text{TiO}_2/\text{SiO}_2$ particles calcinated at 950 °C for 3 hours

For low Fe/Ti ratios up to 0.005 mol/mol, no influence of the iron ions on the phase composition is observed in the XRD patterns. The rutile mass fraction remains unchanged at about 13 wt.% compared to the sample P4. Increasing the Fe/Ti ratio to 0.05 mol/mol causes a significant increase of the rutile peak. With further increased Fe/Ti ratio, additional peaks appear in the XRD patterns at 18.1 ° and 32.5 °, which can be assigned to the bond between iron and titanium. At a Fe/Ti ratio of 1 mol/mol, another additional peak of Fe_2O_3 is observed. For a high concentration of iron ions with 0.5 mol/mol and 1 mol/mol, the rutile mass fractions are much higher and increase steadily, in contrast to a low Fe/Ti ratio of 0.005 mol/mol. It must be

noted that for the high concentration of iron additive, the rutile mass fraction cannot be evaluated accurately because of an overlap of the pseudobrookite peak with the main anatase peak.

However, the change of the phase composition cannot clearly identify the addition of iron ions as the cause for the reduced thermostability of TiO₂/SiO₂. The formation of pseudobrookite only shows that the iron ions can react with TiO₂ particles. It is known that the doping of TiO₂ particles with iron causes an increase of rutile mass fraction because of diffusion of iron ions in the TiO₂ lattice [110, 111]. Nevertheless, no bonds between iron and silicon are observed. Therefore, there is no direct evidence that the iron ion can reduce the thermostability of TiO₂/SiO₂ particles.

4.2.6 Discussion

In the present study the thermostability of TiO₂ particles was enhanced by a SiO₂ additive up to 1050 °C for 3 h, in order to make the stabilized particles suitable for the production of co-fired self-cleaning surfaces on ceramic roof tiles. Periyat et al. [69] and He et al. [70] have reported that thermostability of TiO₂ particles are improved up to 1000 °C by an SiO₂ additive of 15 mol% in the liquid phase. Tobaldi et al. [25] and Cho et al. [112] have investigated the effect of SiO₂ additive on the TiO₂ particle properties. They found that the SiO₂ additive can suppress the phase transformation of anatase at high temperatures and the TiO₂/SiO₂ particles exhibit high photocatalytic activity. They have also found that for the SiO₂ additive in the TiO₂ lattices a part of Ti⁴⁺ ions are substituted by Si⁴⁺ ions to form Ti-O-Si bonds, which contribute to the improved thermostability of TiO₂ particles. The studies of Hung et al. have investigated the structure of the mixed oxide TiO₂/SiO₂ in a counterflow diffusion flame reactor with various SiO₂ concentrations and flame temperatures. They showed that a high flame temperature is favored to form discrete SiO₂ particles on TiO₂ particles while at low temperature the formation of a smooth SiO₂ layer on TiO₂ particles is favored. Furthermore, at low SiO₂ concentration TiO₂ particles are covered with discrete SiO₂, whereas at high SiO₂ concentration TiO₂ particles are encapsulated with SiO₂ layers. Ehrmann et al. [113] have simulated the possible formation of TiO₂/SiO₂ particles in a premixed flame. They have pointed out the

structure of TiO₂/SiO₂ particles is dependent on the miscibility of the TiO₂ and SiO₂ particles.

In this work, the enhancement of the thermostability of TiO₂ particles is due to the amorphous SiO₂ layers condensed on the TiO₂ surface, as shown in the TEM images in Fig. 4.24. This is due to the low flame temperature in this study, of about only 1000°C and the relatively high precursor feed rate. Therefore, the SiO₂ formed a smoother layer on the TiO₂ surface. However, the thickness of SiO₂ layer is not uniform, which is analogous to the study of Hu et al. [32]. Moreover, the morphology of the SiO₂ layers (thickness, homogeneity and structure) has a decisive influence on the thermostability and photocatalytic activity of TiO₂ particles. A thick SiO₂ layer reduces the photocatalytic activity of TiO₂ photocatalyst by a barrier effect, whereas a thin SiO₂ layers cannot sufficiently prohibit the phase transformation of TiO₂ by heat treatment. However, due to the limitations of the experimental conditions SiO₂ is inhomogeneously distributed on the TiO₂ surface, as shown in Fig. 4.31. As the thickness of the SiO₂ layer increases caused by increased precursor feed rate, the average thickness of the SiO₂ layer also increases and its size distribution becomes broader simultaneously.

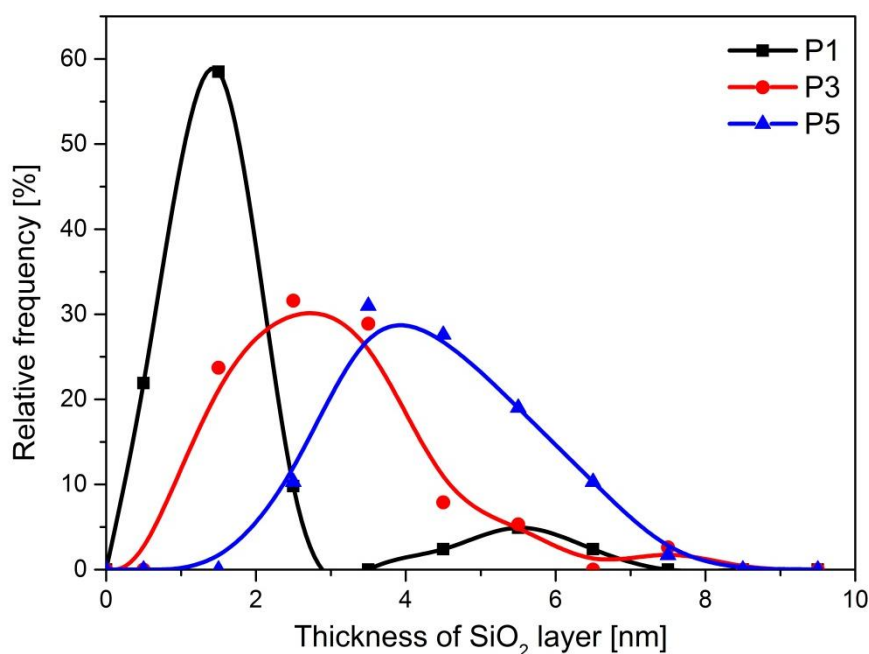


Fig. 4.31: Size distribution of SiO₂ layer thickness of sample P1 (Si/Ti ratio: 0.11), P3 (Si/Ti ratio: 0.32) and P5 (Si/Ti ratio: 0.64)

From Fig. 4.31 it can be seen that the SiO_2 layer is not homogeneously distributed on the TiO_2 surface. The size distribution of SiO_2 layer is relatively wide and dependent on the precursor feed rate of SiCl_4 . With increasing precursor feed rate the size distribution of SiO_2 layer becomes broader and is shifted to bigger size. However, the increase of the thickness of SiO_2 layer is not proportional to the increase of the SiO_2 additive amount. The reason is that the mixing between TiO_2 and SiO_2 is not homogeneous causing inhomogeneous SiO_2 layers on the TiO_2 surface. For sample P1 the average thickness of SiO_2 layer is about 2 nm at Si/Ti ratio of 0.11. For sample P5 with three times the amount of SiO_2 added compared to P1, the average layer thickness is about 4 nm. The large width of the size distribution of SiO_2 layer is due to the method of the SiCl_4 precursor addition by means of a quartz tube. Therefore, there is only a part of SiO_2 layers effective for stabilization of TiO_2 particles. The results can be supported with the photocatalytic test with non-calcinated samples, as shown in Fig. 4.32.

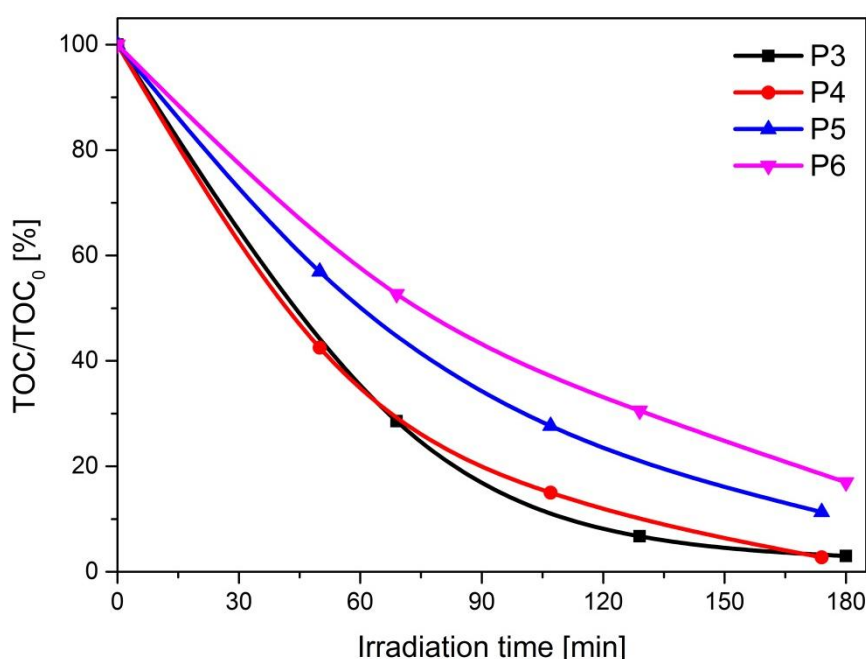


Fig. 4.32: Photocatalytic degradation of DCA with non-calcinated samples P3 (Si/Ti ratio: 0.32), P4 (Si/Ti ratio: 0.43), P5 (Si/Ti ratio: 0.64) and P6 (Si/Ti ratio: 0.86)

The non-calcinated TiO₂/SiO₂ samples P3 to P6 show high photocatalytic activity for DCA degradation. The sample P3 with the lowest amount of SiO₂ additive exhibits the highest photocatalytic ability and an increase of the SiO₂ amount leads to a steady decrease of the photocatalytic activity of the samples. The results demonstrate again that a part of the TiO₂ particles is not coated with SiO₂ layers and still has free surface for the DCA degradation that decreases with increased SiO₂ amount. However, the non-coated TiO₂ particles could not survive the heat treatment above 900 °C. This is also the reason for the lower photocatalytic activity of TiO₂/SiO₂ particles after calcination compared to the non-stabilized TiO₂ particles.

In this study the SiO₂ layers play an important role for the stabilization of TiO₂ particles during heat treatment. The amorphous SiO₂ layer can not only stabilize the TiO₂ particles, but also hinders the direct contact of organic molecules and TiO₂ particles. The stabilized TiO₂ particles show high photocatalytic activity after calcination above 900 °C demonstrating that the surface of TiO₂ is released after heat treatment. To examine the structural change of the SiO₂ layer by heat treatment, the sample P3 was heated and observed online in TEM. Because of the limitations of the TEM equipment the sample could only be heated up to 800 °C. The TEM images of the sample heated at 800 °C are shown in Fig. 4.33. An agglomerate of TiO₂ with primary particle size between 10 to 40 nm is illustrated in the figure a). The TiO₂ particles are coated with SiO₂ layers of different thickness between 2 nm to 10 nm and the average thickness of the SiO₂ layer is about 4 nm. The initial agglomerate size is shown in this figure and is 112.2 nm. After heat treatment at 800 °C for 3 hours, the particle shows a small but still significant change of the agglomerate size from 112.2 nm to 108.1 nm (Fig. 4.33, b). With further heating for 4 hours the agglomerate is shortened by more than 10 nm to 102.0 nm (Fig. 4.33, c). While during the heating process no change of the TiO₂ cores is observed, the thickness of the SiO₂ layer changes slightly. As the SiO₂ layers are thinner than 1 nm, the change is not visible on the TEM-images, whereas the SiO₂ bridge between two TiO₂ particles changes significantly, which is marked with a red circle in the figure. Therefore, it is assumed that the reduction of the thickness of the SiO₂ layer could be the reason for the recovery of the photocatalytic activity of the TiO₂/SiO₂ particle after calcination.

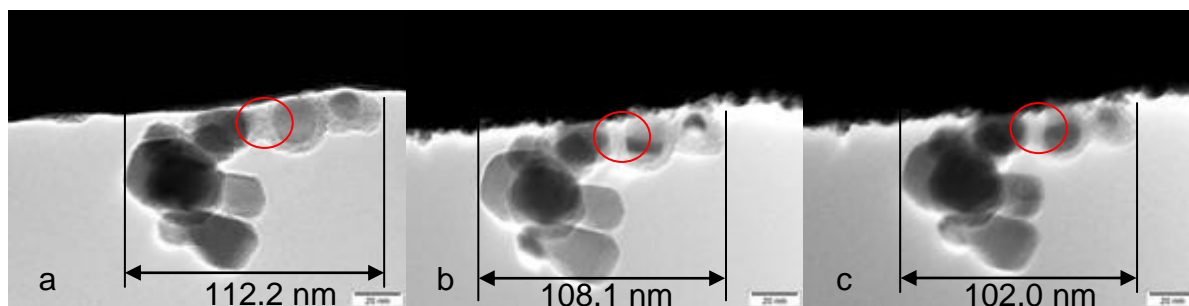


Fig. 4.33: Observation of the change of SiO_2 layer with online heating: a) at room temperature; b) 800°C , 3 h; c) 800°C , 4 h

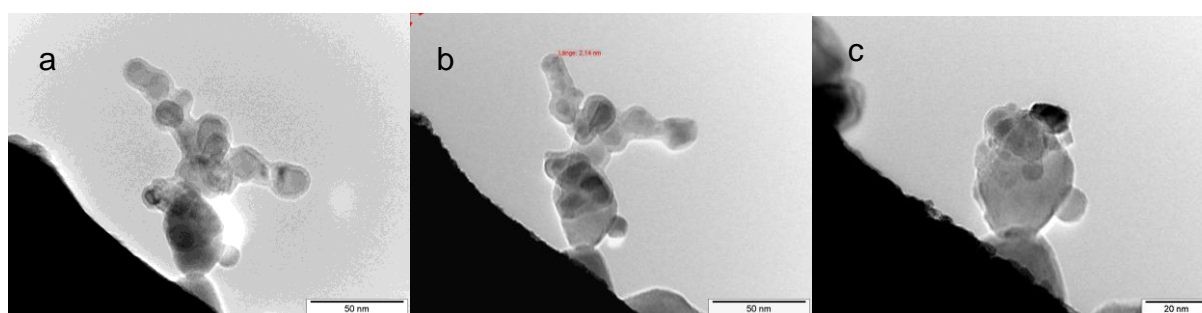


Fig. 4.34: Observation of the change of $\text{TiO}_2/\text{SiO}_2$ structure with online heating: a) at room temperature; b) 800°C , 3 h; c) 800°C , 4 h

Fig. 4.34 shows another set of TEM images of a $\text{TiO}_2/\text{SiO}_2$ agglomerate, which is online heated at 800°C for 3 h and 4 h, respectively, and additionally compared to a non-calcinated one. The non-calcinated sample shows the typical chain-like structure of flame made $\text{TiO}_2/\text{SiO}_2$ particles with homogenous SiO_2 layers. After calcination at 800°C for 3 hours, the agglomerate shows a tendency of contraction of the particles and after 4 hours the chain-like structure collapses and forms a compact and dense agglomerate. The restructuring of the agglomerate results in a decrease in the specific surface area of the stabilized TiO_2 particles after calcination, which is in agreement with the observation in the BET analysis. The change of the $\text{TiO}_2/\text{SiO}_2$ agglomerate structure indicates that the SiO_2 can flow because of its low viscosity at high temperature [114]. It supports the assumption of the release of TiO_2 surface by viscous flow of SiO_2 during the heat treatment.

5 Performance of self-cleaning coatings made of TiO₂/SiO₂ nanoparticles

In recent years, TiO₂ coatings have attracted much attention as self-cleaning surfaces, because the surface cleaning of buildings requires a high energy consumption and use of chemical detergents and consequently generates high costs. The initial goal of this study is the production of self-cleaning coatings on roof tiles in a one-step procedure without loss of photocatalytic activity during baking. To realize this goal, the flame synthesized TiO₂/SiO₂ particles showing high thermostability were deposited on substrates and baked at various temperatures. Although the results in the previous chapter showed that the flame synthesized TiO₂/SiO₂ particles are stable up to 1050 °C, some impurities on the substrate caused a reduction of the thermostability of TiO₂/SiO₂ particles. Therefore, in order to study the coating process and the performance of the coating itself, the influence of impurities was masked by using Si-wafers (Siltronic AG) as model substrate for the coating process with TiO₂/SiO₂ particles.

5.1 Self-cleaning coating of extended surface with TiO₂ photocatalyst

To achieve high temperature stable self-cleaning coatings, spray coating method was applied with the reference material TiO₂ P25 and flame synthesized TiO₂/SiO₂ particles of sample P4. The powders were firstly dispersed in distilled water at a concentration of 10 g/l. The pH value of the suspension was adjusted to 3 with HNO₃ and then treated in an ultrasonic bath for 30 minutes. Using spray coating method the TiO₂ photocatalyst was deposited on the Si-wafers with 30-40 spraying cycles, which corresponded to a TiO₂ loading of 38.4 g/m² on the substrate surface. During the coating process the Si-wafers were heated at 150 °C for a simultaneous drying.

5.2 Baking of coatings

According to the industrial manufacturing of roof tiles, the Si-wafers with TiO₂ coatings were baked at different temperatures between 150 °C and 1050 °C. The

baking process is similar to the calcination process of the $\text{TiO}_2/\text{SiO}_2$ particles in the previous sections. The coatings were baked in a muffle furnace with a heating rate of 5 K/min for 3 hours to the desired temperature. When the coating process was finished, the furnace cooled down to room temperature. The total duration of the baking process was about 24 hours. Due to the low thermostability of TiO_2 P25, the coatings with TiO_2 P25 were baked up to 750 °C, while the $\text{TiO}_2/\text{SiO}_2$ coatings were baked up to 1050 °C.

5.3 Photocatalytic test of coating

The photocatalytic activity of the coatings was tested for the degradation of the model organic substance DCA under UV-A light irradiation (Cleo Performance 40-W-R, Philips) with an intensity of 60 W/m^2 to 65 W/m^2 . The reactor for the determination of the photocatalytic activity of the coating is shown in Fig. 5.1.

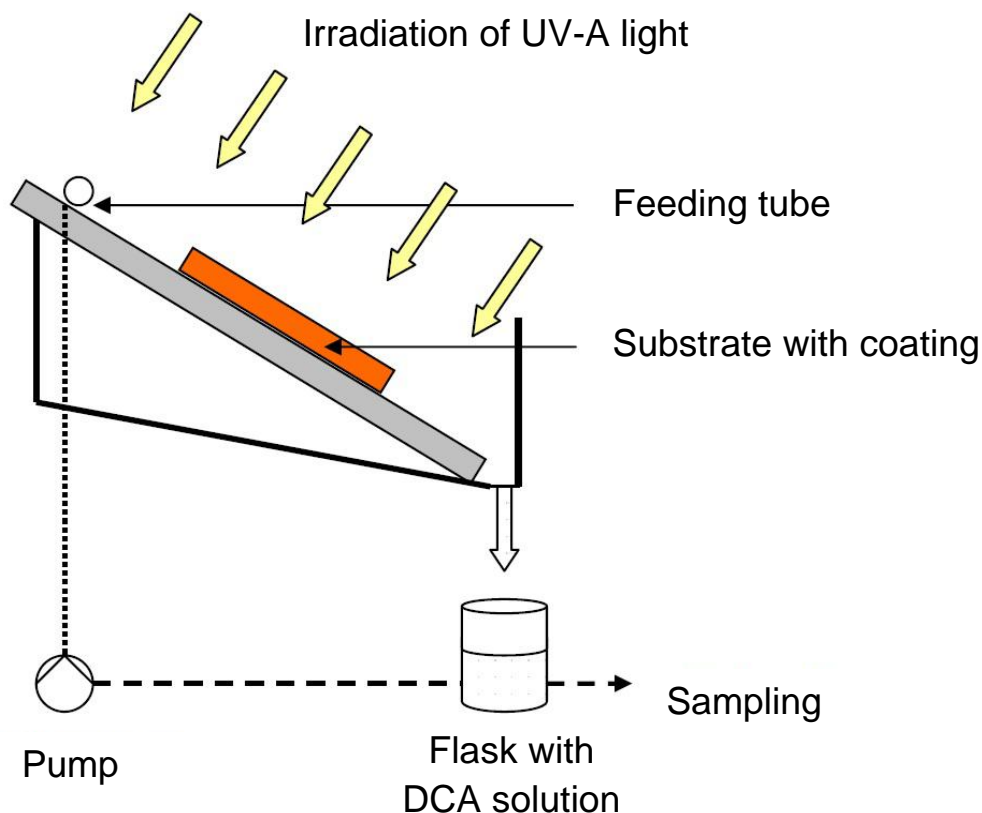


Fig. 5.1: Apparatus for photocatalytic test of coatings

For the photocatalytic test the DCA solution is continuously fed onto the coating with a pump. During the photocatalytic degradation of DCA about 5 ml solution was withdrawn from the reactor every 30 minutes. By measuring the TOC remained in the solution with TOC-analyzer, the photocatalytic performance of coating was quantified.

5.4 Results

5.4.1 Structure of coating

The self-cleaning effect of the TiO_2 coating is based on the combination of the photocatalytic and superhydrophilic properties. Adsorbed organic pollutants on the self-cleaning surface can be decomposed under UV irradiation due to the photocatalytic properties of TiO_2 , whereas the contaminant and dust can be washed off by rainwater because of superhydrophilic properties of TiO_2 . Fig. 5.2 shows the morphology of the self-cleaning coating with $\text{TiO}_2/\text{SiO}_2$ particles (sample P4) on Si-wafer before baking.

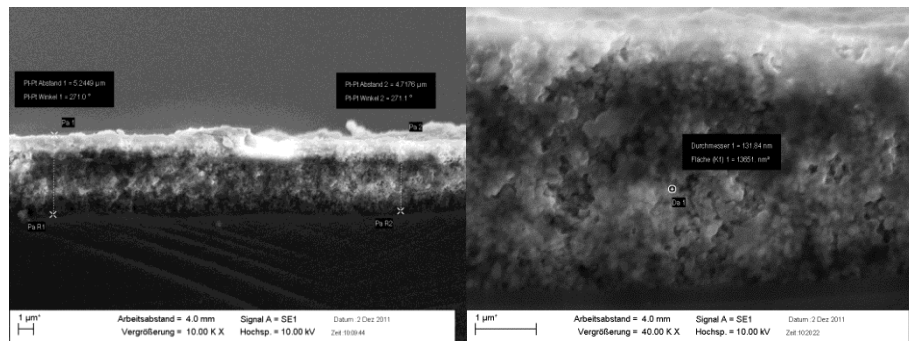


Fig. 5.2: SEM-image of the morphology of $\text{TiO}_2/\text{SiO}_2$ coating before baking

As shown in Fig. 5.2, the self-cleaning coating shows high optical quality and its thickness is relative homogeneous at about 5 μm (left). The coating has a porous structure and consists of small $\text{TiO}_2/\text{SiO}_2$ agglomerates of about 130 nm (right).

Fig. 5.3 shows the surface roughness of the coatings with TiO_2 P25 and $\text{TiO}_2/\text{SiO}_2$ particles as a function of baking temperature. The baked coatings with $\text{TiO}_2/\text{SiO}_2$ particles show lower roughness between 0.4 and 0.5 μm than the coating with TiO_2

P25 indicating that the surface of $\text{TiO}_2/\text{SiO}_2$ is much smoother. The roughness of the TiO_2 P25 coating is higher as $1.3 \mu\text{m}$, even after baking at 400°C . After baking above 500°C the roughness decreases rapidly to $0.6 \mu\text{m}$. However, the roughness of the $\text{TiO}_2/\text{SiO}_2$ coating has not changed significantly with increasing baking temperature. The change of the roughness of the TiO_2 P25 coating indicates the particle growth during baking and the unchanged roughness of the $\text{TiO}_2/\text{SiO}_2$ coating is because of high thermostability of $\text{TiO}_2/\text{SiO}_2$ particles.

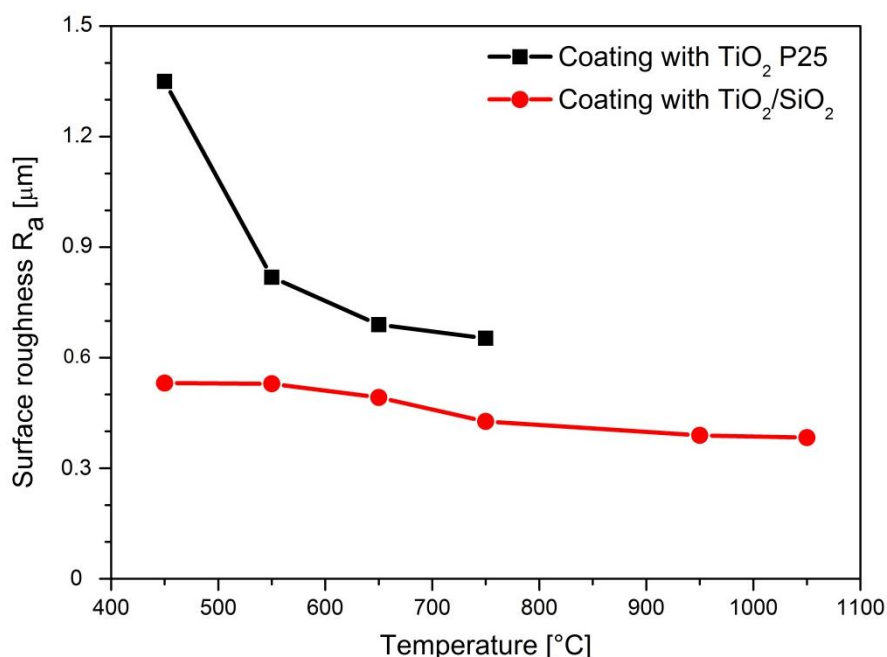


Fig. 5.3: Roughness of the coating surface as a function of baking temperature

5.4.2 Phase composition of baked coatings

The sample P4 showed thermostability up to 1050°C described in the previous chapter. To check whether the thermostability of TiO_2 P25 and $\text{TiO}_2/\text{SiO}_2$ particles is affected by coating process or substrate, the phase composition of the particles scratched from the Si-wafers after baking was measured with XRD. The XRD patterns of TiO_2 P25 coating after baking at 150°C to 750°C compared to the XRD patterns of $\text{TiO}_2/\text{SiO}_2$ coating after baking at 150°C to 950°C are shown in Figure 5.4.

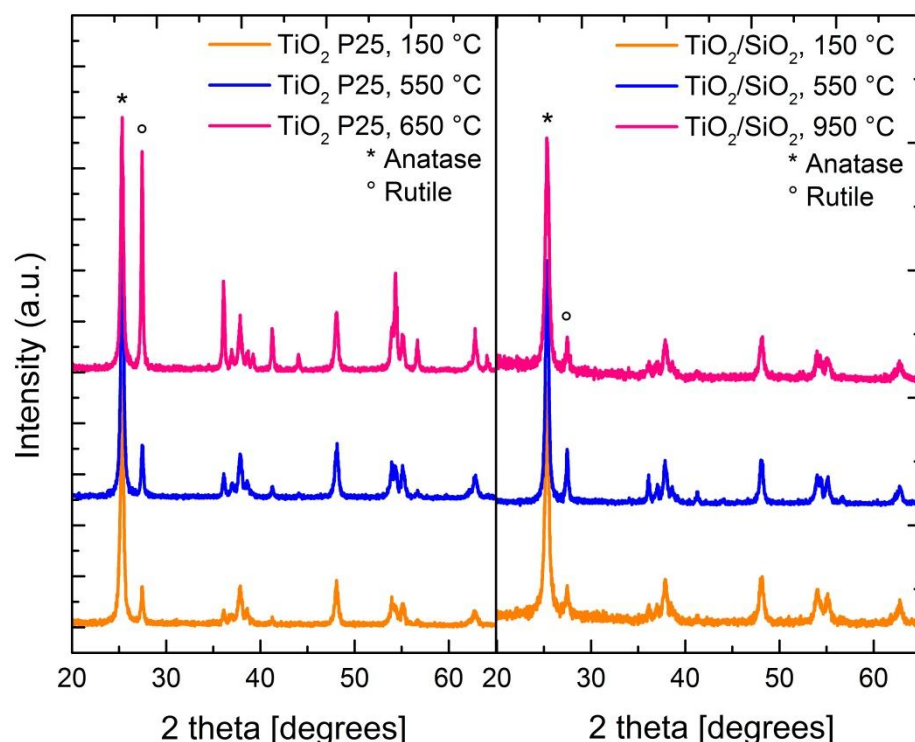


Fig. 5.4: XRD patterns of TiO_2 P25 scratched from coatings after baking at 150 °C, 550 °C and 650 °C (left) and XRD patterns of $\text{TiO}_2/\text{SiO}_2$ scratched from coatings after baking at 150 °C, 550 °C and 950 °C (right)

As shown in Fig. 5.4 (left), the X-ray patterns of TiO_2 P25 particles scratched from coatings after baking show only peaks corresponding to the anatase and rutile phase. The XRD patterns of TiO_2 P25 from the Si-wafer baked up to 550 °C, show approximately the same intensity of rutile peak suggesting no phase transformation occurred. When the baking temperature of the coating is above 550 °C, an obvious increase of the rutile peak intensity is observed indicating phase transformation from anatase to rutile. The results are in agreement with the studies of Nádia et al. [21] that the phase transformation of TiO_2 P25 occurred at temperatures from 400 °C to 800 °C. In contrast to the TiO_2 P25, the coating with $\text{TiO}_2/\text{SiO}_2$ particles shows a negligible change of phase composition after baking up to 950 °C, as shown in Fig. 5.4 (right). The effect of the baking temperature on the phase composition of the TiO_2 P25 coating and $\text{TiO}_2/\text{SiO}_2$ coating is illustrated in Fig. 5.5.

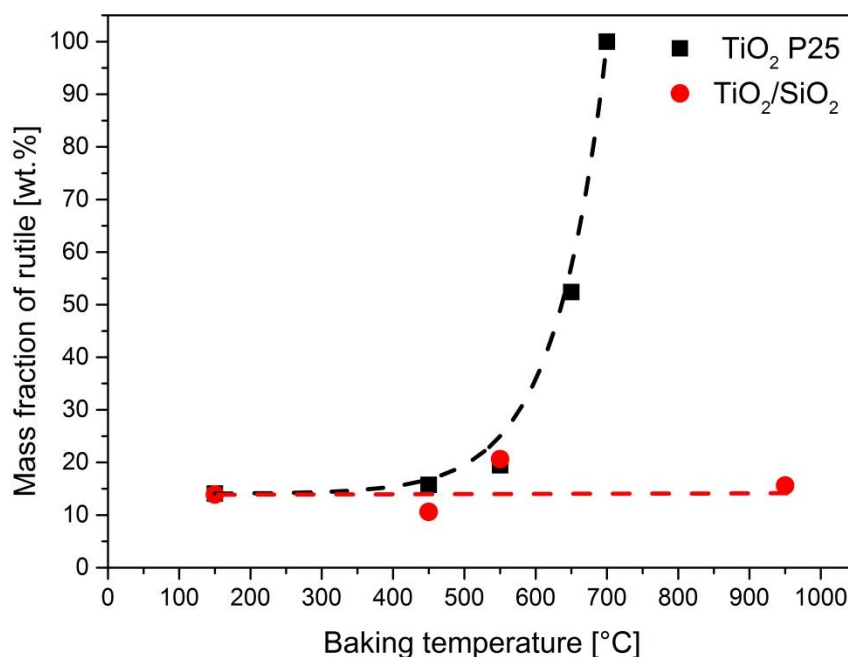


Fig. 5.5: The effect of the baking temperature on the phase composition of the TiO_2 P25 and $\text{TiO}_2/\text{SiO}_2$ particles

For the non-calcinated flame synthesized $\text{TiO}_2/\text{SiO}_2$ particles (sample P4), the rutile mass fraction is about 14 wt.% (Fig. 5.5). After baking of the $\text{TiO}_2/\text{SiO}_2$ coating up to 950 °C, the rutile mass fraction still remains constant at approximately 14 wt.%, similar to that of the non-calcinated powder. In the case of TiO_2 P25 coating, the rutile mass fraction increases dramatically at baking temperatures above 550 °C. The rutile mass fraction increases to 52.4 wt.% and 100 wt.% after baking at 650 °C and 700 °C, respectively. The change of the phase composition of the both tested coating is the same as determined for the original powders. The results suggest that neither the coating process nor the interaction with the Si-wafer has an influence on the thermostability of the tested powders.

5.4.3 Photocatalytic activity of coating

The photocatalytic activity of coatings with stabilized TiO_2 was evaluated for the DCA degradation compared to coatings with the reference material TiO_2 P25. Fig. 5.6 shows the DCA degradation curves of coatings with TiO_2 P25. For the TiO_2 P25

coating baked at 150 °C, about 63 % DCA was decomposed within 2 hours. With increasing baking temperature, the photocatalytic activity of this coating becomes lower. After baking at 750 °C, the coating had degraded only 4.1 % DCA, because almost all anatase have transited to rutile resulting in a loss of the photocatalytic activity. However, the decrease of photocatalytic activity is not monotonically with increased baking temperature. The coating calcinated at 550 °C had decomposed ca. 61 % DCA within 2 hours and is a little more active than the coating backed at 450 °, which had decomposed only about 55 % DCA within 2 hours. The reason is that the crystallinity of TiO₂ P25 may be slight changed during the heat treatment [80] and the photocatalytic activity of TiO₂ is proportional to its crystallinity.

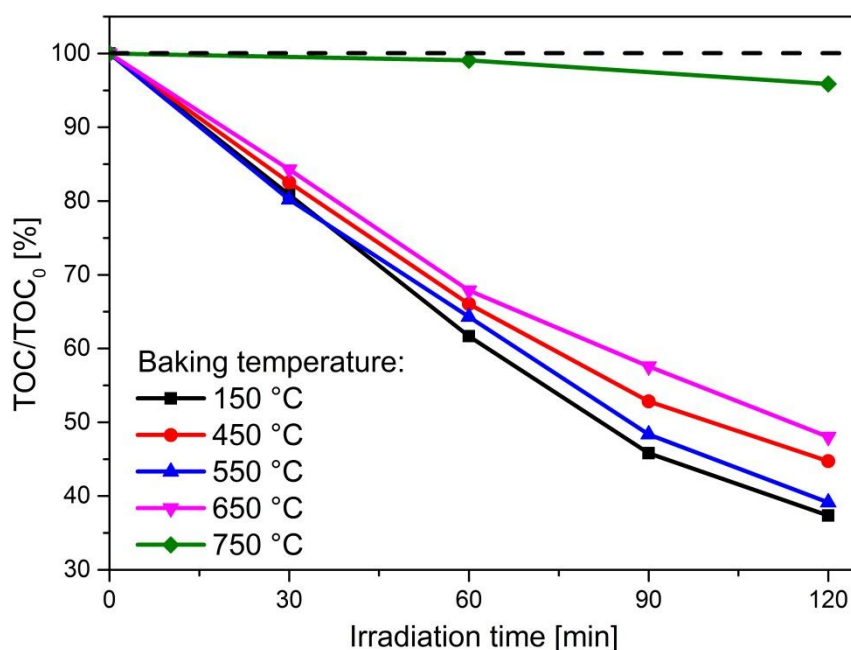


Fig. 5.6: The DCA degradation curves of TiO₂ P25 coating on Si-wafer baked at different temperatures

It is noteworthy that the photocatalytic activity of the TiO₂ P25 coating baked at 750 °C decreases rapidly to nearly zero compared to the coating baked at 650 °C degrading about 50 % DCA. The increase of baking temperature from 150 °C to 650 °C causes a decrease of 10.7 % of DCA degradation, whereas a further increase of baking temperature from 650 °C to 750 °C results in an almost complete inactivity of the coating. This tendency is due to the phase composition of the coating made of

TiO_2 P25, as shown in Fig. 5.5. The rutile mass fraction of the TiO_2 P25 coating increases steadily from 15.7 to 52.4 % with increased baking temperature from 150 °C to 650 °C. A further increase of baking temperature to 700 °C leads to the disappearance of the anatase peaks. The results are consistent with the observations of Lee et al. [105] and Porter et al. [115] that for the phase transformation high activation energy is required explaining the immeasurably slow transition of anatase at temperatures below 550 °C and rapid one at temperatures exceeding 650 °C.

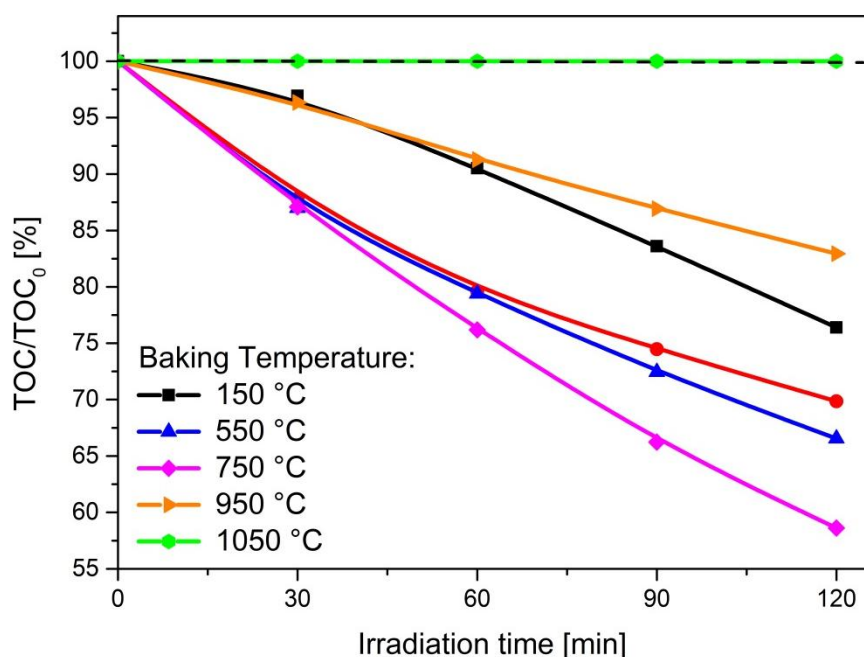


Fig. 5.7: The DCA degradation curves of $\text{TiO}_2/\text{SiO}_2$ coating on Si-wafer baked at different temperatures

The DCA degradation curves of the coating with $\text{TiO}_2/\text{SiO}_2$ particles are shown in Fig. 5.7. The coating baked at 750 °C shows the highest photocatalytic activity and about 41 % DCA was decomposed within 2 hours, whereas the lowest DCA degradation of coating appears after baking at 1050 °C showing no activity. The change of the photocatalytic activity is not monotone. The photocatalytic activity of $\text{TiO}_2/\text{SiO}_2$ coating first increases with increased baking temperature up to 750 °C and decreases with further increased baking temperature. In contrast to the coating with TiO_2 P25, the photocatalytic activity of $\text{TiO}_2/\text{SiO}_2$ coating is generally lower. To clearly compare the photocatalytic ability, the calculated reaction rate constants of the

coating with TiO₂ P25 and TiO₂/SiO₂ particles as a function of baking temperature are shown in Fig. 5.8.

The reaction rate constants of the TiO₂ P25 coating are approximate constant at about $7.5 \cdot 10^{-3} \text{ s}^{-1}$ at low baking temperatures up to 600 °C. Above 650 °C the reaction rate decreased rapidly to zero because of the phase transformation. The TiO₂/SiO₂ coating shows a reaction constant of $2.29 \cdot 10^{-3} \text{ s}^{-1}$ after baking at 150 °C, approximately one third of the value of the coating with TiO₂ P25. With increasing calcination temperature up to 750 °C the reaction rate constantly increases until a maximum value of $4.47 \cdot 10^{-3} \text{ s}^{-1}$, about 60% of the maximum value of coating with TiO₂ P25. Subsequently, the reaction constant decreases with further increased baking temperature down to zero.

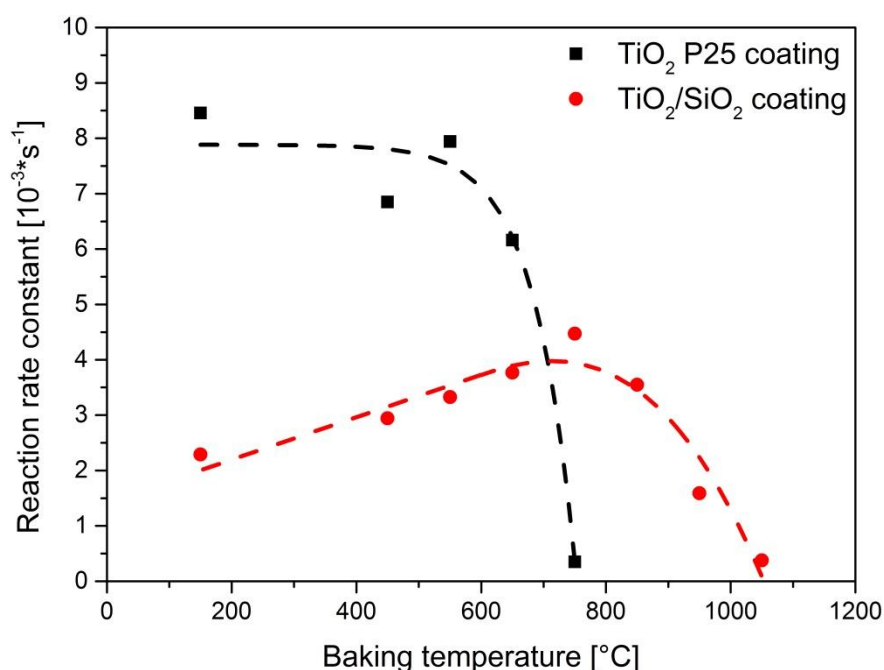


Fig. 5.8: Reaction rate constant of TiO₂ P25 coating and TiO₂/SiO₂ coating as a function of baking temperature

The reasons for the different photocatalytic activity of TiO₂ P25 coating and TiO₂/SiO₂ coating are the same as for the powders, which are discussed in the previous chapter. For the photocatalytic degradation of DCA, the accessibility of the TiO₂ particle surface is important. DCA can be decomposed only when it is in close contact with TiO₂ surface, where the interfacial transfer of charge carriers from the TiO₂ surface to

DCA molecules is sufficient. The encapsulation of the TiO₂ particles with a silicon layer can stabilize TiO₂ particles, but at the same time can suppress the charge transfer causing the reduction of the photocatalytic activity. After heat treatment of the TiO₂/SiO₂ coating, the surface of the TiO₂ particles is released again which results in an increase of the photocatalytic activity of TiO₂/SiO₂ coating at the maximal value of 750 °C. With further increasing baking temperature, the phase transformation and particle growth are initiated due to the breaking of the SiO₂ layer. Therefore, the photocatalytic activity decreases to nearly zero after baking at 1050 °C. However, the photocatalytic activity of TiO₂/SiO₂ coating after baking is lower than for the TiO₂ P25 coating, because of the inhomogeneous SiO₂ layer on the TiO₂ particles causing a loss of a part of anatase in TiO₂/SiO₂ particles during heat treatment. The results are consistent with the observation of the photocatalytic performance of TiO₂/SiO₂ powders evaluated in the previous chapter.

It should be noted that the most active TiO₂/SiO₂ coating is observed after baking at 750 °C and a further increase of the baking temperature decreases the photocatalytic activity of the coating. In contrast, the original powders showed the maximal photocatalytic activity after calcination at 900 °C. However, the XRD analysis showed that there is neither a change in the phase composition (Fig. 5.5) nor in the primary particle size compared to the original powders. In principle, the dependency of the photocatalytic activity on calcination temperature should be the same for the TiO₂/SiO₂ coatings and for the original powders. Unfortunately, the reason for the drop of the photocatalytic activity of the TiO₂/SiO₂ coating at lower temperature is so far unclear but may be related to the porous structure. Fig. 5.2, shows a cross section through the coating. It is obvious that silica draining from the upper TiO₂/SiO₂ particles for temperature above 750 °C may reduce the surface accessible for catalytic reaction.

It is mentioned that the self-cleaning effect of TiO₂ coating is based on the combination of photocatalytic activity and superhydrophilicity (i.e. a water contact angle of ~ 0°). While the photoactive property of TiO₂ is favored to oxidizing the adsorbed contaminants on the self-cleaning surface, the superhydrophilic property favors spread water to easily remove the contaminants from the surface. As shown in Fig. 5.9 (left), the water contact angle of a TiO₂ P25 film (thickness of around 10 nm) is about 12° determined with the sessile drop method. It should be noted that the

contact angle depends strongly on the roughness of the film. According to the Wenzel model, the contact angle decreases with increased roughness of the film surface [116, 117]. The low contact angle on the TiO_2 P25 film indicates high roughness of the surface. In addition, according to the studies of Fujishima et al. [3, 116], the water contact angle on the TiO_2 film decreases with UV irradiation time because of the reconstruction of the surface hydroxyl groups. Fig. 5.9 (right) shows the contact angle on TiO_2 P25 film with UV irradiation in 5 minutes decreased from around 12° to 6° .

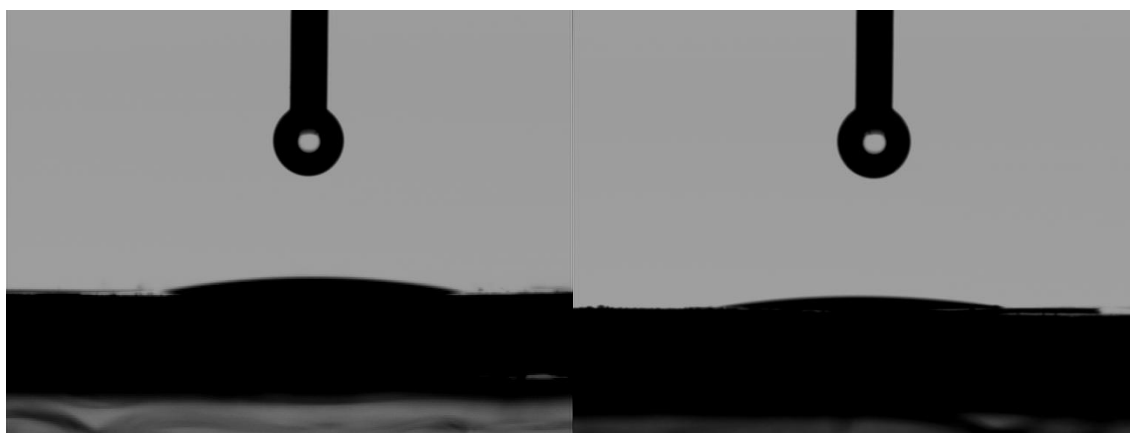


Fig. 5.9: Water contact angle measurement on TiO_2 P25 film without UV irradiation (left) and with UV irradiation (right)

Fig. 5.10 shows the effect of heat treatment and UV irradiation on the contact angle on the thermostable $\text{TiO}_2/\text{SiO}_2$ film. It was found that without UV irradiation the contact angle on the $\text{TiO}_2/\text{SiO}_2$ film before calcination at 900°C is about 14° (Fig. 5.10 a). After calcination the contact angle on the film decreases to about 10° (Fig. 5.10 b) indicating that TiO_2 particle surface was released by heat treatment water molecules had more contact with TiO_2 particles. This result is consistent with the observation in previous chapter. Moreover, additional UV irradiation increases the hydrophilicity of the $\text{TiO}_2/\text{SiO}_2$ film by further reducing the water contact angle (Fig. 5.10 c).

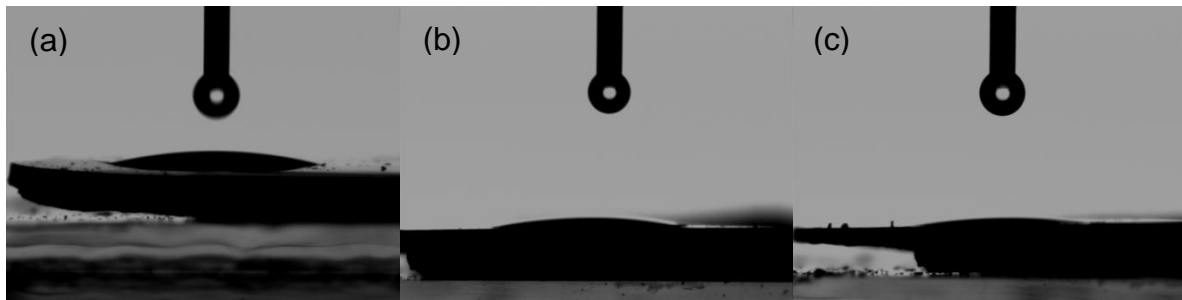


Fig. 5.10: The effect of heat treatment and UV irradiation on the contact angle on the $\text{TiO}_2/\text{SiO}_2$ film ((a) before calcination, (b) after calcination without uv-irradiation, (c) after calcination with UV-irradiation)

Therefore, it can be concluded that the coating made of $\text{TiO}_2/\text{SiO}_2$ particles is not only stable at high temperatures but also shows excellent self-cleaning properties when applied to extended surfaces and exposed to high temperatures.

6 Summary

In the present study, TiO_2 nanoparticles were synthesized in a premixed flame. The particle properties such as size, phase composition and specific surface area, which are affected by TiCl_4 precursor feed rate, were characterized using TEM, XRD and BET, respectively. Subsequently, the photocatalytic activity of flame synthesized TiO_2 nanoparticles was tested for the degradation of DCA and 4-CP in the liquid phase.

Starting with the synthesis of photocatalytically active TiO_2 nanoparticles, stabilization was achieved with SiO_2 by directly introducing SiCl_4 precursor in the flame to form a core-shell structure. The binary $\text{TiO}_2/\text{SiO}_2$ samples were calcinated at temperatures between 900 °C and 1200 °C. Particle size, specific surface area, phase composition and photocatalytic activity were investigated. Subsequently, the stabilized TiO_2 particles were applied for co-firing self-cleaning surface. The thermostability and photocatalytic activity were also evaluated for this application.

For pure TiO_2 nanoparticles, increasing the precursor feed rate from 0.021 mmol/min to 0.504 mmol/min, the specific surface area decreased from 166 m^2/g to 70 m^2/g and the BET equivalent diameter of TiO_2 particles increased from 9 nm to 21 nm. According to the XRD analysis, the flame made TiO_2 particles consisted of mainly anatase phase of above 90 wt.% and with increased precursor feed rate from 0.021 mmol/min to 0.504 mmol/min the rutile mass fraction increased from zero to 10 wt.%. The variation of the precursor feed rate strongly influenced the average particle size and the particle size distribution. With increasing precursor feed rate, the average particle size increased and the distribution becomes broader. The TEM equivalent particle size shifted from 7 nm to 21 nm with precursor feed rate increasing from 0.021 mmol/min to 0.504 mmol/min. The photocatalytic activity of flame synthesized TiO_2 samples was higher than that of the reference material TiO_2 P25 for the degradation of DCA and 4-CP. The photocatalytic activity increased firstly with increasing precursor feed rate up to a maximum value and then decreased for further increasing precursor feed rate. The sample synthesized at precursor feed rate of 0.071 mmol/min showed the highest photocatalytic activity and was much more active than the reference material TiO_2 P25.

The binary $\text{TiO}_2/\text{SiO}_2$ samples showed high thermostability up to 1050 °C for 3 hours. As shown with BET analysis, the non-calcinated $\text{TiO}_2/\text{SiO}_2$ samples showed approximately constant specific surface area of about 85 m²/g for high silica contents. After calcination at temperatures between 900 °C and 1100 °C, the $\text{TiO}_2/\text{SiO}_2$ agglomerates collapsed due to particle growth (for low silica content) or restructuring of agglomerate (for high silica content). At the same time the specific surface area decreased to an extent depending on calcination temperature and silica content. For each calcination temperature, the specific surface areas of calcinated samples increased with increasing Si/Ti ratio up to a maximum and then decreased for further increasing Si/Ti ratio. The phase composition of binary $\text{TiO}_2/\text{SiO}_2$ particles is also strongly dependent on the silica amount and calcination temperature. When the TiO_2 particles were protected with a sufficiently thick SiO_2 layer, they showed almost the same anatase mass fraction of about 85 wt.% as the non-calcinated ones as long as the calcination temperature was lower than 1100 °C. For calcination temperatures above 1100 °C, the SiO_2 layer could not withstand the heat treatment and, independently of the thickness of the SiO_2 layer, the anatase mass fraction decreased to about 55 wt.% and 25 wt.% for calcination temperatures of 1150 °C and 1200 °C, respectively. Therefore, it was concluded that the thermostability of stabilized TiO_2 particle was improved up to about 1050 °C. The TEM analysis showed that the SiO_2 additive had no effect on the particle morphology. The TEM equivalent particle size of $\text{TiO}_2/\text{SiO}_2$ samples was kept constant at about 17 nm after calcination up to 1050 °C and increased dramatically after calcination above 1050 °C to over 50 nm. The photocatalytic activity of stabilized TiO_2 particles depends strongly on the silica additive amount and calcination temperature. For calcination temperatures between 900 °C and 1150 °C, the photocatalytic activity exhibited a maximum as a function of Si/Ti ratio. The position of the maximum photocatalytic activity depended on the calcination temperature and silica content. The increase of photocatalytic performance for low Si/Ti ratios (left side of the maximum) is due to improved survival of anatase after heat treatment. The activity decrease for high Si/Ti ratios (right side of the maximum) is caused by the reduced accessibility of the TiO_2 surface for DCA molecules due to the excessive amount of SiO_2 on the TiO_2 particles.

A flame synthesized binary $\text{TiO}_2/\text{SiO}_2$ was applied for a self-cleaning coating on silica surface serving as model substrate for the intended co-firing of self-cleaning roof tiles.

The XRD analysis showed that the substrate and the coating process did not affect the thermostability of $\text{TiO}_2/\text{SiO}_2$ particles. In contrast to the reference material TiO_2 P25, the coating with binary particles conserved the anatase mass fraction after calcination up to 1050 °C. The coating with binary particles showed also high photocatalytic activity for the degradation of DCA after baking. The highest photocatalytic activity of coating with binary particles appeared at 750 °C, whereas the coating with reference material was totally inactive at this baking temperature.

7 Outlook

In the present study, the flame synthesized TiO_2 particles coated with SiO_2 layer show high thermostability in contrast to the reference material TiO_2 P25. Moreover, the stabilized particles show high photocatalytic activity after heat treatment. Unfortunately, due to imperfect mixing of the SiO_2 coating molecules with the already formed TiO_2 nanoparticles in the flame, the thickness of the SiO_2 layer is not uniform. Although even the non-calcinated $\text{TiO}_2/\text{SiO}_2$ particles showed a certain photocatalytic activity for the degradation of DCA, the part of TiO_2 particles, which were not coated or coated with a insufficiently thick SiO_2 layer, lost their photocatalytic activity due to the phase transformation during calcination. Therefore, pilot tests were carried out to coat the TiO_2 particle with SiO_2 by means of a plasma reactor. The results showed that the SiO_2 layer on TiO_2 surface is homogenous and depending on the process parameters the SiO_2 layers can be adjusted up to 10 nm. In the coming work, the plasma reactor will be integrated in the flame reactor for online coating of TiO_2 particles.

The stabilized TiO_2 particles exhibited high photocatalytic activity after calcination. It is assumed that at high temperatures the SiO_2 layer becomes mobile because of reduced viscosity. By online observation of the samples during heating in a TEM it was shown that at 800 °C the initially coated TiO_2 surfaces were released by viscous flow of SiO_2 . Since the TEM heating is limited to 800°C, it is planned to calcinate the samples dispersed on a Pt-grid in an external furnace at desired temperatures under inert atmosphere in upcoming work.

While so far only one stabilized sample was tested regarding its self-cleaning performance on Si-wafers, a systematic study of the influence of silica content and calcination procedure on photocatalytic activity is still missing. Once these points are clarified, the final goal of the study, i.e. the production of self-cleaning roof tiles in one step, will be addressed. In particular, photocatalytic activity and lifetime of the $\text{TiO}_2/\text{SiO}_2$ coating, also as a function of impurities originating from the substrate, have to be analyzed.

8 References

1. C. W. Hsu, L. Wang and W.F. Su, Effect of chemical structure of interface modifier of TiO_2 on photovoltaic properties of poly(3-hexylthiophene)/ TiO_2 layered solar cells. *Journal of Colloid and Interface Science*, 2009. 329: p. 182-187.
2. A. Fujishima, T. N. Rao and D. A. Tryk, Titanium dioxide photocatalysis. *Journal of Photochemistry and Photobiology C: Photochemistry Reviews*, 2000. 1: p. 1-21.
3. A. Fujishima and X. Zhang, Titanium dioxide photocatalysis: present situation and future approaches. *Comptes Rendus Chimie*, 2006. 9: p. 750-760.
4. M. R. Hoffmann, S. T. Martin, W. Chio and D. W. Bahnemann, Environment applications of semiconductor photocatalysis. *Chemical Reviews*, 1995. 95: p. 69-96.
5. W. J. Stark and S. E. Pratsinis, Aerosol flame reactors for manufacture of nanoparticles. *Powder Technology*, 2002. 126: p. 103-108.
6. A. Fujishima, X. Zhang and D. A. Tryk, Heterogeneous photocatalysis: From water photolysis to applications in environmental cleanup. *International Journal of Hydrogen Energy*, 2007. 32: p. 2664-2672.
7. R. Strobel, A. Baiker and S. E. Pratsinis, Aerosol flame synthesis of catalysts. *Advanced Powder Technology*, 2006. 17: p. 457-480.
8. S. E. Pratsinis, Flame aerosol synthesis of ceramic powders. *Progress in Energy and Combustion Science*, 1998. 24: p. 197-219.
9. S. Yang, Y.-H. Jang, C. H. Kim, C. Hwang, J. Lee, S. Chae, S. Jung and M. Choi, A flame metal combustion method for production of nanoparticles. *Powder Technology*, 2010. 197: p. 170-176.
10. H. D. Jang and S. K. Kim, Controlled synthesis of titanium dioxide nanoparticles in a modified diffusion flame reactor. *Materials Research Bulletin*, 2001. 36: p. 627-637.
11. V. Ramaswamy, N. B. Jagtap, S. Vijayanand, D. S. Bhange and P. S. Awati, Photocatalytic decomposition of methylene blue on nanocrystalline titania prepared by different methods. *Materials Research Bulletin*, 2007. 43: p. 1145-1152.

12. W. Li, Y. Bai, C. Liu, Z. Yang, X. Feng, X. Lu, N. Vanderlaak and D. Y. Chan, Highly thermal stable and highly crystalline anatase TiO₂ for photocatalysis. *Environmental Science & Technology*, 2009. 43: p. 5423-5428.
13. K. K. Akurati, A. Vital, G. Fortunato, R. Hany, F. Nueesch and T. Graule, Flame synthesis of TiO₂ nanoparticles with high photocatalytic activity. *Solid State Sciences*, 2007. 9: p. 247-257.
14. J. Araña, J. M. Doña-Rodríguez, D. Portillo-Carrizo, C. Fernández-Rodríguez, J. Pérez-Peña, O. G. Díaz, J. A. Navío and M. Macías, Photocatalytic degradation of phenolic compounds with new TiO₂ catalysts. *Applied Catalysis B: Environmental*, 2010. 100: p. 346-354.
15. G. Tian, H. Fu, L. Jing and C. Tian, Synthesis and photocatalytic activity of stable nanocrystalline TiO₂ with high crystallinity and large surface area. *Journal of Hazardous Materials*, 2009. 161: p. 1122-1130.
16. H. D. Jang, S.-K. Kim and S.-J. Kim, Effect of particle size and phase composition of titanium dioxide nanoparticles on the photocatalytic properties. *Journal of Nanoparticle Research*, 2001. 3: p. 141-147.
17. M. Zhang, L. Shi, S. Yuan, Y. Zhao and J. Fang, Synthesis and photocatalytic properties of highly stable and neutral TiO₂/SiO₂ hydrosol. *Journal of Colloid and Interface Science*, 2009. 330: p. 113-118.
18. D. Beydoun, R. Amal, G. Low and S. McEvoy, Role of nanoparticles in photocatalysis. *Journal of Nanoparticle Research*, 1999. 1: p. 439-458.
19. H. Zhang and J. F. Banfield, Thermodynamic analysis of phase stability of nanocrystalline titania. *Journal of Materials Chemistry*, 1998: p. 2073-2076.
20. H. Zhang, B. Chen and J. F. Banfield, The size dependence of the surface free energy of titania nanocrystals. *Physical Chemistry Chemical Physics*, 2009. 11: p. 2553-2558.
21. R. C. Nádia. M. Fernandes and S. S. Veronice, Influence of thermal treatment on the structure and photocatalytic activity of TiO₂ P25. *Catalysis Today*, 2005. 107-108: p. 5915-601.
22. H. Zhang and J. F. Banfield, Phase transformation of nanocrystalline anatase-to-rutile via combined interface and surface nucleation. *Journal of Materials Research*, 2000. 15: p. 437-448.
23. Y. Hu, H. L. Tsai and C. L. Huang, Phase transformation of precipitated TiO₂ nanoparticles. *Materials Science and Engineering*, 2003. 344: p. 209-214.

24. A. Kobata, K. Kusakabe and S. Morooka, Growth and transformation of TiO₂ crystallites in aerosol reactor. American Institute of Chemical Engineers, 1991. 37: p. 347-359.
25. D. M. Tobaldi, A. Tucci, A. S. Škapin and L. Esposito, Effects of SiO₂ addition on TiO₂ crystal structure and photocatalytic activity. Journal of the European Ceramic Society, 2010. 30: p. 2481-2490.
26. S. Yuan, Q. Sheng, J. Zhang, H. Yamashita and D. He, Synthesis of thermally stable mesoporous TiO₂ and investigation of its photocatalytic activity. Microporous and Mesoporous Materials, 2008. 110: p. 501-507.
27. R. D. Shannon and J. A. Pask, Topotaxy in the anatase-rutile transformation. The American Mineralogist, 1964. 49: p. 1707-1717.
28. K. Okada, N. Yamamoto, Y. Kameshima and A. Yasumori, Effect of silica additive on the anatase-to-rutile phase transition. Journal of American Ceramic Society, 2001. 84: p. 1591-1596.
29. A. Teleki, Flame synthesis and coating of nanostructured particles in one step. 2008, ETH Zürich: Dissertation.
30. H. S. Jie, H. Park, K. H. Kim, J. P. Ahn and J. K. Park, In-Situ TEM observation on phase formation of TiO₂ nanoparticle synthesized by flame method. Materials Science Forum, 2007. 534-536: p. 81-84.
31. H. Zhang and J. Banfield, Kinetics of crystallization and crystal growth of nanocrystalline anatase in nanometer-sized amorphous titania. Chemistry of Materials, 2002. 14: p. 4145-4154.
32. C. H. Hung and J. L. Katz, Formation of mixed oxide powders in flames: Part I. TiO₂-SiO₂. Journal of Materials Research, 1992. 7: p. 1861-1869.
33. K. K. Akurati, R. Dittmann, A. Vital, U. Klotz, P. Hug, T. Graule and M. Winterer, Silica-based composite and mixed-oxide nanoparticles from atmospheric pressure flame synthesis. Journal of Nanoparticle Research, 2006. 8: p. 379-393.
34. S. H. Ehrman, S. K. Friedlander and M. R. Zachariah, Characteristics of SiO₂/TiO₂ nanocomposite particles formed in a premixed flat flame. Journal of Aerosol Science, 1997. 29: p. 687-706.
35. S. Kim and S. H. Ehrman, Capillary Condensation onto titania (TiO₂) nanoparticle agglomerates. Langmuir, 2007. 23: p. 2497-2504.

36. A. Teleki, M. K. Akhtar and S. E. Pratsinis, The quality of SiO₂-coatings on flame-made TiO₂-based nanoparticles. *Journal of Materials Chemistry*, 2008. 18: p. 3547-3555.
37. M. Hofer and D. Penner, Thermally stable and photocatalytically active titania for ceramic surfaces. *Journal of the European Ceramic Society*, 2011. 31: p. 2887-2896.
38. A. L. Linsebigler, G. Lu and J. T. Yates, Photocatalysis on TiO₂ Surfaces: Principles, Mechanisms, and Selected Results. *Chemical Reviews*, 1995. 95: p. 735-758.
39. A. Mills and S. L. Hunte, An overview of semiconductor photocatalysis. *Journal of Photochemistry and Photobiology A: Chemistry*, 1997. 108: p. 1-35.
40. R. Benedix, F. Dehn, J. Quaas, and M. Orgass, Application of titanium dioxide photocatalysis to create self-Cleaning building materials, in *Lacer*, No. 5, 2000.
41. D. C. Hurum, A. G. Agrios and K. A. Gray, Explaining the enhanced photocatalytic activity of Degussa P25 mixed-phase TiO₂ using EPR. *Journal of Physical Chemistry B*, 2003. 107: p. 4545-4549.
42. H. Gerischer and A. Heller, The role of oxygen in photooxidation of organic molecules on semiconductor particles. *Journal of physical Chemistry*, 1991. 95: p. 5261-5267.
43. G. P. Fotou and S. E. Pratsinis, Photocatalytic destruction of phenol and salicylic acid with aerosol-made and commercial titania powders. *Chemical Engineering Communications*, 1996. 151: p. 251-269.
44. C. M. Lindner, Optimierung der photokatalytischen Wasserreinigung mit Titandioxid: Festkörper- und Oberflächenstruktur des Photokatalysators, 1997, Universität Hannover, Dissertation.
45. I. K. Konstantinou and T. A. Albanis, TiO₂-assisted photocatalytic degradation of azo dyes in aqueous solution: kinetic and mechanistic investigations: A review. *Applied Catalysis B: Environmental*, 2004. 49: p. 1-14.
46. N. Guettaï and H. A. Amar, Photocatalytic oxidation of methyloange in presence of titanium dioxide in aqueous suspension. Part II: kinetics study. *Desalination and the Environment*, 2005. 185(1-3): p. 439-448.
47. A. Fujishima and K. Honda, Electrochemical Photolysis of Water at a Semiconductor Electrode. *Nature*, 1972. 238: p. 37-38.

48. G. S. Mital and T. Manoj, A review of TiO₂ nanoparticles. Chinese Science Bulletin, 2011. 56: p. 1639-1657.
49. X. Chen and S. S. Mao, Titanium dioxide nanomaterials: Synthesis, properties, modifications and applications. Chemical Reviews, 2007. 107: p. 2891-2959.
50. S. M. Gupte and M. Triathi, A review on the synthesis of TiO₂ nanoparticles by solution route. Central European Journal of Chemistry, 2012. 10: p. 279-294.
51. D. P. Macwan, P. N. Dave and S. Chaturvedi, A review on nano-TiO₂ sol–gel type syntheses and its applications. Journal of Materials Science 2011. 46: p. 3669-3686.
52. D. S. Ensor, Aerosol science and technology: History and review. 2011, USA: TRI International.
53. G. D. Ulrich, Theory of particle formation and growth in oxide synthesis flames. Combustion Science and Technology, 1971. 4: p. 47-57.
54. G. D. Ulrich, B. A. Milnes and N. S. Subramanian, Particle growth in flames. II: Experimental results for silica particles. Combustion Science and Technology, 1976. 14: p. 243-249.
55. A. Camenzind, W. R. Caseri and S. E. Pratsinis, Flame-made nanoparticles for nanocomposites. Nano Today, 2010. 5: p. 48-65.
56. H. Chang, S. J. Kima, H. D. Jang and J. W. Choi, Synthetic routes for titania nanoparticles in the flame spray pyrolysis. Colloids and Surfaces A: Physicochemical Engineering Aspects, 2008: p. 282-287.
57. K. Nakaso, K. Okuyama, M. Shimada and S. E. Pratsinis, Effect of reaction temperature on CVD-made TiO₂ primary particle diameter. Chemical Engineering Science, 2003. 58: p. 3327-3335.
58. M. K. Akhtar, Y. Xiong and S. E. Pratsinis, Vapor synthesis of titania powder by titanium tetrachloride oxidation. Journal of Aerosol Science, 1991. 22: p. 35-38.
59. K. Wegner, Nanoparticle synthesis in gas-phase system: Process design and scale-up for metal and metal oxide. 2002, ETH Zürich: Dissertation.
60. K. E. J. Lehtinen and M. R. Zachariah, Energy accumulation in nanoparticle collision and coalescence processes. Journal of Aerosol Science, 2002. 33: p. 357-368.
61. W. Koch and S. K. Friedlander, Particle growth by coalescence and agglomeration. Journal of Aerosol Science, 1990. 21: p. 73-76.

62. W. Koch and S. K. Friedlander, The effect of particle coalescence on the surface of a coagulating aerosol. *Journal of Colloid and Interface Science*, 1990. 140: p. 419-427.
63. P. T. Spicer, O. Chaoul, S. Tsantilis and S. E. Pratsinis, Titania formation by TiCl_4 gas phase oxidation, surface growth and coagulation. *Journal of Aerosol Science*, 2002. 33: p. 17-34.
64. P. T. Spicer and S. E. Pratsinis, Competition between gas phase and surface oxidation of TiCl_4 during synthesis of TiO_2 particles. *Chemical Engineering Science*, 1998. 53: p. 1861-1868.
65. H. Zhang and J. F. Banfield, Understanding polymorphic phase transformation behavior during growth of nanocrystalline aggregates: Insights from TiO_2 . *Journal of Physical Chemistry B*, 2000. 104: p. 3481-3487.
66. A. A. Gribb and J. F. Banfield, Particle size effects on transformation kinetics and phase stability in nanocrystalline TiO_2 . *American Mineralogist*, 1997. 82: p. 717-728.
67. R. D. Shannon and J. A. Pask, Kinetics of the anatase-rutile transformation. *Journal of American Ceramic Society*, 1965. 48: p. 391-398.
68. H. Zhang and J. F. Banfield, New kinetic model for the nanocrystalline anatase-to-rutile transformation revealing rate dependence on number of particles. *American Mineralogist*, 1999. 84: p. 528-535.
69. P. Periyat, K. V. Baiju, P. Mukundan, P. K. Pillai and K. G. K. Warriar, High temperature stable mesoporous anatase TiO_2 photocatalyst achieved by silica addition. *Applied Catalysis A: General*, 2008. 349: p. 13-19.
70. C. He, B. Tian and J. Zhang, Thermally stable SiO_2 -doped mesoporous anatase TiO_2 with large surface area and excellent photocatalytic activity. *Journal of Colloid and Interface Science*, 2010. 344: p. 382-389.
71. Q. H. Powell, G. P. Fotou, T. T. Kodas and B. Anderson, Coating of TiO_2 with metal oxides by gas-phase reactions. *Journal of Aerosol Science*, 1995. 26: p. 557-558.
72. Q. H. Powell, G. P. Fotou, T. T. Kodas, B. M. Anderson and Y. Guo, Gas-phase coating of TiO_2 with SiO_2 in a continuous flow hot-wall aerosol reactor *Journal of Materials Research*, 1997. 12: p. 552-559.

73. S. Jian, G. P. Fouto and T. T. Kodas, A theoretical study on gas-phase coating of aerosol particles. *Journal of colloid and interface science*, 1997. 185: p. 26-38.
74. N. Balázs, D. F. Srankó, A. Dombi, P. Sipos and K. Mogyorósi, The effect of particle shape on the activity of nanocrystalline TiO₂ photocatalysts in phenol decomposition. Part 2: The key synthesis parameters influencing the particle shape and activity. *Applied Catalysis B: Environmental*, 2010. 96: p. 569-576.
75. K. Mogyorósi, N. Balázs, D. F. Srankó, E. Tombácz, I. Dékány, A. Oszkó, P. Sipos and A. Dombi, The effect of particle shape on the activity of nanocrystalline TiO₂ photocatalysts in phenol decomposition. Part 3: The importance of surface quality. *Applied Catalysis B: Environmental*, 2010. 96: p. 577-585.
76. N. Balázs, K. Mogyorósi, D. F. Srankó, A. Pallagi, T. Alapi, A. Oszkó, A. Dombi and P. Sipos, The effect of particle shape on the activity of nanocrystalline TiO₂ photocatalysts in phenol decomposition. *Applied Catalysis B: Environmental*, 2008. 84: p. 356-362.
77. A. Hagfeldt and M. Grätzel, Light-induced redox reactions in nanocrystalline systems. *Chemical Reviews* , 1995. 95: p. 49-68.
78. M. Kaneko, *Photocatalysis-Science and Technology*, 3rd. Edition. 1999: Springer Verlag.
79. B. Ohtani, Y. Ogawa and S. Nishimoto, Photocatalytic activity of amorphous-anatase mixture of titanium(IV) oxide particles suspended in aqueous solutions. *Journal of Physical Chemistry B*, 1997. 101: p. 3746-3752.
80. K. Tanaka, M. F. V. Capule and T. Hisanaga, Effect of crystallinity of TiO₂ on its photocatalytic action. *Chemical Physics Letters*, 1991. 187: p. 73-76.
81. K. M. Schindler and M. Kunst, Charge carrier Dynamics in TiO₂ Powders. *Journal of Physical Chemistry B*, 1990. 94: p. 8222-8226.
82. M. A. Fox and M. T. Dulay, Heterogeneous Photocatalysis. *Chemical Reviews*, 1993. 93: p. 341-357.
83. A. Moiseev, F. Qi, J. Deubener and A. Weber, Photocatalytic activity of nanostructured titanium dioxide from diffusion flame synthesis. *Chemical Engineering Journal*, 2011. 170(1): p. 308-315.

84. Fei Qi, A. Moiseev, J. Deubener and A. Weber, Thermostable photocatalytically active TiO₂ anatase nanoparticles. *Journal of Nanoparticle Research*, 2011. 13: p. 1325-1334.
85. R. A. Spurr and H. Meyer, Quantitative analysis of anatase-rutile mixtures with an X-Ray diffractometer. *Analytical Chemistry*, 1957. 29: p. 760-762.
86. J. I. Langford and A. J. C. Wilson, Seherer after sixty years: A survey and some new results in the determination of crystallite size. *Journal of Applied Catalyst*, 1978. 11: p. 102-113.
87. J. Theurich, M. Lindner and D. W. Bahnemann, Photocatalytic degradation of 4-Chlorophenol in aerated aqueous titanium dioxide suspensions: A kinetic and mechanistic study. *Langmuir*, 1996. 12: p. 6368-6376.
88. X. Li, J. W. Cubbage, T. A. Tetzlaff and W. S. Jenks, Photocatalytic degradation of 4-Chlorophenol. 1. The hydroquinone pathway. 2. The Chlorocatechol pathway. *Journal of Organic Chemistry*, 1999. 64: p. 8509-8536.
89. D.W. Bahnemann, D. Bockelmann, R. Goslich, M. Hilgendorff and D. Weichgrebe, Photocatalytic purification and treatment of water and air. 1993, Amsterdam: D.F. Ollis and H. Al-Ekabi, Elsevier Science Publishers.
90. K. K. Akurati, A. Vital, U. E. Klotz, B. Bommer, T. Graule and M. Winterer, Synthesis of non-aggregated titania nanoparticles in atmospheric pressure diffusion flames. *Powder Technology*, 2006. 165: p. 73-82.
91. S. E. Pratsinis, W. Zhu and S. Vemury, The role of gas mixing in the flame synthesis of titania powders. *Powder Technology*, 1996. 86: p. 87-93.
92. G. P. Fotou, S. Vemury and S. E. Pratsinis, Synthesis and evaluation of titania powders for photodestruction of phenol. *Chemical Engineering Science*, 1994. 49: p. 4939-4948.
93. M. Lindner, J. Theurich and D. W. Bahnemann, Photocatalytic degradation of organic compounds: accelerating the process efficiency. *Water Science and Technology*, 1997. 35(4): p. 79-86.
94. D. W. Bahnemann, D. Bockelmann and R. Goslich, Mechanistic studies of water detoxification in illuminated TiO₂ suspensions. *Solar Energy Materials*, 1991. 24: p. 564-583.

95. D.W Bahnemann, S. N. Kholuiskaya, R. Dillert, A. I. Kulak and A. I. Kokorin, Photodestruction of dichloroacetic acid catalyzed by nano-sized TiO_2 particles. *Applied Catalysis B: Environmental*, 2002. 36(2): p. 161-169.
96. S. Jöksa, D. Klausona, M. Krichevskaya, S. Preis, F. Qi, A. Weber, A. Moiseev and J. Deubener, Gas-phase photocatalytic activity of nanostructured titanium dioxide from diffusion flame synthesis. *Applied Catalysis B: Environmental*, 2011. 111-112: p. 1-9.
97. S. Klein, M. Winterer and H. Hahn, Reduced-pressure chemical vapor synthesis of nanocrystalline silicon carbide powders. *Chemical Vapor Deposition*, 1998. 4: p. 143-149.
98. A. Teleki, R. Wengeler, L. Wengeler, H. Nirschl and S. E. Pratsinis, Distinguishing between aggregates and agglomerates of flame-made TiO_2 by high-pressure dispersion. *Powder Technology*, 2008. 181: p. 292-300.
99. S. Kim and S. H. Ehrman, Photocatalytic activity of a surface-modified anatase and rutile titania nanoparticle mixture. *Journal of Colloid and Interface Science*, 2009. 338: p. 304-307.
100. J. P. Zhang, L. Y. Shi, Y. Y. Hu and Q. Y. Pan, Morphology and photocatalytic activity of nanosized titania particles. *Journal of Shanghai University*, 2001. 5: p. 247-252.
101. U. Müller, H. Burtscher and A. Schmidt-Ott, Photoemission from small metal spheres: A model calculation using an enhanced three-step model. *Physical Review B*, 1988. 28: p. 7814-7816.
102. M. Born and E. Wolf, *Principle of optics*, ed. 7th. 1997: Cambridge University Press.
103. L. Kavan, T. Stoto and M. Grätzel, Quantum size effect in nanocrystalline semiconducting TiO_2 layers prepared by anodic oxidative hydrolysis of TiCl_3 . *Journal of Physical Chemistry*, 1993. 97: p. 9493-9498.
104. Y. Suganuma and M. Suganuma, Effects of heat treatment on photocatalytic property of Sol-Gel derived polycrystalline TiO_2 . *Journal of Sol-Gel and Technology*, 2001. 22: p. 83-89.
105. G. W. Lee and S. M. Choi, Thermal stability of heat-treated flame-synthesized anatase TiO_2 nanoparticles. *Journal of Materials Science*, 2008. 43: p. 715-720.

106. N. Mahdjoub, N. Allen, P. Kelly and V. Vishnyakov, SEM and Raman study of thermally treated TiO₂ anatase nanopowders: Influence of calcination on photocatalytic activity. *Journal of Photochemistry and Photobiology A: Chemistry*, 2010. 211: p. 59-64.
107. C. Perego, R. Revel, O. Durupthy, S. Cassaignon and J.-P. Jolivet, Thermal stability of TiO₂-anatase: Impact of nanoparticles morphology on kinetic phase transformation. *Solid State Sciences*, 2009. 6: p 989-995.
108. E. H. Choi, S. I. Hong and D. J. Moon, Preparation of thermally stable mesostructured nano-sized TiO₂ particles by modified sol–gel method using ionic liquid. *Catalysis Letters*, 2008. 123: p. 84-89.
109. M. Hornfeck, Der Einfluss der Stöchiometrie und refraktären Dotierungen auf die Viskosität synthetischer Kieselgläser. 1998, Universität des Saarlandes, Dissertation.
110. W. Y. Teoh, R. Amal, L. Mädler and S. E. Pratsinis, Flame sprayed visible light-active Fe-TiO₂ for photomineralisation of oxalic acid. *Catalysis Today*, 2007. 120: p. 203-213.
111. J. Araña, O. G. Díaz, M. M. Saracho, J. M. D. Rodríguez, J. A. H. Melián and J. P. Peña, Photocatalytic degradation of formic acid using Fe/TiO₂ catalysts: the role of Fe³⁺/Fe²⁺ ions in the degradation mechanism. *Applied catalysis B: Environmental* 2001. 32: p. 49-61.
112. K. Cho, H. Chang, J. H. Park, B. G. Kim and H. D. Jang, Effect of molar ratio of TiO₂/SiO₂ on the properties of particles synthesized by flame spray pyrolysis. *Journal of Industrial and Engineering Chemistry*, 2008. 14: p. 860-863.
113. S. H. Ehrman and S. K. Friedlander, Phase segregation in binary SiO₂/TiO₂ and SiO₂/Fe₂O₃ nanoparticle aerosols formed in a premixed flame. *Journal of Materials Research*, 1999. 14: p. 1551-1561.
114. M. D. Sacks and T.-Y. Tseng, Preparation of SiO₂ Glass from Model Powder Compacts: II, Sintering. *Journal of the American Ceramic Society*, 1984. 67: p. 532-537.
115. J. F. Porter, Y.-G. Li and C. K. Chan, The effect of calcination on the microstructural characteristics and photoreactivity of Degussa P-25 TiO₂. *Journal of Materials Science*, 1999. 34: p. 1523-1531.

116. Z. Liu, X. Zhang, T. Murakami and A. Fujishima, Sol–gel $\text{SiO}_2/\text{TiO}_2$ bilayer films with self-cleaning and antireflection properties. *Solar Energy Materials & Solar Cells*, 2008. 92: p. 1434-1438.
117. K. Hashimoto, H. Irie and A. Fujishima, TiO_2 photocatalysis: A history overview and future prospects. *AAPPS Bulletin*, 2007. 17: p. 12-28.

9 Publications and Presentations

The thesis is based on following publications:

1. F. Qi, A. Moiseev, J. Deubener, A. P. Weber, Synthesis of $\text{TiO}_2/\text{SiO}_2$ photocatalysts in a diffusion flame reactor, International Congress on Particle Technology. 2010: Nürnberg.
2. F. Qi, A. Moiseev, J. Deubener, A. Weber, Thermostable photocatalytically active TiO_2 anatase nanoparticles. Journal of Nanoparticle Research, 2011. 13: p. 1325-1334.
3. F. Qi, A. Moiseev, J. Deubener, A. P. Weber, Hochttemperaturstabile TiO_2 -Nanopartikeln für photokatalytische Anwendung, in 5. Symposium Partikeltechnologie. 2011: Pfinztal, Germany.
4. A. Moiseev, F. Qi, J. Deubener, A. Weber, Photocatalytic activity of nanostructured titanium dioxide from diffusion flame synthesis. Chemical Engineering Journal, 2011. 170: p. 308-315.
5. S. Jöksa, D. Klausona, M. Krichevskaya, S. Preis, F. Qi, A. Weber, A. Moiseev, J. Deubener, Gas-phase photocatalytic activity of nanostructured titanium dioxide from diffusion flame synthesis. Applied Catalysis B: Environmental, 2012. 111-112: p. 1-9.
6. S. Dahle, L. Wegewitz, F. Qi, A. P. Weber, W. Maus-Friedrichs, Silicon dioxide coating of titanium dioxide nanoparticles from dielectric barrier discharge in a gaseous mixture of silane and nitrogen, Plasma Chemistry and Plasma Processing (submitted in 2012)
7. F. Qi, A. Moiseev, J. Deubener, A. Weber, chapter "High temperature stable nanoparticles by interface passivation demonstrated on self-cleaning titania coatings" to the "Handbook of functional nanomaterials", 2013, Nova Science Publishers, Ltd., USA
8. A. Moiseev, M. Krichevskaya, F. Qi, A. P. Weber, J. Deubener, Analysis of photocatalytic performance of nanostructured pyrogenic titanium dioxide powders in view of their polydispersity and phase transition: Critical anatase

particle size as a factor for suppression of charge recombination, Chemical Engineering Journal, 2013. 228: p 614-621.

Conference presentations

1. F. Qi, A. Moiseev, J. Deubener, A. Weber, Thermostable $\text{TiO}_2/\text{SiO}_2$ nanoparticles with high photocatalytic activity. International Aerosol Conference (IAC), Helsinki, Finland, 29th August-03rd September 2010.
2. F. Qi, A. Moiseev, J. Deubener, A. Weber, Hochtemperaturstabile Photokatalysator- Nanopartikel durch Grenzflächenpassivierung, ProcessNet, Jahrestreffen der Fachausschüsse Partikelmesstechnik & Grenzflächenbestimmte Systeme und Prozesse, Clausthal, Germany, 28th Februar – 02nd March 2011.
3. F. Qi, A. Moiseev, J. Deubener, A. Weber, Thermostability of flame synthesized core-shell $\text{TiO}_2/\text{SiO}_2$ nanoparticles and photocatalytic activity, European Aerosol Conference (EAC), Granada, Spain, 02nd-07th September 2012.

10 Curriculum Vitae

Date of birth 23rd September 1980

Place of birth Yizheng, Jiangsu, VR China

Education

02/2008 – 12/2012 TU Clausthal, Germany

Ph.D. study at the Institute of Particle technology under the supervision of Prof. Dr. rer. nat. Alfred Weber

Doctoral Thesis: “Synthesis of high temperature stable titania nanoparticles for photocatalytic applications”

09/2007 – 12/2007 Novatis AG, Switzerland

Diploma Thesis: “Entwicklung eines ‘Screening Tools’ im mg-Bereich zur Nasszerkleinerung von pharmazeutischen wirkstoffen“

10/2004 – 02/2012 TU Clausthal, Germany

Diploma study of environmental engineering

04/2004 – 10/2004 TU Clausthal, Germany

Language course

09/1999 – 07/2003 Wuhan University of Technology, Wuhan, VR China

Bachelor study of environmental engineering